OVEN CONTROLLED PACKAGE FOR MEMS DEVICES

A THESIS SUBMITTED TO
THE GRADUATE SCHOOL OF NATURAL AND APPLIED SCIENCES
OF
MIDDLE EAST TECHNICAL UNIVERSITY

BY

BÜŞRA ERDOĞAN

IN PARTIAL FULFILLMENT OF THE REQUIREMENTS
FOR
THE DEGREE OF MASTER OF SCIENCE
IN
MECHANICAL ENGINEERING

APRIL 2023

Approval of the thesis:

OVEN CONTROLLED PACKAGES FOR MEMS DEVICES

submitted by **BÜŞRA ERDOĞAN** in partial fulfillment of the requirements for the degree of **Master of Science** in **Mechanical Engineering, Middle East Technical University** by,

Prof. Dr. Halil Kalıpçılar
Dean, Graduate School of **Natural and Applied Sciences** ________________

Prof. Dr. M. A. Sahir Arıkan
Head of the Department, **Mechanical Engineering** ________________

Assoc. Prof. Dr. Kıvanç Azgın
Supervisor, **Mechanical Engineering, METU** ________________

Assoc. Prof. Dr. Özgür Bayer
Co-Supervisor, **Mechanical Engineering, METU** ________________

Examining Committee Members:

Assoc. Prof. Dr. Özgür Bayer
Mechanical Engineering, METU ________________

Assoc. Prof. Dr. Kıvanç Azgın
Mechanical Engineering, METU ________________

Assist. Prof. Dr. Hakan Çalışkan
Mechanical Engineering, METU ________________

Assist. Prof. Dr. Altuğ Özçelikkale
Mechanical Engineering, METU ________________

Assist. Prof. Dr. Emir Kutluay
Mechanical Engineering, Hacettepe University ________________

Date: 24.04.2023

I hereby declare that all information in this document has been obtained and presented in accordance with academic rules and ethical conduct. I also declare that, as required by these rules and conduct, I have fully cited and referenced all material and results that are not original to this work.

Name Last name : Büşra Erdoğan

Signature :

ABSTRACT

OVEN CONTROLLED PACKAGE FOR MEMS DEVICES

Erdoğan, Büşra
Master of Science, Mechanical Engineering
Supervisor : Assoc. Prof. Dr. Kıvanç Azgın
Co-Supervisor: Assoc. Prof. Dr. Özgür Bayer

April 2023, 110 pages

This thesis reports a temperature compensation approach for a MEMS sensor at the package level. The research involves the design, modeling, fabrication, and characterization of the vacuum level packaging of the MEMS sensor with a built-in closed-loop temperature controller. The design's primary objective is to create a temperature-controlled environment for the MEMS sensor. Alumina is selected as a material for constructing a temperature control surface. The MEMS sensor is bonded on top of the alumina base. The heating elements on the alumina base are formed by the deposition of metal, while temperature sensing is provided by thermistors. The package is sealed with a cap by soldering, and a copper tube is used to vacuum the internal cavity. The pinch-off method is used to seal the copper tube. Different than the prevailing literature, this research posits that temperature control is not solely limited to the MEMS sensor, but also encompasses the signal amplifier circuit. Therefore, the trans-impedance amplifier (TIA) circuit, which is also created on the alumina material, is positioned on the opposite side of the temperature control surface, on the back of the package. Consequently, the temperature control surface is also utilized for the TIA circuit.

An analytical model is developed to comprehend the system's thermal model and obtain a closed-loop temperature controller. In addition to the analytical model, a finite element model (FEM) is constructed for several important reasons. The first is a design check of the system before starting production and ensuring that heating elements can stabilize the package. The second is to obtain the heat transfer coefficient using test data and analyze the time-dependent behavior of the system with it. Finally, building a closed-loop controller while leveraging FEM.

The fabrication of the temperature control surface, the trans-impedance amplifier circuit, the implementation of all the elements, and tests are carried out in the METU MEMS Center. In the test phase of this work, the MEMS sensor is identified by using analytical and FEM approaches. System-level tests are conducted in a climate chamber with and without temperature control between 5 °C and 35 °C, as operating temperatures are defined within that range. Between 5 °C and 35 °C, the resonance frequency of the in-phase mode of the MEMS sensor deviates by 3120 Hz in the absence of an oven control. In contrast, the deviation of the resonance frequency with a closed-loop temperature controller is 380 Hz. Likewise, without a temperature controller, the deviation for the out-of-phase mode is 3140 Hz, whereas it is 154 Hz with a temperature controller.

Keywords: MEMS sensor, Temperature compensation, Oven control, Plant identification, Closed-loop control

ÖZ

MEMS CİHAZLARI İÇİN FIRIN KONTROLLÜ PAKET

Erdoğan, Büşra
Yüksek Lisans, Makina Mühendisliği
Tez Yöneticisi: Doç. Dr. Kıvanç Azgın
Ortak Tez Yöneticisi: Doç. Dr. Özgür Bayer

Nisan 2023, 110 sayfa

Bu tez, paket düzeyinde bir MEMS sensörü için bir sıcaklık kompanzasyon yaklaşımını rapor etmektedir. Araştırma, dahili bir kapalı devre sıcaklık denetleyicisi ile MEMS sensörünün vakum seviyesi paketinin tasarımını, modellenmesini, fabrikasyonunu ve karakterizasyonunu içerir. Tasarımın birincil amacı, MEMS sensörü için sıcaklık kontrollü bir ortam yaratmaktır. Bir sıcaklık kontrol yüzeyi oluşturmak için bir alümina malzeme seçilir. MEMS sensörü alümina tabanın üzerine konumlandırılır. Alümina taban üzerindeki ısıtma elemanları metal serilmesi ile oluşturulurken sıcaklık algılaması termistörler ile sağlanmaktadır. Paket, lehimleme yoluyla bir kapakla kapatılır ve iç boşluğu vakumlamak için bir bakır boru kullanılır. Kıstırma yöntemi, bakır boruyu kapatmak için kullanılır. Mevcut literatürden farklı olarak bu araştırma, sıcaklık kontrolünün yalnızca MEMS sensörü ile sınırlı olmadığını, aynı zamanda sinyal yükseltici devresini de kapsadığını öne sürmektedir. Bu nedenle alümina malzeme üzerinde oluşturulan trans-empedans yükseltici (TIA) devresi paketin arka tarafında, sıcaklık kontrol yüzeyinin karşı tarafında konumlandırılmıştır. Sonuç olarak, sıcaklık kontrol yüzeyi TIA devresi için de kullanıma hazır hale gelir.

Sistemin ısıl modelini anlamak ve kapalı çevrim sıcaklık kontrolörü elde etmek için analitik bir model geliştirilmiştir. Analitik modele ek olarak, sonlu elemanlar modeli (FEM) temel birkaç sebep ile oluşturulur. İlki, üretime başlamadan önce sistemin tasarım kontrolü ve ısıtma elemanlarının paketi stabilize edebilmesinin sağlanmasıdır. İkincisi, test verilerini kullanarak ısı transfer katsayısını elde etmek ve bununla sistemin zamana bağlı davranışını analiz etmektir. Son olarak, kapalı döngü sıcaklık kontrolörünü sonlu elemanlar analizinden kullanarak oluşturmaktır.

Sıcaklık kontrol yüzeyinin imalatı, trans-empedans yükselteç devresi, tüm elemanların uygulanması ve testleri ODTÜ MEMS Merkezi'nde yapılmaktadır. Test fazında, analitik model ve sonlu elemanlar modeli yaklaşımları kullanılarak MEMS sensörü tanımlanır. Sistem düzeyinde testler, çalışma sıcaklıkları bu aralık içinde tanımlandığından, 5 °C ile 35 °C arasında sıcaklık kontrolü olan ve olmayan bir iklim odasında gerçekleştirilir. 5 °C ile 35 °C arasında, MEMS sensörünün eş fazlı modunun rezonans frekansı, bir fırın kontrolü olmadığında 3120 Hz sapar. Tersine, kapalı devre bir sıcaklık kontrol cihazında rezonans frekansının sapması 380 Hz'dir. Benzer şekilde, sıcaklık kontrolörü olmadan faz dışı modun sapması 3140 Hz iken, sıcaklık kontrolörü ile 154 Hz'dir.

Anahtar Kelimeler: MEMS sensor, Sıcaklık telafisi, Fırın kontrolü, Sistem tanımlama, Kapalı döngü kontrolü

In solidarity with women fighting for their rights…

ACKNOWLEDGMENTS

I would like to express my sincere gratitude to my thesis supervisor Assoc. Prof. Dr. Kıvanç Azgın and my co-supervisor Assoc. Prof. Dr. Özgür Bayer for their guidance, support and recommendations throughout this thesis.

I would like to thank METU MEMS Center employees Batuhan Beşcan, Emre Ersoy, Ertuğ Şimşek and Murat Demirpolat for their assistance. I would like to thank Seyedmohsen Baghaei Oskouei for his support on the finite element analysis and valuable discussions for thermal model.

I would like to thank Bekir Gürel Dimez, Hasan Doğan Gavcar, Mertcan Sevinç, Sedat Mert, Seval Şahin, Orçun Tolga Şengöz and Oytun Demirörs for their technical help and their amazing friendship.

I would like to express my deepest gratitude to my family for their endless support. Finally, I would like to thank Ümit Doğan Dağlum for his love, support and patience throughout this journey, his humour made my challenges more enjoyable.

TABLE OF CONTENTS

LIST OF TABLES

TABLES

LIST OF FIGURES

FIGURES

CHAPTER 1

INTRODUCTION

Micro-Electro-Mechanical-Systems(MEMS) sensors show great promise for consumer electronics, medical, automotive applications, and other areas due to their small size and cost. The rising potentiality of the utilization of MEMS resonators in the application of frequency and time references necessitates appropriate evaluation metrics. MEMS resonators' performance metrics are the resonant frequency, quality factor Q, frequency stability, and motional impedance [1].

Resonant frequency, f_0: Depending upon the mechanical properties and physical parameters, a structure has natural frequencies. Resonant frequencies emerge at natural frequencies with large amplitude.

Quality factor, Q: The physical meaning of quality factor is the ratio of stored energy in the system to the dissipated energy of the system. A system with a low Q-factor means the dissipation of energy is high. Multiple mechanisms affect the total quality factor. These are gas damping, anchor loss, surface losses, electrical damping, intrinsic losses, and thermoelastic dissipation (TED).

Motional Impedance, Z_m: Motional impedance refers to the relation between the input voltage and output current of a resonator system.

Frequency Stability: It is desired to have a stable frequency signal for timing and frequency reference applications. The accuracy and consistency of the signal defines system reliability. Stability is generally stated as a variation from the target frequency and it is represented by parts per million (ppm) or parts per billion (ppb). The frequency stability can be examined in three sections: long-term, medium-term, and short-term stability [2]. Long-term stability is also known as aging, and it is the measurement of frequency stability over hours to months. The medium-term stability range includes seconds to hours, and it is generally affected by temperature deviations. It is also expressed as temperature stability. Short-term stability is the noisy effect of frequency in the range of seconds.

To analyze the frequency stability, statistical methods can be used. Yet, standard deviation calculation is not appropriate for frequency sources due to non-convergent behavior. Allan variance is a convergent solution for this problem. Allan variance is calculated as below:

$$\sigma_y^2(\tau) = \frac{1}{2(m-1)} \sum_{i=1}^{m-1} (y_{i+1} - y_i)^2 \qquad 1.1$$

where m refers to measurement number, τ refers to sampling time, and y_i refers to each frequency measurement. Hence, Allan deviation is expressed as:

$$\sigma_y(\tau) = \sqrt{\frac{1}{2(m-1)} \sum_{i=1}^{m-1} (y_{i+1} - y_i)^2} \qquad 1.2$$

1.1 Environmental Effect on MEMS

MEMS sensors have become a viable option for defense, position sensing, and navigation applications because of the rapid advancements in technology. However, sustaining the optimal performance of MEMS sensors remains a significant challenge. Solutions for sustaining the performance depend on the insulation of sensors from environmental effects. These environmental effects can be sorted as temperature, vibration, stress, and shock [3]. This subsection reviews temperature effects on MEMS sensors.

The resonant frequency of MEMS sensors is highly dependent on the temperature since the thermophysical properties of the material change with temperature. These material properties can be exemplified by Young’s modulus and thermal expansion coefficient. Additionally, size change due to thermal expansion causes changes in the resonant frequency. Because of the size change, the gap between the capacitive electrodes can change and impact the electrostatic stiffness. Furthermore, temperature-induced mechanical stress influences the applied load on the MEMS sensor, which affects the frequency. The quality factor is also highly dependent on the temperature and the changes on quality factor is related to the changes in frequency [2].

Hence, one of the performance metrics affected by temperature is frequency stability and temperature coefficient of frequency (TCF) term is used for defining the thermal frequency stability. It is desired to have a zero TCF and the following section discusses temperature compensation methods for achieving this objective.

1.2 Overview of Temperature Compensation Methods for MEMS Sensors

Temperature compensation methods to decrease TCF can be divided into passive and active compensation techniques. Passive compensation techniques involve building composite structures, doping, and geometry engineering [1]. In these techniques, the resonator's characteristics have been built such that the temperature coefficient of frequency is reduced. One of the reasons behind the temperature dependence of frequency is the temperature coefficient of elasticity of the material used. Different materials with opposing coefficient of thermal expansion (CTE) values can be selected in the composite structure method to decrease the temperature effect on the resonator. The material selection brings cancellation of CTE. In 2005, a film bulk acoustic resonator (FBAR) is presented with two different temperature compensation methods [4]. One of them includes integrating an air-gap capacitor to reduce the TCF and using AlN rather than ZnO to achieve zero TCF. The second solution for temperature compensation of FBAR depends on building a SiO_2 layer and reaching -0.45 ppm/˚C. Melamud et al builds a composite structure consisting of silicon and silicon dioxide to reach zero linear TCF in 2009 [5]. They reported that the composite resonators have a quadratic TCf of -20 ppb/˚C^2. In 2010, Myers presented a passive temperature compensation method for DETF resonators built with silicon carbide (SiC) and silicon for strain-sensing applications [6]. In 2013, Clark et al achieve a reduction in TCF from -16 ppm/˚C to -0.1 ppm/˚C by creating polysilicon and silicon dioxide layers for overtone resonators [7]. In the same year, a composite resonator structure was built with oxide-refilled trenches, and they achieve a high-Q resonator with a low-temperature coefficient of frequency of 2 ppm/˚C [8]. In 2019, lithium-niobate on silicon dioxide (LN-OX) platform is used for implementing MEMS resonator array [9] They study active compensation methods besides this passive compensation method which brings 15.2 ppm/K.

Doping is the second method for passively compensating for the temperature effect on resonators. In 2009, Samarao and Ayazi reported that degenerate doping of silicon brings a reduction in the temperature coefficient of frequency [10]. That was the first temperature compensation method that uses free charge carriers on elastic constants of silicon, and they achieve a reduction in TCF from -29 ppm/˚C to -1.5 ppm/ ˚C. In 2020, Ma et al developed a surface acoustic wave device composed of scandium-doped AlN and phosphorus-doped silicon [11]. Doped silicon is used for temperature compensation material, and they arrange SAW resonators at 75˚ in <110> direction on a silicon wafer to achieve zero first-order. Chen et al reported a piezoelectric MEMS resonator built from scandium-doped aluminum nitride on silicon [12]. The reported MEMS resonator has a ±21.5 ppm frequency variation from -40 ˚C to 85 ˚C.

One of the passive temperature compensation methods is geometry engineering. In 1998, Hsu and Nguyen introduced a design technique for the temperature compensation method of micromechanical resonators [13]. In their design, suspending beams' lengths differ such that beams are imposed upon different ratios of expansion/distraction depending on the temperature change. With the help of this design strategy, cancellation of frequency shifts could be achieved from 27 ˚C to 127 ˚C. Passive temperature compensation methods rely on geometry engineering given in [14]–[16].

On the other hand, active compensation techniques include electrostatic tuning, electronic compensation, and micro-oven control methods. The electrostatic tuning method relies on the relation between bias voltage and frequency of a resonator. In 2005, Sundaresan et al reports a temperature-compensating bias circuitry that resulted in 2 ppm/˚C [17]. Ho et al applied the electrostatic tuning method to I-shaped bulk acoustic resonators in 2010[18] and resulted in 39 ppm over 100˚C. Their electrostatic tuning strategy comes from the relation between the structure's dynamic stiffness and voltage. In 2011, Lee et al presents an active compensation method using electrostatic tuning [19]. Their electrostatic tuning method uses a sensor to measure the resonator temperature and with the help of the lookup table, they arrange the bias voltage concerning changing ambient temperature. They achieve ±2.5 ppm temperature stability over a 90˚C temperature range. Moreover, again in 2011, Serrano et al. used electrostatic tuning for a piezoelectric MEMS resonator and reported a full temperature compensation between -25˚C to 100˚C [20]. In 2017, Shin et al. used the electrostatic tuning method for disk-shaped resonators [21]. Their method stands on arranging mode shapes via applying bias voltages.

The other active temperature compensation method is electronic temperature compensation. In 2007, Sundaresan presented a temperature compensation method for silicon IBARs [22]. They reported a frequency drift of 2830 ppm over 100˚C for an uncompensated oscillator while it is 39 ppm for the compensated oscillator. They were built proportionally to absolute temperature circuits. In 2012, Perrot et al. used a temperature-to-digital converter for compensation [23]. They used a thermistor close to MEMS resonator in the CMOS die, resulting in ±0.5 ppm frequency stability for -40 to 85˚C. Wu et al reported a piezoelectric resonator in 2018 [24]. Their temperature compensation method includes both active and passive strategies. While a composite structure was used for passive compensation, a temperature sensor and PLL circuit were used for active compensation. They packaged the MEMS resonator and the integrated circuit together.

Finally, the oven control strategy for temperature compensation relies on Joule heating of heaters located near to MEMS resonator and stabilizes the operating temperature. Nguyen and Howe reported one of the initial works on micro oven control for a resonator in 1993 [25]. In 2006, Sundaresan et al presented a temperature compensation method for silicon Bulk Acoustic Wave resonators [26]. Their oven control method gave direct current to the resonator while the temperature control circuit included a reference voltage generator and CTAT generator. They improved the temperature stability by 52x and reported frequency stability of 56 ppm over 100 ˚C. In 2008, a detailed thermal analysis is studied for the oven control method of MEMS resonators [27]. Jha et al. designed a MEMS DETF resonator with an in-built heater, and they modeled the thermal resistances of the heater and DETF system as one-dimensional. However, their analytical model result was 20% different than FEM and measurement results.

In 2009, Lee et al. presented a vacuum packaging application for a MEMS device that includes an oven-controlled system and vibration isolation platform [28]. Temperature control was provided by a heater and a temperature sensor placed on the isolation platform. To minimize the power dissipation for the heated structure, glass isolation suspensions, anti-radiation shield, and vacuum encapsulation was used. In the fabrication of this application, metal lines were formed by Ti/Pt/Au layers on the glass wafer. The oven control set temperature was determined as 80˚C and drive frequency stability was 0.96 ppm/˚C from -30˚C to 70˚C temperature range while it is 17.3 ppm/ ˚C for uncompensated design. They enhanced the oven control compensation by arranging the operating temperature regarding the environment temperature which resulted in 0.22 ppm/ ˚C. The maximum power consumption reported in this work is 33.1 mW for 80 ˚C.

Lim et al. presented a solution for OCXO's frequency instability caused by varying ambient temperatures in 2010 [29]. Also, the packaging size and power consumption of OCXO were aimed to be improved. The oscillator, heater, temperature sensor, and op-amps were placed on a CMOS chip. Hence, the package size of OCXO is reduced which brings less power consumption and a shorter warm-up time. The heater used in this design has a maximum power consumption of 1.16 W with a 3.3V power supply. In this paper, to make a connection between the heater current and the chip temperature, measurements were taken at different temperatures and the heater current was manually adjusted. A thermal model was not declared. The temperature control circuit of this system can be classified as a bang-bang controller. Frequency stability is reported as ±0.35 ppm from 0˚C to 60˚C.

In 2010, Salvia et al. worked on MEMS oscillators' temperature stability [30]. To enhance their limits, OCXO's oven control approach was applied in this paper with a new PLL-based controller. The designed MEMS structure has three main parts. These are hermetic encapsulation, folded beam micro-oven, and two double-ended tuning-fork resonators. Hermetic encapsulation brings two benefits; one of them is that a low-pressure environment provides air damping less significant for 1 MHz range resonators. And the other one is; heat loss can be minimized through gas conduction and convection which brings low power operation. Folded beam structure for micro-ovenization provides stiffness and thermal isolation. Finally, there are two double-ended tuning forks and their design parameters are slightly different to implement different thermal characteristics. Yet, their resonant frequencies are close to each other. This design provides high-resolution data for the temperature of resonators thanks to the different temperature characteristics of the two resonators. They resulted with ±1 ppm from -20˚C to 80˚C and reported 15-20 mW power consumption for micro-oven.

In 2005, Wojciechowski et al. reported an oven-controlled oscillator in two parts [31], [32]. In the first part, they started with the design and fabrication of the micromechanical oscillator while in the second part, they introduced characterization and measurements. They used AlN resonators on a suspended platform integrated with CMOS. They reported -1.2 ppm/˚C frequency stability from 0˚C to 80˚C. Xu et al. stated that to achieve high efficiency for the ovenization of resonators, high thermal resistances are needed in the anchors of the resonators [33]. However, increasing the thermal resistance cause an increase in the motional resistance which causes a decrease in the quality factor. Therefore, they came up with two essential approaches for this trade-off. One of them was separating the RF power delivery from the resonator's supporting structures to have the flexibility to design thermal resistances. Secondly, they introduced a dummy resonator to create uniform temperature distribution across the resonator. They reported 100 ppm frequency stability over 120˚C with 0.53 mW heater power dissipation. In 2018, Liu et al. enhanced a MEMS oscillator's frequency stability oven controlled system [34]. The method used in this paper leans on the structural resistance of silicon resonators. The heater and resonator are placed on the same die. When the system is integrated with micro-oven control, frequency drift is dropped from 3000 ppm to ±2.5 ppm. After digital calibration, frequency stability navigates through ±0.25 ppm. They achieved the highest "frequency stability improvement factor" at the time.

In 2019, Liu et al. developed an oven control system to compensate for the temperature effect on the MEMS pressure sensors [35]. They used heaters separately in the thermal platform under the MEMS sensor for the oven controlled system.

The compensation function for the ambient and the set temperature is implemented for the analytical model. A compensation function is produced to overcome the ambient temperature effects. They built an electrical equivalent model for a thermal system and used this model in their compensation function. The heater in this system is controlled with PWM and ambient temperature is detected by the second temperature sensor in the cap. The temperature control accuracy is reported as ±0.2˚C from -45˚C to 45 ˚C.

In 2019, Yang presented a thesis for improving the performance of MEMS inertial sensors against changing environmental effects [3]. Firstly, one isolation stage with an oven-controlled inertial sensor was designed. The isolation stage is made of glass, and it has a suspended structure. A commercial IMU was placed on stage, and they vacuum packaged to the LCC. To overcome the problems coming from SOCIS; a new solution, a double-isolation stage oven-controlled inertial sensor (DOCIS) was presented. In this design, the isolation stage is made of silicon rather than glass which reduces the temperature gradient. However, there should be a second isolation stage for thermal isolation and this one is made of cross-linked polyamide aerogel.

Moreover, in 2019 Kwon et al. presented an oven controlled MEMS oscillator (OCMO) [36]. Their oven control environment only involved the resonator body and for the temperature measurement, they used resonant frequency change of the oscillator. They decided the ovenization point from the temperature dependence of the frequency as 70˚C. They presented steady-state measurements between -40˚C and 60 ˚C and enhanced the temperature stability by 73000. Their OCMO is highly competitive with the OCXO market.

In 2020, Ortiz et al. reported a DETF resonator, and a Lamé-Mode resonator integrated with an on-chip heater [37]. They tested the resonators in the ambient temperature range of -40˚C to 60˚C at the turnover temperature. Lamé-Mode resonator showed temperature stability of ±1.5 ppb over temperature which highest frequency stability value ever reported. Moreover, they repeated their tests by locating trans-impedance amplifiers inside and outside of the temperature control chamber to understand the temperature dependence of them. It was observed that locating TIAs inside the oven chamber significantly improves the frequency stability and decreases the bias instability.

In 2021, Zhao et al. studied oven control systems for hemispherical resonator gyroscopes [38]. They used a resistance temperature detector as a temperature sensor and for the first time, the voltage output of it converted to the frequency signal to decrease the effect of environmental changes. Jia et al. presented a piezoelectric MEMS resonator in 2022 [39]. It is stated that a AlN deposited MEMS resonator operating dual-mode is presented for the first time. Their temperature sensing mechanism relied on the dual-mode operation of the resonator. It is reported that the frequency stability was ±400 ppb in the temperature range of -40˚C to 80˚C.

1.3 Research Objectives and Thesis Structure

It is essential to minimize the impact of varying external conditions on MEMS devices to achieve stability and reliability. The temperature effect is one of the most significant factors in the performance of MEMS devices. The main objective of this is to design a temperature control environment for a vacuum packaged MEMS sensor and utilize this environment for its trans-impedance amplifier. The methodology used for temperature compensation is oven control. Hence, the design is named as "Oven Controlled Package". In light of this information, the following are the objectives of this study:

1. Designing a temperature control surface which includes heating elements and temperature detection areas. The proposed heating elements should have sufficient power to stabilize the package above ambient temperature. That surface should also be compatible with the MEMS fabrication.
2. A thermal model should be built mathematically while observing the system's behavior with different thermal resistances and capacitances. A numerical model based on the finite element method should be constructed for characterizing the thermal behavior of the system.
3. Preparing a process flow for the fabrication and assembly procedures.
4. Realizing characterization tests and finalizing the thermal model with test results. Building a closed-loop temperature controller from the thermal model, which is built both analytically and by FEM. Observing the frequency response of the resonator with and without a temperature controller.

The following is a summary of the content and organization of this thesis:

Chapter 2 presents the mathematical model of the thermal and electrical system of the oven controlled package. The finite element model is also presented in this section.

Chapter 3 describes the fabrication procedure of the alumina based temperature control surface, alumina based trans-impedance amplifier circuit, implementation of all the elements, and assembly procedures. The vacuum packaging method and seal test are detailed.

Chapter 4 presents the characterization tests of the package. A plant identification procedure is carried out from an analytical model and a finite element model. A closed-loop temperature controller is integrated into the system. Frequency response tests of the MEMS DETF resonator with and without a closed-loop temperature controller are performed. Results from the system-level tests are compared.

CHAPTER 2

DESIGN OF OVEN CONTROLLED PACKAGE

In this chapter, the design of the oven control package is introduced to compensate the temperature change effect in the MEMS packages. Section 2.1 introduces the elements of the package. Analytical modeling and finite element modelling are presented in Section 2.2 and Section 2.3, respectively. In Section 2.4, the MEMS sensor located in the package is introduced with an analytical model and FEM analysis. The chapter is finally summarized in Section 2.5

2.1 Components of the Oven Controlled Package

The methodology used for temperature compensation relies on creating an oven controlled environment which stabilized the temperature of the MEMS sensor when the environment conditions are changing. A package design is built for that purpose and it is named as oven controlled package.

Oven controlled package design starts with selecting the MEMS package and it is constrained by the size of the MEMS sensor which will be used in future work. All of the other elements in the package are constrained by the MEMS package chosen. The MEMS package used in this thesis is Spectrum HYB04004 whose solid model can be seen in Figure 2.1.

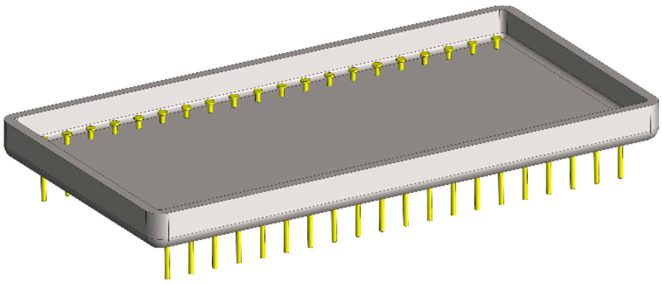

Figure 2.1. Spectrum Hybrid Package 4004.

The attachment of the MEMS sensor to the package should be sustained with an intermediate plate to create a temperature control surface. An alumina wafer is selected for building the temperature control surface of the MEMS sensor. The reason for choosing alumina material here is that the thermal expansion coefficients of kovar and alumina are close to each other and the low thermal expansion coefficient of alumina also creates a suitable thermal coupling for the silicon-based sensor being produced.

The alumina base needs to have a few key components on the surface. The heater area is one of them, followed by the temperature detecting region and, finally, the MEMS sensor attachment area as shown in Figure 2.2.

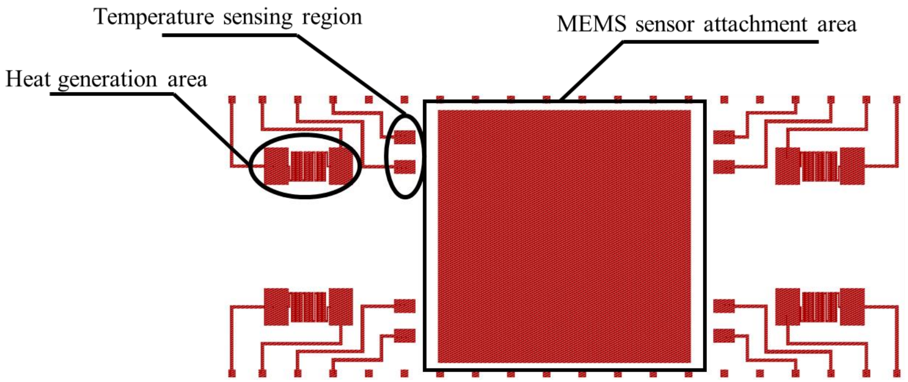

Figure 2.2. Alumina base layout for temperature control surface

The alumina base's location in the package is given in Figure 2.3.

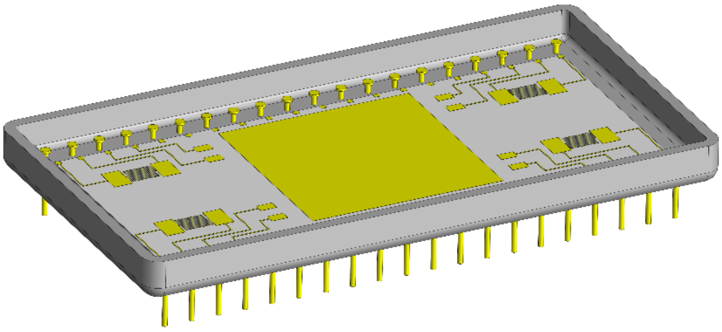

Figure 2.3. Alumina base placement on the package.

Another package with a sealed copper tube is used to prepare the package for vacuum packaging, the sealed package is demonstrated in Figure 2.4. A cross-section view of the oven controlled package is presented in Figure 2.5.

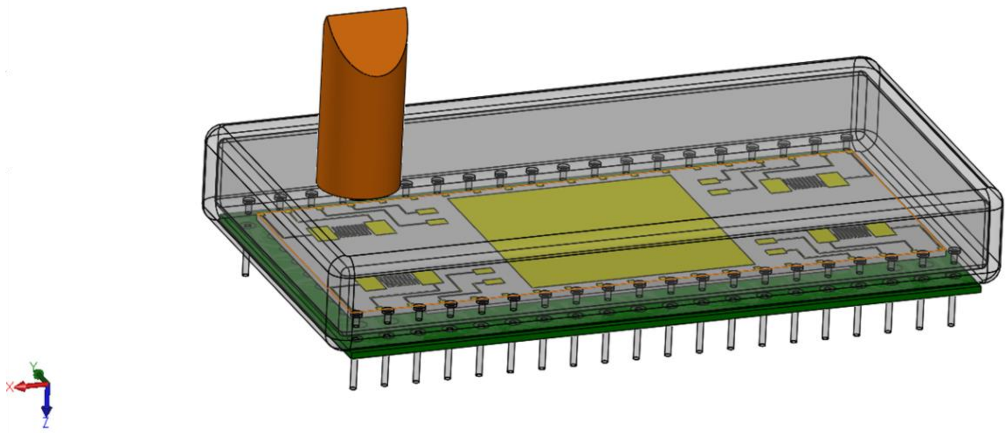

Figure 2.4. Demonstration of the sealed oven control package.

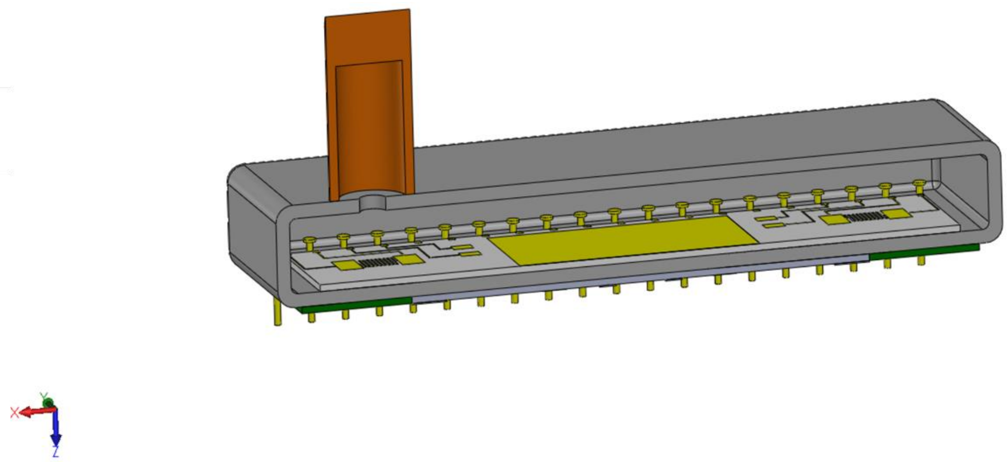

Figure 2.5. Cross-section view of the oven controlled package.

A PCB and alumina based trans-impedance amplifier (TIA) circuit is designed and placed right behind the package to obtain a connection with the inside of the package and utilize the temperature control environment for the TIA as well. The complete model of the package is presented in Figure 2.6.

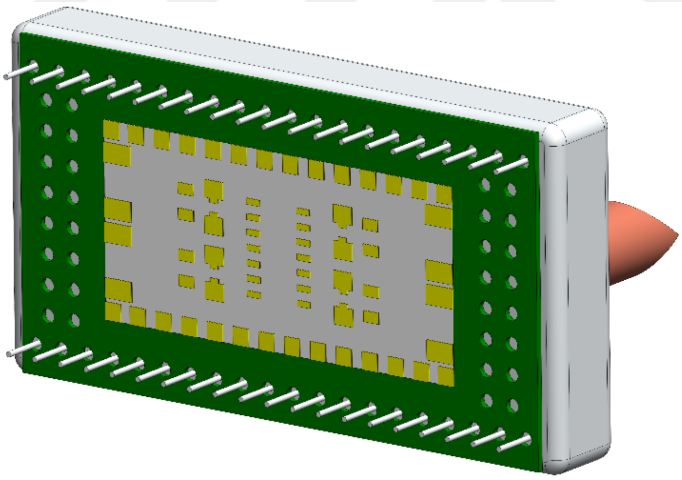

Figure 2.6. The complete model of the package.

Fabrication and assembly details of the packaging will be given in CHAPTER 3.

2.1.1 Heat Generating Elements

The design of heat-generating elements is discussed in two aspects. One of them is using surface mount resistors, and the other one is depositing and patterned metal material to obtain a resistor structure. In the case of using SMD (surface mount device) resistors, a metallization is also required to create a mounting region. Therefore, the pad size of the SMD resistor must be included in the design parameters of the heat-generating elements. Forming the resistor unit by metallization only is determined by the distance between the solder pads of the SMD resistor used in the first option. Other design parameters of the heat generating element were defined by fabrication restrictions. Finally, the metallization pattern can be seen in Figure 2.7.

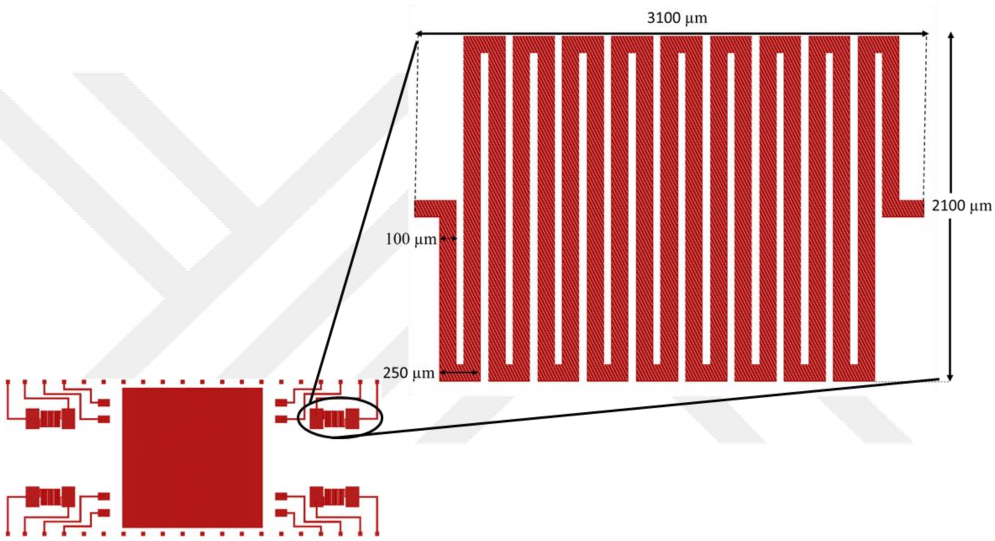

Figure 2.7. Heat generation elements.

When selecting the metal needed to shape the pattern, the metal material’s temperature coefficient of resistance (TCR) should be considered. The material's TCR shouldn't vary significantly with temperature. To satisfy this condition, the temperature-dependent electrical resistance of several different metals was investigated. The electrical resistance of gold, copper, chromium, aluminum, platinum, and titanium tungsten over a temperature range of 0°C to 100°C calculated and presented in Figure 2.8. Although platinum is commonly used in oven control designs, it is not used in this thesis' design due to the significant change in resistance with temperature. As a result, TiW and Cr were chosen for the adhesion layer, and Au and Cu were chosen for the signal carrying lines.

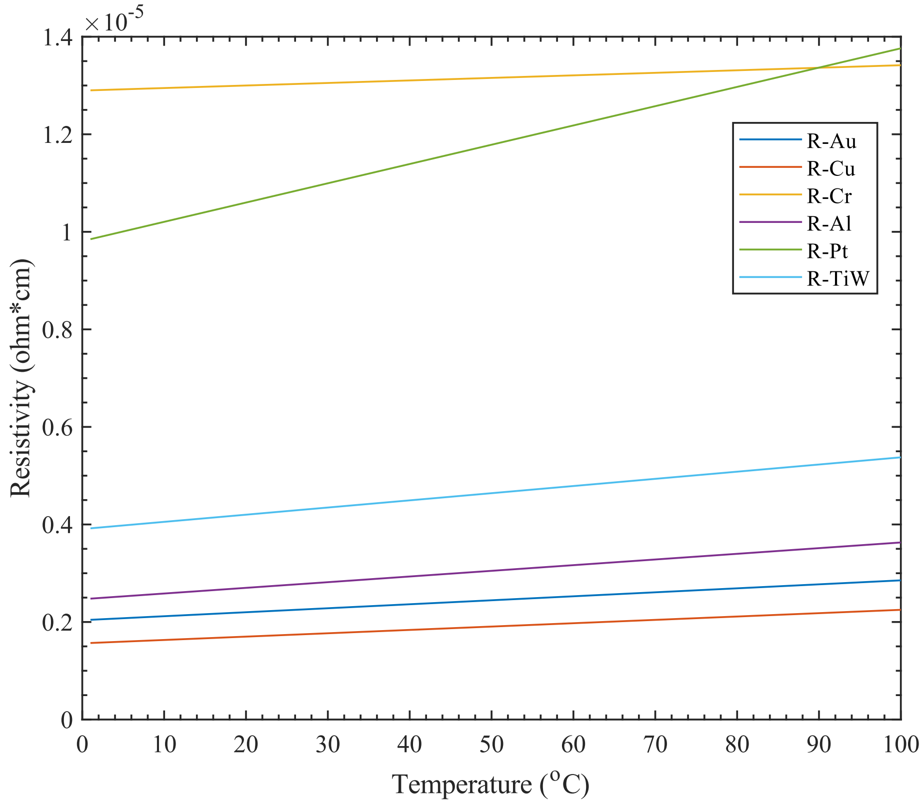

Figure 2.8. Resistivity changes of metals.

2.1.2 Temperature Sensing Elements

The temperature sensing elements used in this thesis are MURATA Manufacturing NCU18WF104 series negative temperature coefficient (NTC) thermistors. The resistance of thermistors decreases as the temperature rises. The datasheet of the thermistors includes resistance values for the -40 to 125 °C temperature range. Figure 2.9 shows resistance curvature as a function of temperature between 0 and 125 °C. The resistance behavior of the thermistor as temperature changes can be found by fitting the curve in the figure, and it is expressed as:

$$R_{thermistor}(T_S) = 9\,x\,10^{-10}\,x\,T_S^6 - 4\,x\,10^{-7} x\,T_S^5 + 8\,x\,10^{-5}\,x\,T_S^4 - 0.0082\,x\,T_S^3 + 0.5117\,x\,T_S^2 - 18.996\,x\,T_S + 356.45 \quad 2.1$$

In Equation 2.1, T_S refers to the sensing location temperature and $R_{thermistor}(T_S)$ is stated for the resistance function of temperature.

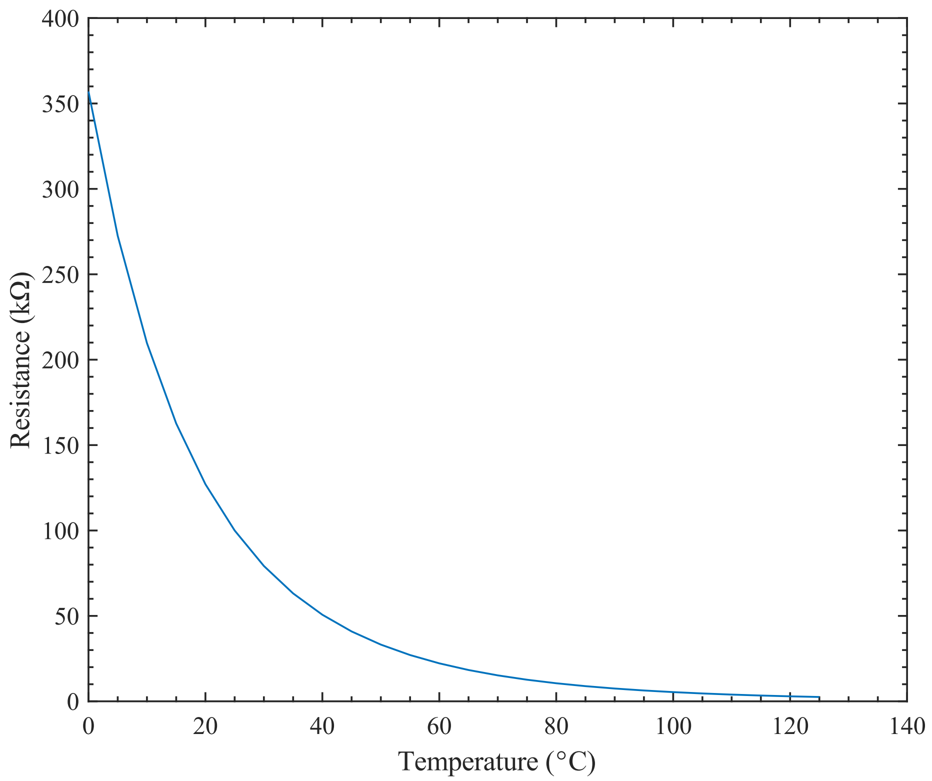

Figure 2.9. The resistance change of the thermistors with changing temperature.

Resistance-temperature relation of the thermistors is used when building an analytical model.

The common circuit diagram for thermistors is demonstrated in Figure 2.10. To read the voltage of the thermistor, a simple voltage divider circuit is used. V_{RT} represents the thermistor's voltage, while R_T represents its resistance. R_S denotes a serially connected resistance, and V_R denotes the voltage across it. The serially connected resistance selected belongs to Vishay Foil Resistors VSMP series 2010. Its resistance tolerance is ±0.01. While the resistance on the thermistor changes with temperature, resistance connected in series shouldn't change with temperature to accurately measure the thermistor resistance. This serially connected resistance is located in the trans-impedance amplifier circuit board behind of the package.

To evaluate the temperature, firstly voltage should be detected from the A0 node. When the voltage V_{RT} is measured from the point denoted by A0 in the tests R_T value can be obtained as:

$$R_T = \frac{V_{RT}}{V_R/R_S} \quad 2.2$$

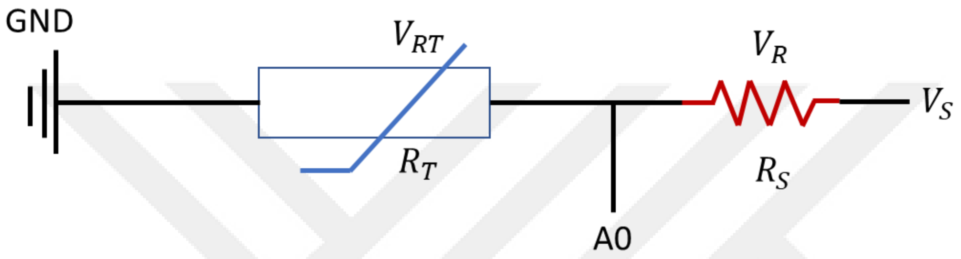

Figure 2.10. Circuit diagram of thermistors.

Equation 2.3 can also be used to simplify temperature calculations from measured voltage, while R_0, β, and $T0$ is specified in the datasheet of the thermistor. Finally, the temperature is evaluated from Eq. 2.4.

$$R_T = R_0 e^{\beta\left(\frac{1}{T}-\frac{1}{T0}\right)} \quad 2.3$$

$$T = \frac{1}{\frac{\ln\left(\frac{R_T}{R0}\right)}{\beta} + \frac{1}{T0}} \quad 2.4$$

Figure 2.11 depicts the locations of the temperature sensing points, which are designated as T_{h1}, T_{h2}, T_{h3}, and T_{h4},. They will be cited by these names in the thesis.

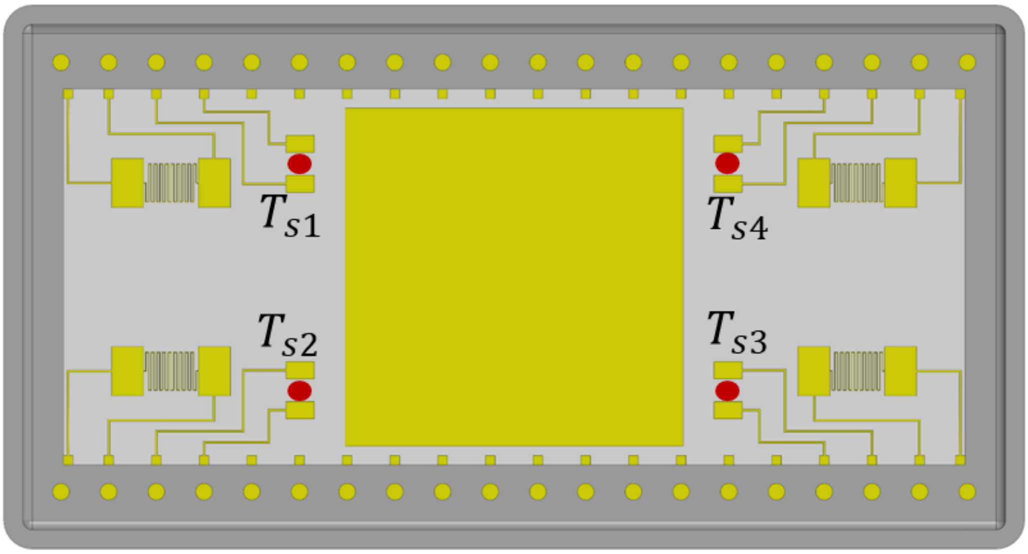

Figure 2.11. The location of the temperature sensing points.

2.1.3 Trans-impedance amplifier circuit

The trans-impedance amplifier circuit is designed to read the signal coming from the MEMS sensor and provide the connections for the thermistors inside the package. The circuit can be seen in Figure 2.12. R_s refers to the mounting region of the resistance that is serially connected to the thermistor, Op-amp refers to the mounting area of the op-amp AD8608. Finally, R_{opamp}, C_{opamp} refers to the mounting region of the resistor and capacitor. The designed circuit board is symmetric with respect to the center of the Op-amp. The material for the trans-impedance amplifier circuit board is selected as alumina which is the same material that is used inside the package to enhance the temperature control region around the TIA circuit.

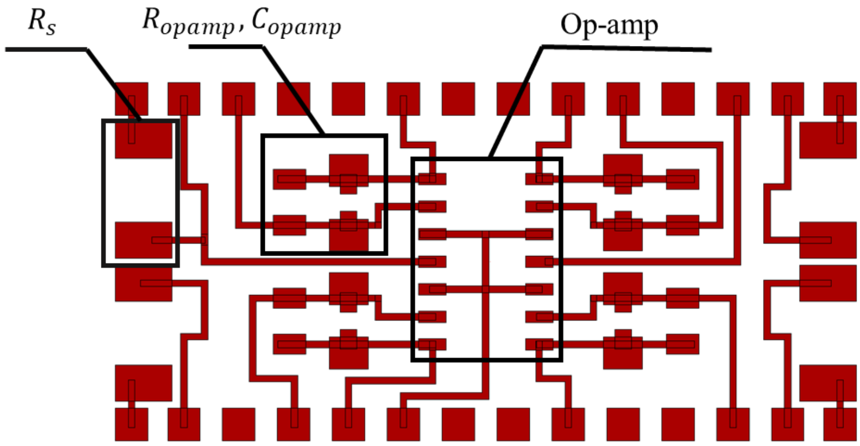

Figure 2.12. Trans-impedance amplifier circuit.

2.1.4 PCB of the Package

A PCB is designed to provide the voltage input and signaling required by the package's elements. The designed PCB can be seen in Figure 2.13. This PCB is integrated with the Trans-impedance amplifier circuit board. The top surfaces of the PCB and TIA circuit board should be aligned for signal transmission.

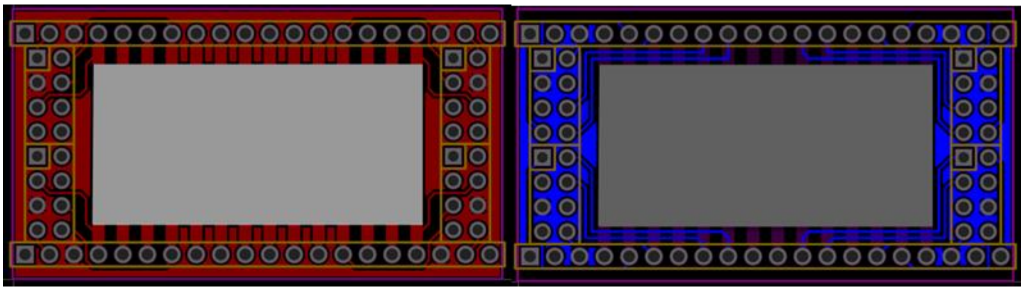

(a) (b)

Figure 2.13. PCB of the package. (a) Top Layer, (b) Bottom Layer

2.2 Modelling of the Package System

Electrical and thermal models of the oven-controlled package are created to better comprehend the system's behavior.

2.2.1 Thermal Model of the System

In the thermal modeling of the system, every heating element with a nearby thermistor is treated as a pair. There are four heater-thermistor couples in the package. Those couples are demonstrated in Figure 2.14.

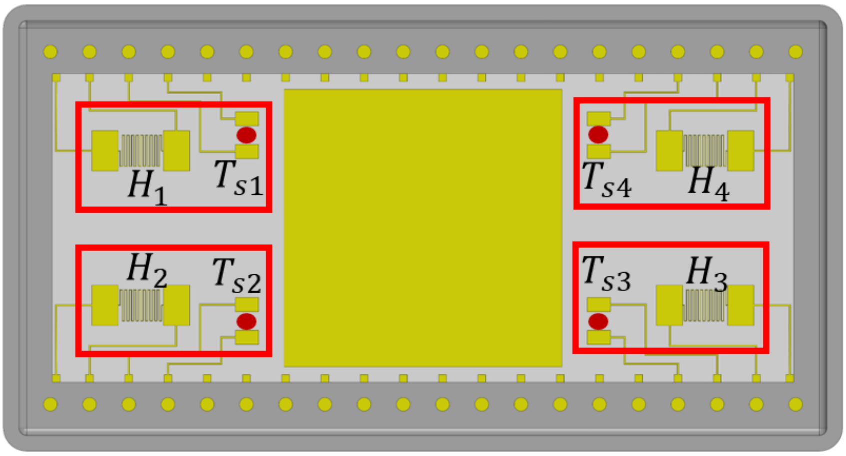

Figure 2.14. Four heater-thermistor couples are considered for thermal modeling.

One of the couples is taken into consideration in the thermal modeling of the sensing locations which is demonstrated in Figure 2.14. To obtain a thermal model, various assumptions were made while establishing a control volume on the alumina die. Firstly, it is assumed that the heater coincides with the sensor point. It is therefore anticipated that the sensor will take in all the generated heat that the heaters create. Additionally, the ambient temperature is thought of as a heat sink in which all of the heat produced is transferred. Each couple is modeled as a one-dimensional, lumped system. Figure 2.15 demonstrates the thermal model.

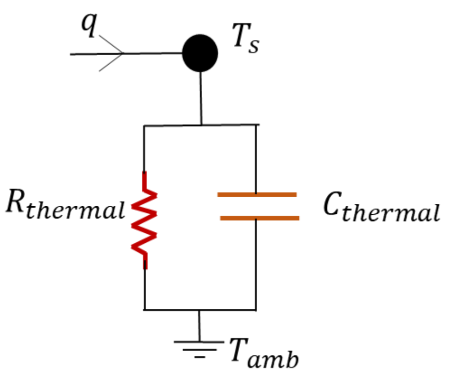

Figure 2.15. Thermal model of one of the heater-thermistor couples.

Thermal resistance and capacitance can be expressed as follows [40]:

$$R_{thermal} = \frac{Temperature\ difference\ btw\ T_s\ and\ T_{amb}}{Change\ in\ heat\ flow\ rate} \frac{°C}{J/s} \qquad 2.5$$

$$C_{thermal} = \frac{Change\ in\ heat\ stored}{Change\ in\ temperature} \frac{J}{°C} \qquad 2.6$$

T_s refers to the temperature of the sensing location, T_{amb} stands for the ambient temperature and q refers to the heat flow rate. $R_{thermal}$ corresponds to the thermal resistance between the location of heat generation and the surrounding temperature. As a result, it includes all of the package's layers. $C_{thermal}$ is the thermal capacitance between the heat generation location and the ambient temperature. Similarly, $C_{thermal}$ involves all the layers of the package.

When heaters begin to operate with constant power, it can be assumed that thermal capacitance dominates the thermal resistance at the initial time. As the system approaches a steady-state with constant power dissipation, heat flow through the thermal resistance rises. Moreover, it is assumed that the thermal resistance and thermal capacitance do not vary between operation temperatures. The heat equation for the thermal capacitance can be expressed as follows:

$$C_{thermal} \frac{dT}{dt} = q_{capacitance} \qquad 2.7$$

$$C_{thermal}(T_S - T_{amb}) = \int q_{capacitance}\, dt \qquad 2.8$$

From these equations, the temperature of the sensing location becomes:

$$T_S = \frac{\int q_{capacitance}\, dt}{C_{thermal}} + T_{amb} \qquad 2.9$$

The heat flow rate on the thermal resistance can be written as follows:

$$q_{resistance} = \frac{T_S - T_{amb}}{R_{thermal}} \qquad 2.10$$

Heat flow rate on the thermal capacitance will be:

$$q_{capacitance} = q - q_{resistance} \qquad 2.11$$

Moreover, an electrical system analogy can be constituted with the thermal model. The thermal impedance, $Z_{thermal}$ of the system can be stated as

$$Z_{thermal} = \left(R_{thermal} + \frac{1}{C_{thermal}s}\right)^{-1} \qquad 2.12$$

$$Z_{thermal} = \frac{C_{thermal}s}{1 + R_{thermal}C_{thermal}s} \qquad 2.13$$

The difference in temperature in a thermal system is analogous to the difference in voltage in an electrical system.

$$(T_s - T_{amb}) = q * Z_{thermal} \qquad 2.14$$

$$T_S = q\frac{C_{thermal}s}{1 + R_{thermal}C_{thermal}s} + T_{amb} \qquad 2.15$$

In these equations, $R_{thermal}$ and $C_{thermal}$ can be calculated experimentally. In the experiments, $R_{thermal}$ and $C_{thermal}$ are determined such that they are satisfying all the temperatures in the operation range. The details are discussed in CHAPTER 4.

2.2.2 Electrical Model of the System

An electrical model of the system is created regarding one of the heater-thermistor pairs. The objective of the electrical model is to obtain the electrical resistance of the thermistors and use this information to calculate the temperature value at thermistor locations.

The voltage inputs to the heating elements and thermistors are distinct in the package. However, their grounds are common. Hence, thermistors' electrical response should be considered together with the heaters. In addition, wire bonds and cable resistances should be included in the electrical model. Figure 2.16 illustrates the electrical model of the package. Parameters are specified in Table 2.1. Ohm's Law is used to compute the current values presented in Figure 2.16.

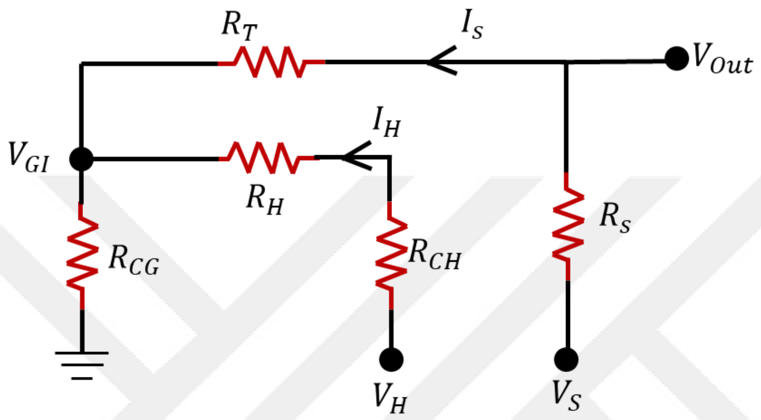

Figure 2.16. Electrical model of one of the heater-thermistor pairs.

Table 2.1. Electrical model parameters

Symbol	Parameter
V_H	Voltage input of heater
V_S	Voltage input of the resistance connected with thermistor
V_{GI}	Voltage of the shared ground when heaters are actuated
R_T	Resistance of the thermistor
R_H	Resistance of the heater
R_{CG}	Resistance of the ground cable from the package to power supplies
R_{CH}	Resistance of the cable from the power supply to the input pad of the heater

$\boldsymbol{R_S}$	Resistance of the resistor in the voltage input
$\boldsymbol{I_S}$	Current on the thermistor
$\boldsymbol{I_H}$	Current on the heater

The current on the thermistor I_S can be written as follows,

$$I_S = \frac{V_S - V_{GI}}{R_S + R_T} = \frac{V_S - (I_S + I_H)R_{CG}}{R_S + R_T} \quad 2.16$$

$$I_H = \frac{V_H - V_{GI}}{R_{CH} + R_H} = \frac{V_H - (I_S + I_H)R_{CG}}{R_{CH} + R_H} \quad 2.17$$

$$V_{OUT} = V_S - I_S R_S \quad 2.18$$

Moreover, voltage value at V_{GI} will be calculated as:

$$V_{GI} = (I_S + I_H)R_{CG} \quad 2.19$$

V_{GI} can be written explicitly as:

$$V_{GI} = \frac{V_S R_{CG}}{R_S + R_T} - \frac{V_{GI} R_{CG}}{R_S + R_T} + \frac{V_H R_{CG}}{R_{CH} + R_H} - \frac{V_{GI} R_{CG}}{R_{CH} + R_H} \quad 2.20$$

$$V_{GI}\left(\frac{1}{R_{CG}} + \frac{1}{R_{CH} + R_H} + \frac{1}{R_S + R_T}\right) = \frac{V_H}{R_{CH} + R_H} + \frac{V_S}{R_S + R_T} \quad 2.21$$

To simplify the calculation:

$$\left(\frac{1}{R_{CG}} + \frac{1}{R_{CH} + R_H} + \frac{1}{R_S + R_T}\right) = A \quad 2.22$$

$$R_{CH} + R_H = B \quad 2.23$$

$$R_S + R_T = x \quad 2.24$$

$$V_{GI} = \frac{V_H}{AB} + \frac{V_S}{Ax} \quad 2.25$$

Equation 2.25 is implemented into Equation 2.16.

$$I_S = \frac{V_S}{x} - \frac{V_S}{Ax^2} - \frac{V_H}{AxB} \quad 2.26$$

$$I_S = \frac{V_S\left(\frac{Bx}{R_{CG}} + B + x\right) - V_S B - V_H x}{x^2 AB} \quad 2.27$$

$$I_S = \frac{V_S\left(\frac{B}{R_{CG}}+1\right)-V_H}{\left(\frac{B}{R_{CG}}+1\right)x+B} \qquad 2.28$$

After calculating the current I_S, V_{OUT} can be expressed with putting the Equation 2.31 into the Equation 2.18.

$$V_{OUT} = V_S - R_S\left(\frac{V_S\left(\frac{B}{R_{CG}}+1\right)-V_H}{\left(\frac{B}{R_{CG}}+1\right)x+B}\right) \qquad 2.29$$

$$\frac{V_S - V_{OUT}}{R_S} = \frac{V_S\left(\frac{B}{R_{CG}}+1\right)-V_H}{\left(\frac{B}{R_{CG}}+1\right)x+B} \qquad 2.30$$

$$\left(\frac{B}{R_{CG}}+1\right)\ x = \frac{V_S\left(\frac{B}{R_{CG}+1}\right)-V_H}{\frac{V_S-V_{OUT}}{R_S}} - B \qquad 2.31$$

Finally, when Equation 2.24 is put into the Equation 2.31, R_T value can be expressed.

$$R_T = \left[\frac{\left(\frac{V_S\left(\frac{B}{R_{CG}}+1\right)-V_H}{\frac{V_S-V_{out}}{R_S}} - B\right)}{\frac{B}{R_{CG}}+1}\right] - R_S \qquad 2.32$$

Where $B = R_{CH} + R_H$.

The thermistor's electrical resistance, R_T, is used to calculate the temperature at thermistor locations. From Eq 2.32 and Eq. 2.1, the temperatures at thermistor locations are calculated.

Moreover, all the resistances in this subsection will be measured in the test setup.

2.3 Finite Element Analysis of Package

Finite element analysis (FEA) of the package is handled with COMSOL Multiphysics. The main purpose of these analyses is to model the system behavior between 5˚C and 35˚C and gain insight before proceeding to the production step.

The oven controlled package is modeled in the SOLIDWORKS environment with its all elements including hybrid package, alumina base, cap package, copper tube, trans-impedance amplifier circuit, and PCB. This 3D model is used for the numerical calculation of Heat Transfer in Solids with a Steady-State Study in COMSOL Multiphysics 5.5.

The sealed package can be considered as a control volume and energy conservation equations used for a singular element in this FEM can be expressed as follows [41]:

$$\dot{E}_{in} + \dot{E}_g - \dot{E}_{out} = \dot{E}_{st} \tag{2.33}$$

where $\dot{E_{in}}$, $\dot{E}_g$, $\dot{E_{out}}$, and $\dot{E_{st}}$ represents thermal energy inflow, rate of thermal energy generation, thermal outflow, and energy storage, respectively.

$$\dot{E}_g = \dot{q}\ dx\ dy\ dz \tag{2.34}$$

Where $\dot{q}$ is the energy generation rate per unit volume.

$$\dot{E}_{st} = \rho\ c_p\ \frac{\partial T}{\partial t} dx\ dy\ dz \tag{2.35}$$

Equation 2.33 can be expressed as:

$$q_x + q_y + q_z + \dot{q}\ dx\ dy\ dz\ -\ q_{x+dx} + q_{y+dy} + q_{z+dz} = \rho c_p \frac{\partial T}{\partial t} dxdydz \tag{2.36}$$

Fourier's law is used to evaluate the heat conduction rates for energy inflow and outflow.

$$q" = -k\nabla T\ = -k(i\frac{\partial T}{\partial x} + j\frac{\partial T}{\partial y} + k\frac{\partial T}{\partial z}) \tag{2.37}$$

The heat diffusion equation for the control volume becomes:

$$\frac{\partial}{\partial x}\left(k\frac{\partial T}{\partial x}\right)+\frac{\partial}{\partial y}\left(k\frac{\partial T}{\partial y}\right)+\frac{\partial}{\partial z}\left(k\frac{\partial T}{\partial z}\right)+\dot{q} = \rho\, c_p\,\frac{\partial T}{\partial t}dx\,dy\,dz \quad 2.38$$

Newton’s law of cooling is constructed for convective heat transfer boundary condition as:

$$q" = h(T_{ext} - T) \quad 2.39$$

where h is the convective heat transfer coefficient, T_{ext} is the environment temperature and T is the temperature of the package surface. In the first simulation, FEA aims to investigate whether the heating elements become a sufficient heat source to keep the system above the ambient temperature. The module used in this analysis is heat transfer in solids and the steady-state study is run.

The assigned materials are kovar for the package, alumina for the two bases, and FR4 for the PCB. Deposited gold and copper are also assigned separately on the alumina bases. Initial values for Heat Transfer in Solids are set to the same temperature as the surrounding environment. The heating elements are defined as the heat source in these thermal studies and a 0.5 W heat rate is assigned to them. Figure 2.17 shows the heating elements selected in the FEM, highlighted in blue. Convective heat flux boundary condition is imposed on the package's outer cage. Because the package's inner cavity is vacuum-sealed, no convection is defined in this space. Figure 2.18 shows the convective heat flux boundary condition. The convective heat transfer coefficient is taken as 10 W/m^{2}K for the first run of these simulations.

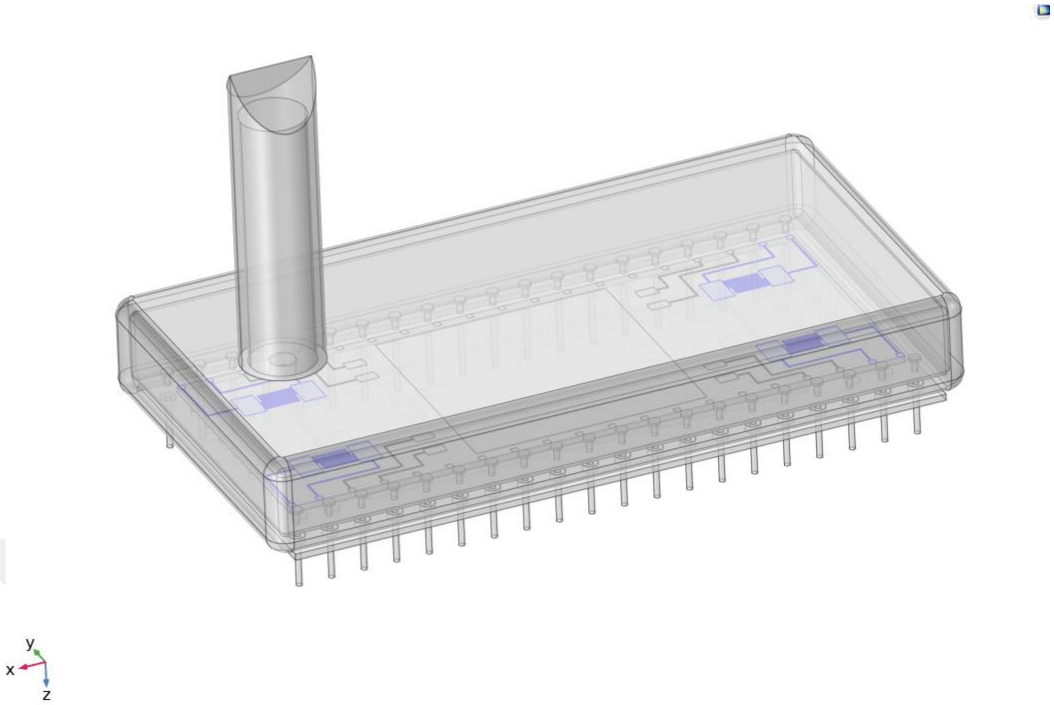

Figure 2.17. Selected heating elements for defining heat source in COMSOL.

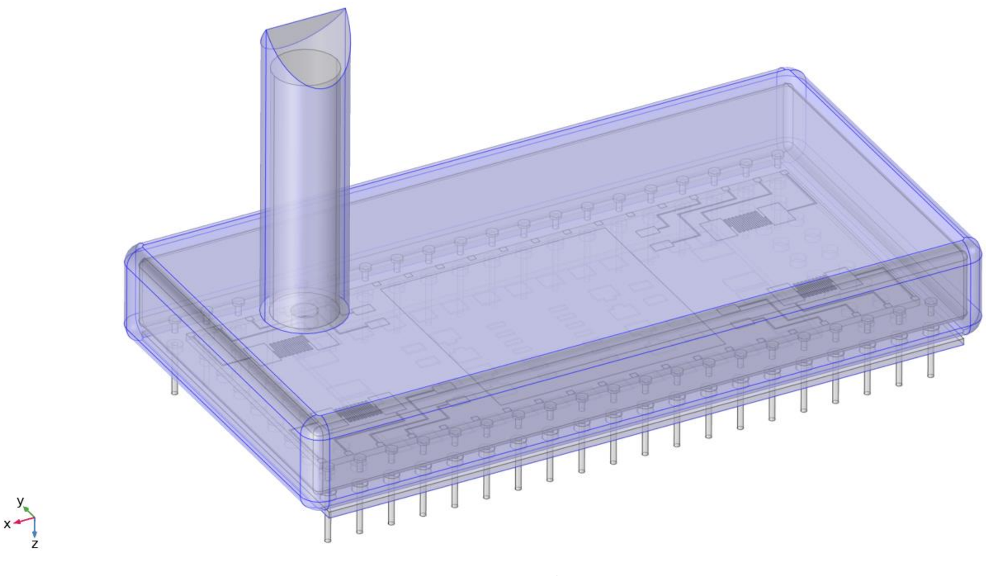

Figure 2.18. Convective heat flux boundary condition.

The size of the mesh is determined by the smallest element size in the geometry. In addition, a simple mesh convergence analysis is performed between extra fine mesh and extremely fine mesh size, and both conclude with the same results. Following those analyses, the extra fine mesh size is selected. This mesh contains 4283785 elements, including both triangular and tetrahedral elements. Figure 2.19 shows the mesh on the geometry. Mesh convergency analysis is presented in Table 2.2 for 25 °C environment temperature. Temperatures of thermistor locations are evaluated in different mesh types until a convergency is achieved.

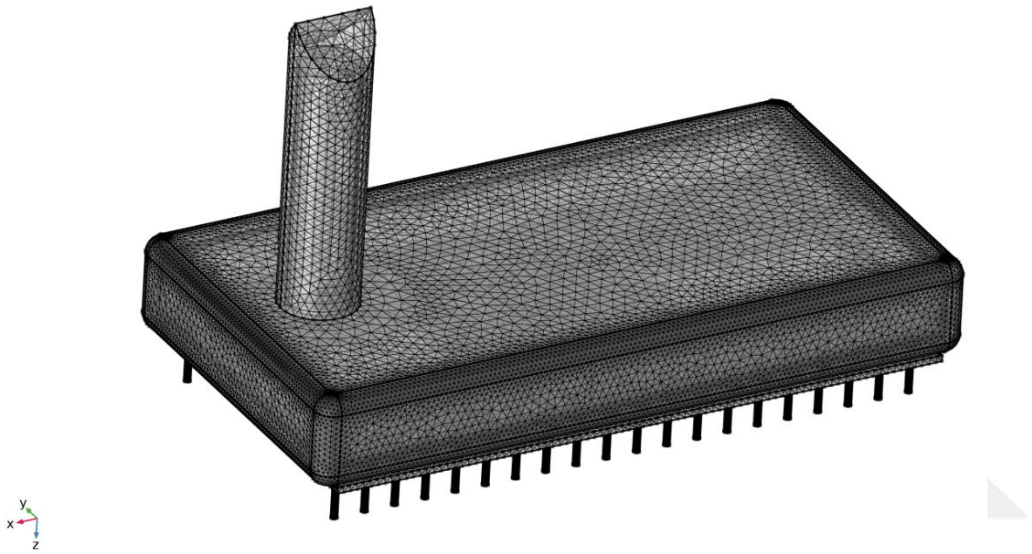

Figure 2.19. Extra fine mesh on the geometry.

Table 2.2. Mesh convergency analysis.

Mesh Size	Element numbers	Temperature results			
		T_{S1}(°C)	T_{S2}(°C)	T_{S3}(°C)	T_{S4}(°C)
Extremely Fine	45789876	72.843	72.865	73.546	73.546
Extra fine	4283785	72.842	72.864	73.546	73.545
Finer	1244698	72.838	72.86	73.543	73.54
Fine	520225	72.834	72.856	73.538	73.536
Coarser	134475	72.823	72.843	73.523	73.719

In the post-processing of the numerical solution, temperature evaluation is made with the Point Evaluation feature of COMSOL on the soldering points of thermistors. The points where temperature evaluation is made can be seen in Figure 2.20.

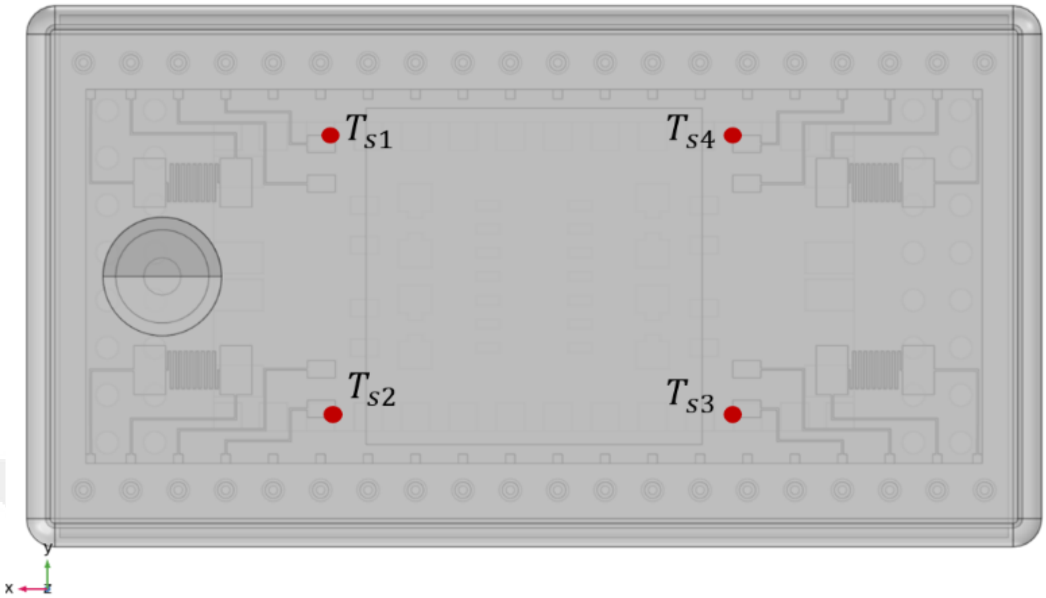

Figure 2.20. Temperature evaluation points.

The steady-state analysis results are presented in Table 2.3 for the conditions between 5 °C and 35 °C external temperature, convective boundary condition, and a total of 2 W power input.

Table 2.3 Temperature at the sensing points at steady state.

T_{ext} (°C)	T_{s1} (°C)	T_{s2} (°C)	T_{s3} (°C)	T_{s4} (°C)
5.00	55.81	55.80	55.79	55.81
10.00	60.80	60.79	60.79	60.80
15.00	65.80	65.78	65.78	65.79
20.00	70.79	70.77	70.77	70.79
25.00	75.78	75.77	75.76	75.78
30.00	80.77	80.76	80.76	80.77
35.00	85.407	85.404	85.404	85.404

At the end of the analysis, it is concluded that 0.5W for each of the thermistors, a total of 2W is enough to keep the system above room temperature at steady-state conditions. For demonstration purposes, the steady state analysis results are only shared for the conditions of the ambient temperature of 20°C and convective heat transfer of 10 W/m^{2}K. Figure 2.21 shows only the temperature distribution of alumina substrate at steady-state conditions. Figure 2.22 shows the temperature distribution of the oven controlled package.

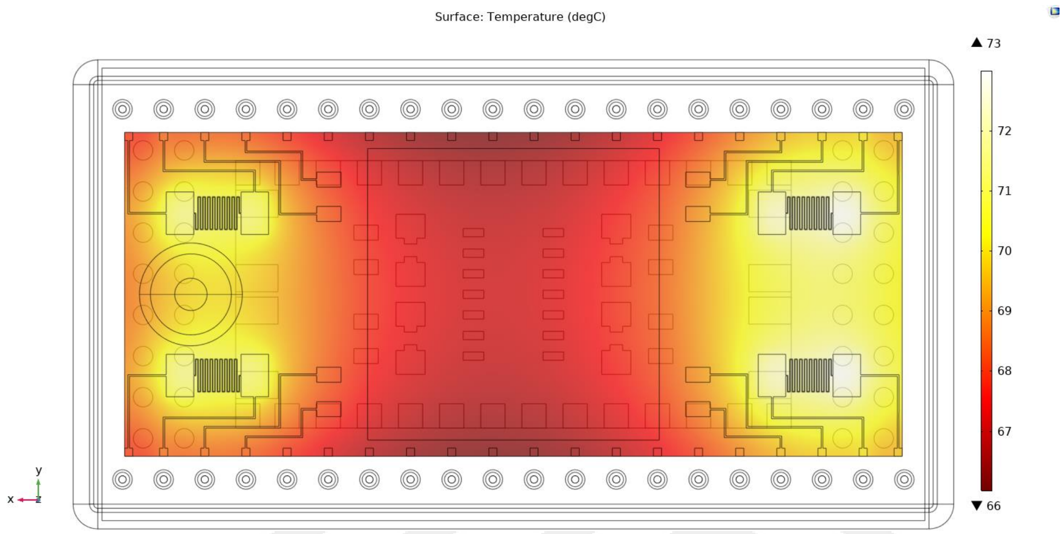

Figure 2.21. Temperature distribution on the alumina surface.

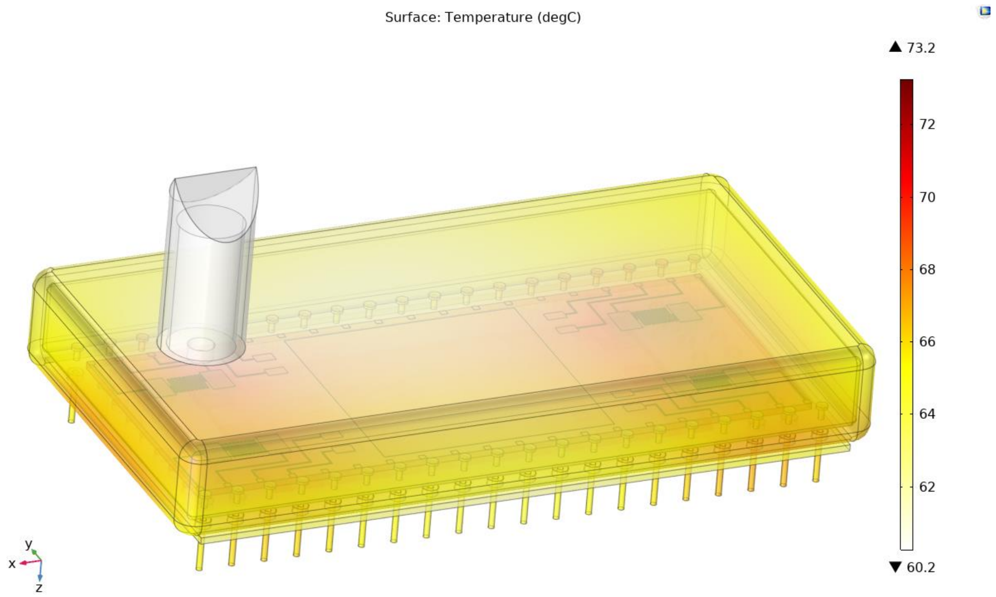

Figure 2.22. Temperature distribution on the oven controlled package.

After, the discrepancies in heat transfer rates on the package's surfaces are analyzed. This investigation provides insight into whether the system can be simplified to a 1D/2D model in the finite element analysis. In the post-processing of this analysis, conduction rates are evaluated with the surface integration evaluation procedure in the COMSOL to compare all surfaces' heat transfer rates. Three main sections are considered, the PCB side of the package, the cap package with copper tube, and the sides of the package. For the total input of 2W, percentages of heat transfer rate are summarized in Table 2.4.

Table 2.4. Distribution of heat transfer rates along the surfaces.

Selected Regions	Percentage
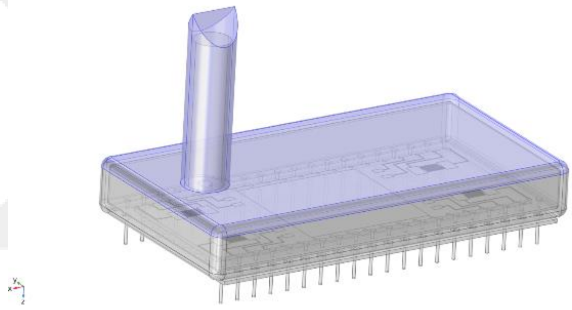	42.25 %
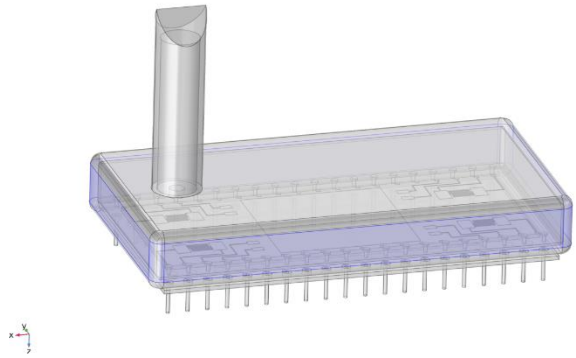	18.56 %

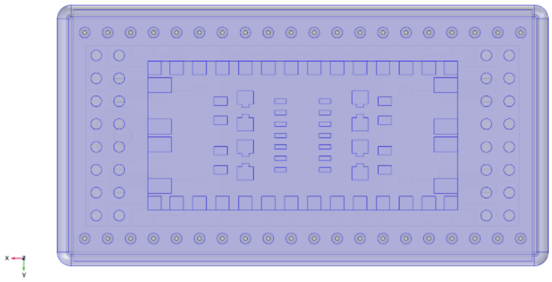	37.75 %

As Table 2.4 shows, all surfaces are significant in terms of heat transfer. Hence, it is decided that no simplification of the geometry can be made to build an analytical and numerical model. Finite element analysis continued with the full model assembly of the system.

Additionally, a parametric study using various convective heat transfer coefficients is done. The objective of this parametric study is to observe changes in the sensing locations' temperature as h varies between 3 W/m^{2}K and 10 W/m^{2}K at different environmental temperatures. Figure 2.23 shows the results of this numerical study. As can be seen from the graph, while the environment temperature is 5 °C and the convective heat transfer coefficient is selected as 10 W/m^{2}K, the temperature of the T_{s1} is calculated as 53.78 °C. On the other hand, at the same temperature with a convective heat transfer coefficient of 3 W/m^{2}K, the temperature of the T_{s1} calculated as 157.6 °C. This analysis demonstrates that the convection heat transfer boundary condition has a significant influence on the thermal behavior of the system. Consequently, the convective heat transfer coefficient, h, must be chosen in consideration of the environmental conditions. As a result, the h value will be selected following the fabrication, assembly, and construction of the test setup procedures. FEA will be updated with the test setup conditions and experimentation, the revised model will be presented in CHAPTER 4. In Figure 2.24, a process flow chart is presented for the aim and strategy with FEM, the details are discussed in CHAPTER 4.

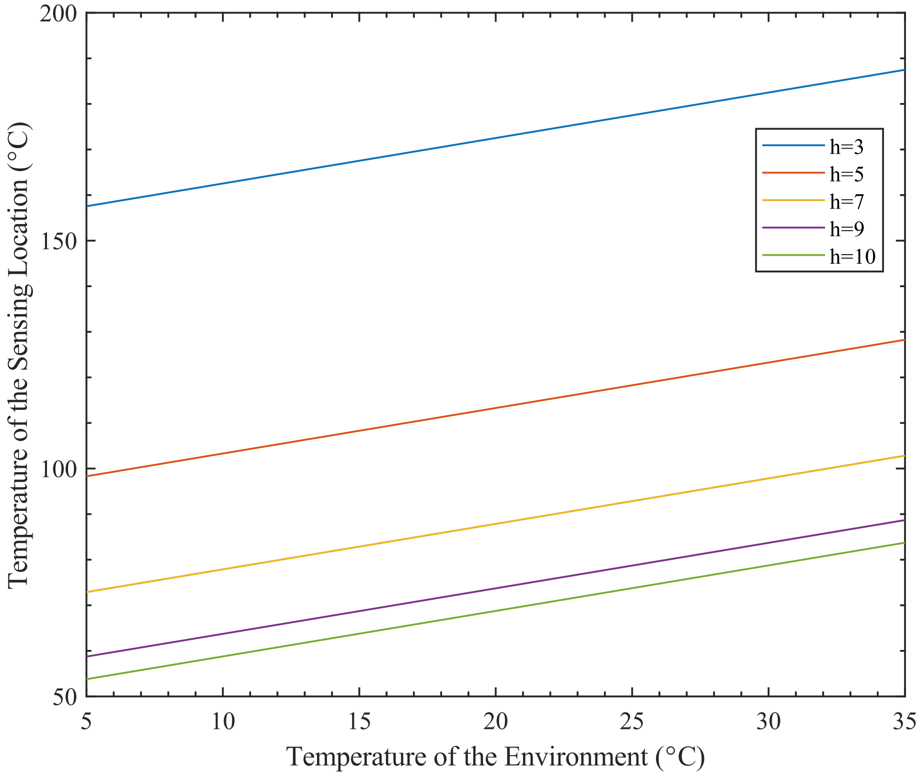

Figure 2.23. Temperature at the T_{S1} with varying convective heat transfer coefficients.

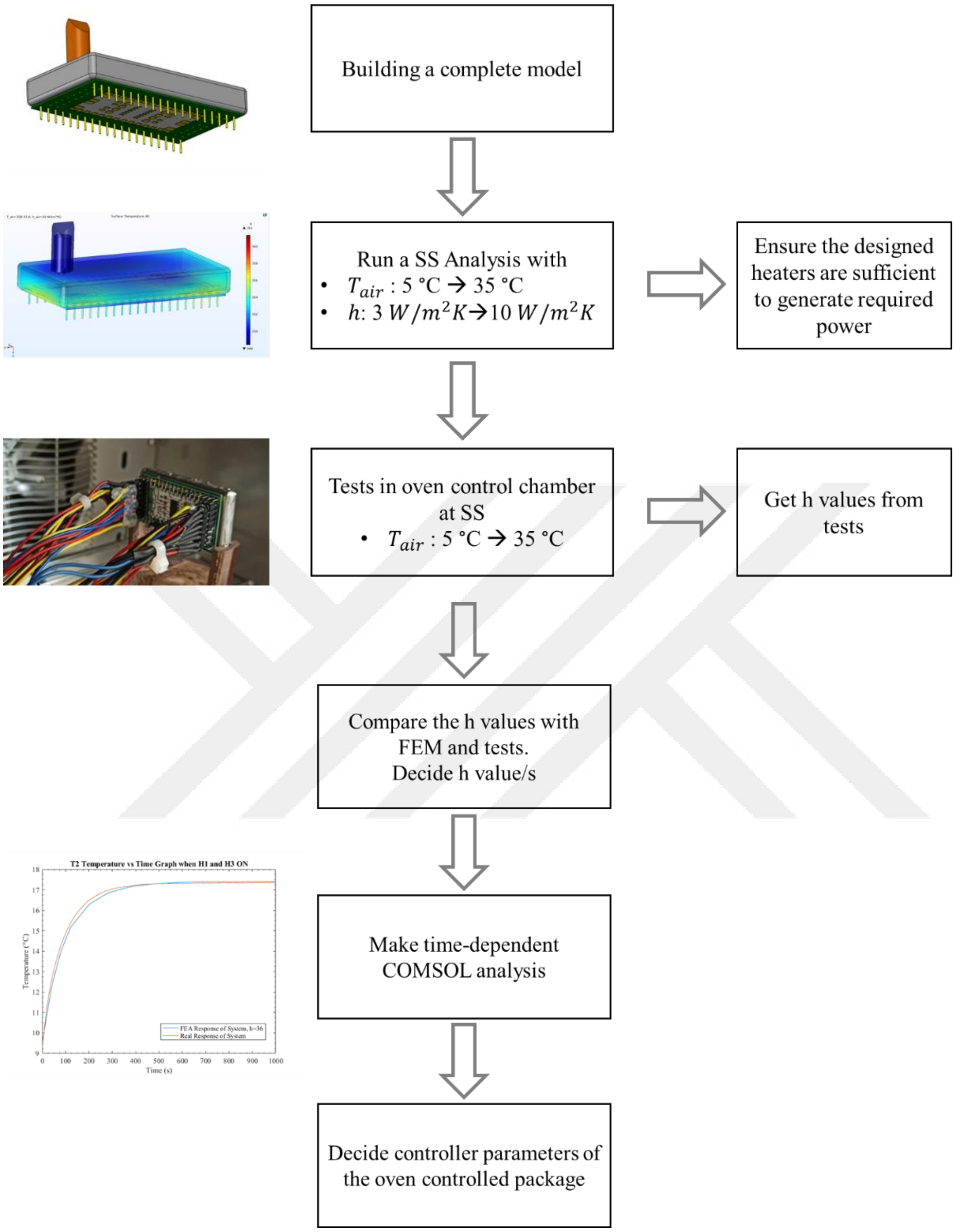

Figure 2.24. A flow chart of the finite element analysis and building a controller from FEA.

2.4 MEMS Sensor

The MEMS sensor located inside the package is a DETF resonator. Its analytical modeling and finite element simulations are presented.

2.4.1 Analytical Model of the DETF Resonators

An analytical model which was developed in [42] is used to comprehend the frequency response of MEMS sensors with changing temperatures. The parameters of the DETF resonator are given in below.

Table 2.5. MEMS DETF resonator device parameters.

Parameters	*Symbol*	Value
Length of DETF tine	L	700 µm
Length of Suspended Beam	L_{sb}	1150 µm
Width of DETF tine	w	10 µm
Width of a connector beam	w_c	880 µm
Gap	g	2 µm
Device thickness	h	35 µm

Material properties used for those calculations can also be given in Table 2.6.

Table 2.6. Material properties.

Parameters	*Symbol*	Value
Density of Si	ρ	2300 kg/m^3
CTE of glass	α_g	3.25x10^{-6} 1/K
CTE of silicon	α_{Si}	2.59x10^{-6} 1/K
Young's modulus of silicon	E	169 GPa
Young's modulus of glass	E_g	47 GPa

After building stress-strain relations between the silicon substrate and glass cap, the natural frequency of the long DETF resonator can be evaluated. The method for this calculation was discussed in [42]. The natural frequency is calculated to be 170.75 kHz using this method and parameters.

2.4.2 Finite Element Model (FEM) Analysis of DETF Resonators

The frequency response of the MEMS sensor is analyzed with the COMSOL Multiphysics environment. Analytical calculations are validated with simulations.

2.4.2.1 Modal Analysis of DETF Resonators

Modal analysis is performed to calculate the eigenfrequencies of the DETF resonator. In the COMSOL environment, the static structural study is constructed. Anchor points of the resonator are selected as fixed regions. Mesh size is decided by performing a mesh convergence analysis and the finer mesh is built for modal analysis. The first 12 modes of the DETF are investigated. Only in-plane and out-of-plane modes of the long DETF are presented in Figure 2.25.

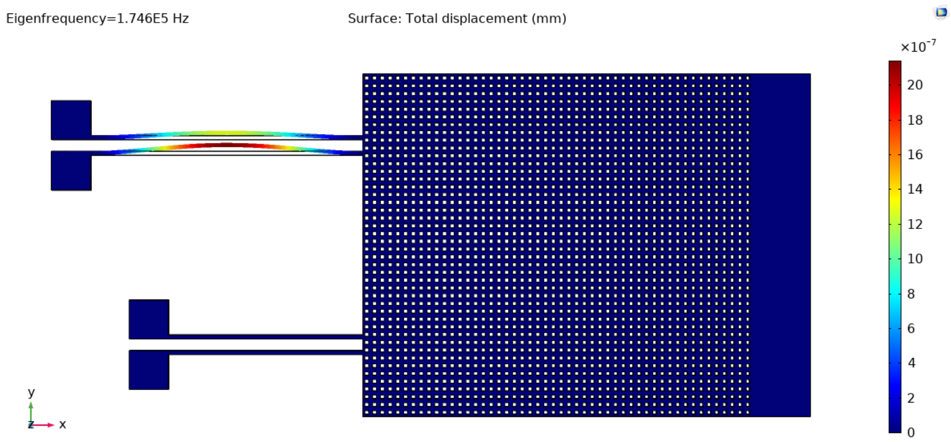

(a)

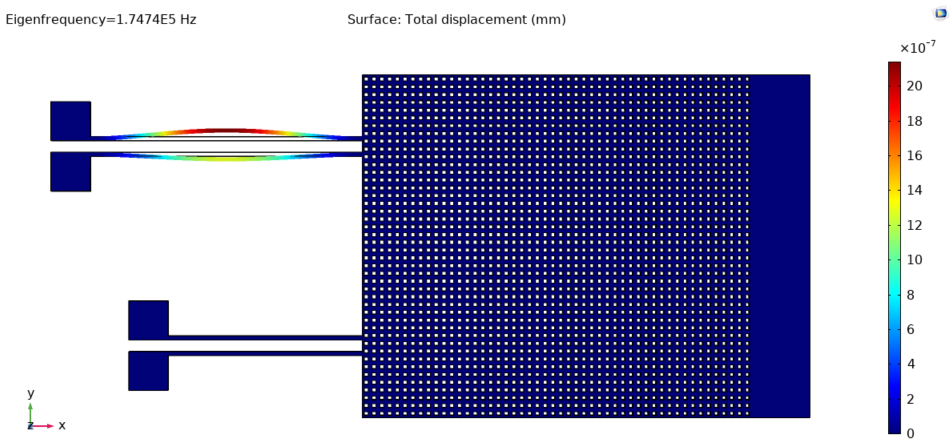

(b)

Figure 2.25. Modal analysis of a) long DETF for in-plane mode, b) long DETF for out-of-plane mode, Thermal Analysis of DETF Resonators.

The reason for only presenting the natural frequency and modes for long DETF resonator results is that they will be used in the characterization tests in the subsequent chapters.

2.5 Summary

In this chapter, a temperature compensation approach is introduced with an oven controlled package. Thermal model is discussed both analytically and numerically. The MEMS sensor used in the package is presented with its mode shape and natural frequencies.

CHAPTER 3

IMPLEMENTATION OF THE OVEN CONTROLLED SYSTEM

In this chapter, the fabrication of the alumina base, alumina TIA, implementation of all the parts, and vacuum packaging procedures are presented. Assembly of the package is introduced in detail.

3.1 Fabrication of Alumina Base and Alumina TIA

Fabrication of alumina base and alumina TIA relies on one masking layer for metallization. However, different approaches are used when patterning metal layers. Hence, fabrication will be presented in two different parts.

3.1.1 Fabrication of Alumina Base

To create a temperature control surface, an alumina wafer is used and processed. The production steps to be performed are shown for each step below.

Step 1: The first step of the fabrication of the alumina base is metallization. The alumina surface must be covered with metal before thermistors and heaters can be placed on it to provide temperature control. As a result, the alumina wafer is coated with TiW and Au during the first stage of production with sputtering. TiW is used as an adhesion layer for metallization. Au is used to transmit signals. Metallization thicknesses are 50 nm for TiW and 400 nm for Au.

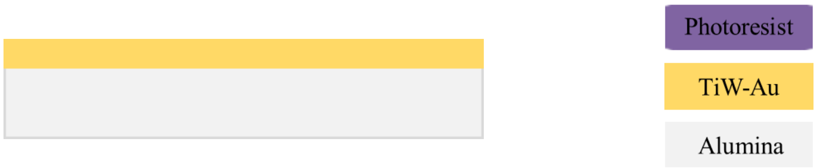

Figure 3.1. Metallization of alumina wafers

Step 2: After completing step 1, the photoresist material is coated onto the alumina wafer as a mask layer to shape the metal lines. The coated material is then exposed to UV light to obtain the desired pattern. Subsequently, the light-exposed areas of the photoresist material are removed from the wafer using a chemical called "developer" through a chemical reaction. In this step, SPR 220-7 is used as the photoresist material, while MF-24A is used as the developer. A coating speed of 3000 rpm has been selected.

Figure 3.2. Lithography of the alumina wafers.

Step 3: In this step, TiW and Au will be shaped by chemical etchants.

Figure 3.3. TiW/Au is patterned in this step.

Figure 3.4 shows the alumina wafer at the end of this step.

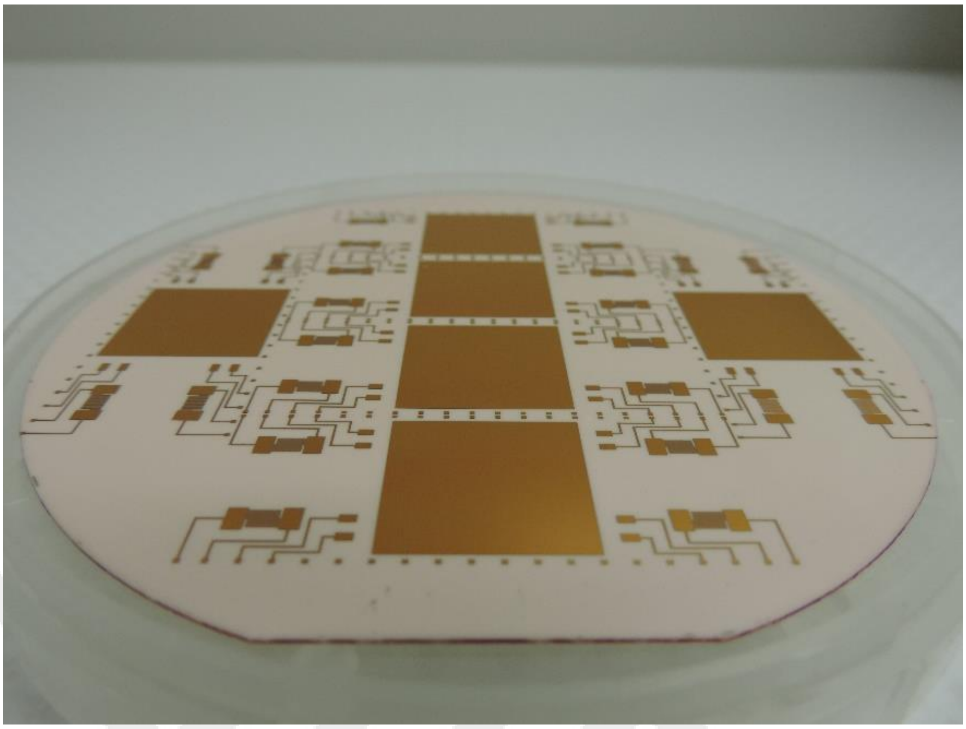

Figure 3.4. An alumina wafer after the metallization process is complete.

Microscope views of metal pads are presented in Figure 3.5.

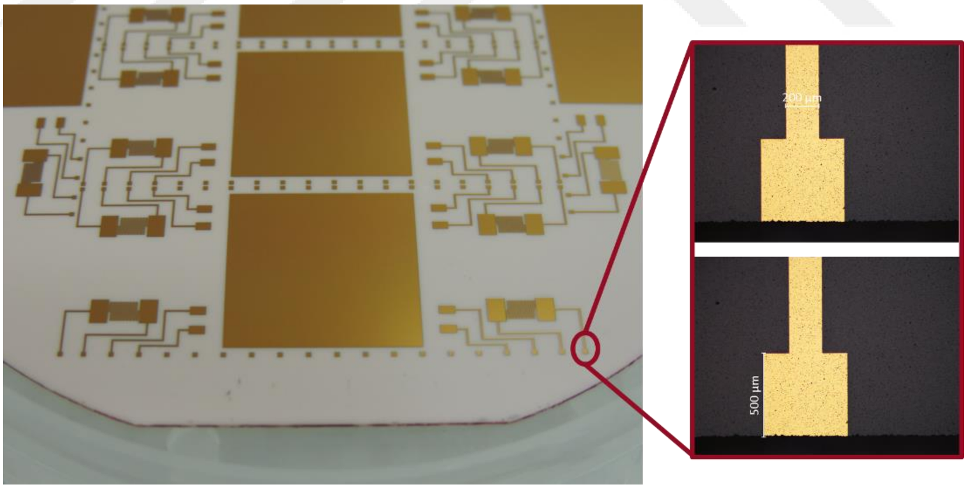

Figure 3.5. Close-up view of alumina substrate and microscope view of metal pads.

Moreover, at the end of the metallization process, a microscope image of the heating elements is given in Figure 3.6.

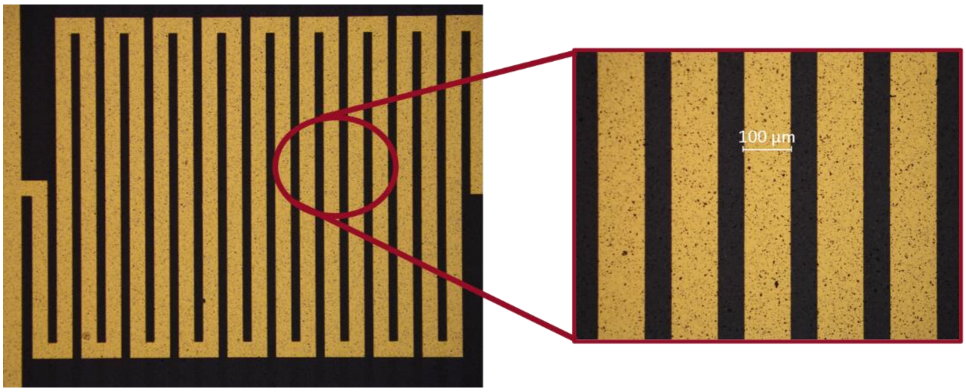

Figure 3.6. Microscope view of heating elements.

Step 4: After completing the signal lines' pattern, TiW/Cu is deposited on the other surface of the alumina wafer with the sputtering method. The second metallization step in this process flow is used to create a bonding surface for the assembly procedure. 2 µm Cu is deposited on top of the 150 nm TiW by a sputtering method.

Figure 3.7. TiW/Cu deposited alumina wafer.

Step 5: After shaping the metal lines and depositing the copper layer, the alumina wafer is transferred to the dicing process to obtain sample dies. To keep the metal lines as clean as possible, the photoresist on the wafer is not removed when the wafer is sent to the dicing step. At this point, issues with the deposited Cu surface have been encountered. The deposited Cu is peeled off. A sub-title summarizes the steps taken to solve this problem.

Step 6: Finally, acetone and isopropanol are used to clean samples from the dicing step.

3.1.1.1 Metal Deposition Optimization

During the fabrication procedure, problems were encountered between Step 4 and Step 5, primarily involving the peeling off of the metal layer from the edge of the alumina die. This problem can be seen in Figure 3.8.

Figure 3.8. Peeled off metal layer.

This issue could potentially be attributed to intrinsic, thermal, or mechanical stresses. Intrinsic stresses may arise during the metal sputtering process and are independent of the thermal stresses that occur at deposition temperature. These intrinsic stresses could be correlated with factors such as grain growth, defect annihilation, and solvent evaporation [43]. Thermal stresses may arise due to mismatched coefficients of thermal expansion (CTE) between the substrate and the film material. Additionally, mechanical stress could be introduced by the dicing blade used in the fabrication process.

The issue may be attributed to two critical steps in the process flow. The first step involves the manipulation of sputtering parameters, while the second step pertains to dicing. Delamination of TiW could arise in the metal sputtering step due to residual stress or inadequate adhesion. Similarly, peel-offs may be caused by crack propagation induced by the dicing blade.

To address the issue, a series of experiments were conducted. The initial trial focused on enhancing the adhesion of the TiW-Cu layer, incorporating procedures outlined in the reference [44]. The surface pre-treatment involved a sequence of steps, starting with solvent cleaning using acetone and IPA. Subsequently, plasma treatment was conducted in the sputtering chamber using Ar atoms to create a cleaner surface. Following the pre-treatment, TiW-Cu sputtering was performed without breaking the vacuum environment. Finally, the metal-deposited alumina wafers were subjected to annealing at 250°C. However, despite these efforts, delamination of the metal film was still observed after the dicing step.

Another trial was undertaken to optimize the dicing procedure to reduce mechanical stress. In this approach, a blind cut was made to create grooves in the wafer, rather than cutting from top to bottom. The wafer was then manually broken along these grooves to obtain completely separated dies. While some dies were obtained without any delamination, a few still exhibited peel-offs. As a result, the optimization process was continued to further refine the procedure.

The last trial was conducted for decreasing the thermal stress in the deposition process. Sputtering 2 µm of Cu results in a temperature increase in the wafer. Hence, deposition parameters including temperature, time, and power are optimized in the METU MEMS Center, and the best results were obtained from that.

One of the dies that had no evidence of delamination is shown in Figure 3.8.

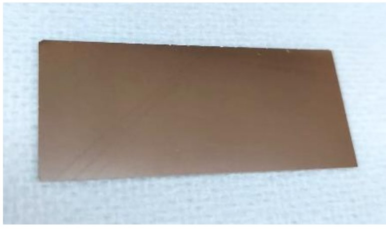

Figure 3.9. Cu deposited side of the alumina substrate

3.1.2 Fabrication of Alumina TIA

The circuit was designed to integrate the thermistor circuit within the package and amplify the sensor signal. Alumina, a material chosen for its minimal differences in thermal properties within the package, was utilized in the design. The fabrication of the Transimpedance Amplifier (TIA) circuit is elucidated below with accompanying schematics.

Step 1 The lift-off procedure was employed to create the metal lines in the circuit. Photolithography served as the initial step in the fabrication process. The photoresist of choice was AZ nLOF 2070, specifically selected due to the desired thickness of the copper layer. Subsequently, a 1 µm Cu layer was deposited, for which AZ nLOF 2070, with a thickness of 7 µm, was selected.

Step 2: After patterning the photoresist, TiW/Cu layer is deposited. TiW is used as an adhesion layer for copper deposition.

Step 3: The alumina wafer undergoes the acetone bath to finish the metallization. Peeled metals are visible in Figure 3.10, which shows the lift-off procedure.

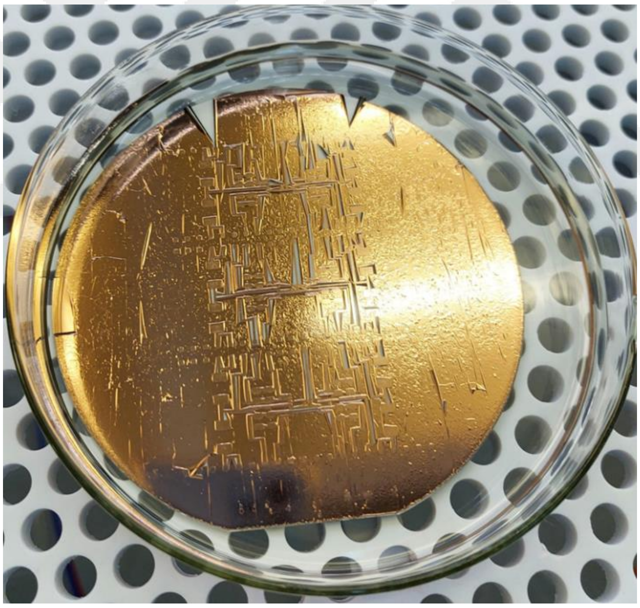

Figure 3.10. Lift-off procedure carried out for TIA circuit.

Step 4: Dicing procedure is applied for the alumina wafer to prepare the system to assemble. To confirm that all signal lines are functioning, a short circuit test is carried out in the probe station following the dicing step, which is shown in Figure 3.11.

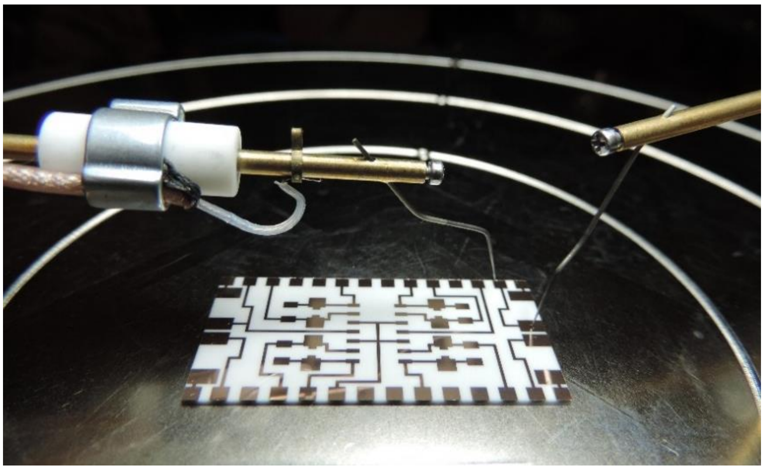

Figure 3.11. TIA circuit after dicing procedure.

3.2 Assembly Procedure of the Package

The complete assembly of the oven-controlled package comprises two Hybrid Packages, an alumina substrate for temperature control, four thermistors, a MEMS sensor, an alumina-based Transimpedance Amplifier (TIA) circuit, a PCB board, and a copper tube. Each assembly step will be elaborated upon systematically.

Step 1: Firstly, the edges of the package are chamfered to create a groove in the interface of solder. After this operation, the Hybrid package should be cleaned of all organic contaminants to have a reliable soldering interface. Aceton and isopropyl alcohol are used for this purpose.

Step 2: First soldering process is done to the edges of the package. Pins of the hybrid package should be protected at this stage. Hence, a tool is designed in the METU MEMS Center and used for enclosing the pins of the package. To easily locate the package, the package's legs are inserted into grooves in another designed apparatus. After this, the package is positioned on the hot plate surface which is set to 100°C. The package's edges are covered in solder paste, and solder wire is used to wet all the edges. Figure 3.12 represents this process in its finished state. This procedure also applies to the cap package for vacuum packaging purposes. Afterwards, the package is cleaned once more.

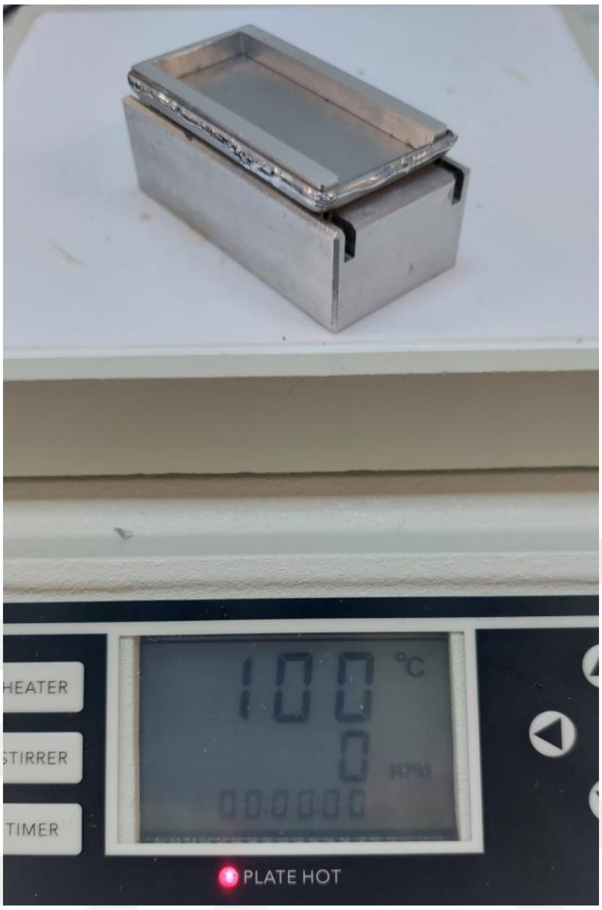

Figure 3.12. The complete soldering operation for edges.

Step 3: In this step, solder was applied to the assembly surface of the package and the alumina substrate, following the configuration established in the previous step. The surface temperature was maintained at 300°C. Additionally, the pin-protecting tool served as an alignment aid during this process, as the soldering operation was performed within the gap provided by the tool. Figure 3.13 illustrates the different stages of soldering for two cases: one where the solder is still wet, and the other where it has solidified and been cleaned with alcohol.

(a) (b)

Figure 3.13. Soldering operation for assembly surface between package and alumina substrate. (a) Solder is still wet. (b) Solder is solidified and cleaned.

Step 4: Alumina substrate’s backside should be soldered for the attachment of the substrate to the package surface. This operation is carried out on the hot plate which is set to 200°C.

Step 5: Four thermistors are soldered on their pads. The alumina substrate is cleaned once more.

Step 6: The cleaned package is placed on the hot plate, and the temperature is set to 330°C. It is needed to wait until the solder is completely reflowed on the die attachment region. Afterwards, the alumina substrate can be put on the surface of reflowed solder with the guidance of the alignment tool. A tweezer is used to apply pressure on the alumina substrate. To facilitate the solidification of the solder attachment, the hot plate temperature is adjusted to 20°C. As a result, both the package and the substrate are gradually cooled down using the hot plate.

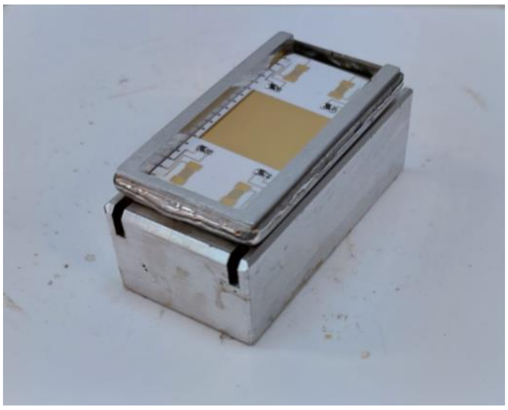

Figure 3.14. Die attachment procedure.

Step 7: Attachment of the MEMS sensor to the alumina substrate is carried out with silver epoxy, EPO-TEK H20E.

Step 8: Wire bonding is utilized in this step to create the connection with the package's interior.

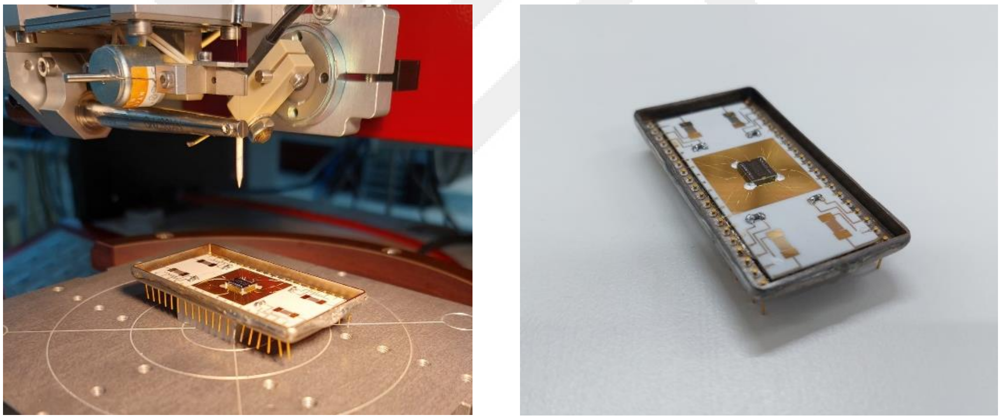

(a) (b)

Figure 3.15. Wire bonding operation

Step 9: The copper tube is attached to the cap package by soldering.

Step 10: Packages are sealed using a soldering iron.

Step 11: Vacuuming is performed on sealed packages using the copper tube. Details will be given in the upcoming subsection.

3.2.1 Vacuum Packaging Method

The MEMS sensor, which is bonded on top of the alumina surface, is designed to operate in vacuum conditions. This is because there is a significant difference between a sensor operating in an atmospheric environment compared to one operating in a vacuum environment. When operating in atmospheric conditions, the sensor interacts with gases, which act as energy absorbers, leading to gas damping losses. Therefore, to minimize the impact of gas damping losses on the sensor's performance, it is essential to place the sensor in a vacuum environment. This is particularly important for the resonator's quality factor, which can be influenced by various factors.

Once the assembly is ready for vacuum packaging, it is connected to a turbomolecular pump, as depicted in Figure 3.16, to initiate the vacuum packaging process. As the vacuum level reaches around 10^{-6} Torr, the copper pipe is cut, and the package is then evacuated to achieve the desired vacuum level.

Figure 3.16. Vacuum packaging procedure.

Pinch-off method is used for cutting the copper tube. The tool for utilizing this operation was developed in METU MEMS Center. The vacuum packaged assembly is given in Figure 3.17.

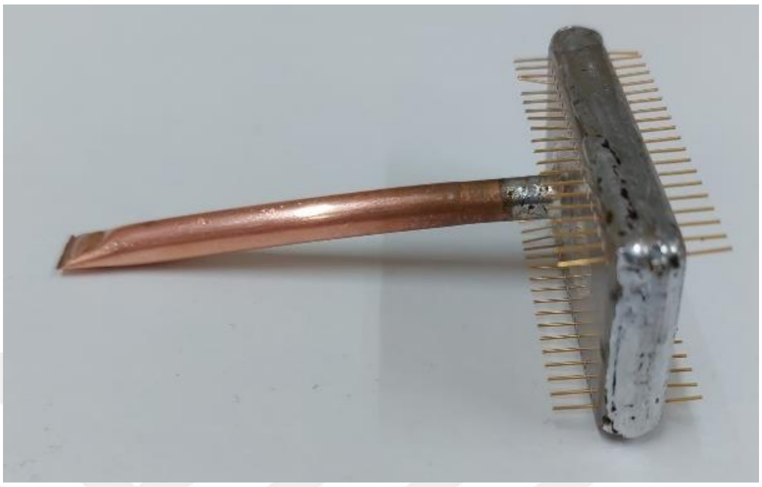

Figure 3.17. Vacuum sealed package.

More than one trial was made for the vacuum packaging procedure. To understand the sealing performance and test the pinch-off method, the Helium (He) leak test is performed in those trials. He leak tests are carried out in accordance with MIL-STD-883E standards. The first step is placing the package in a sealed chamber, pressurizing it with helium, and depressurizing it several times. Afterwards, the package should wait under helium with a pressure of 45 psia (approximately 3.06 atm) for a minimum of 10 hours. According to the applicable standard, the package's volume defines the test's required time and pressure value. After releasing the pressure in this chamber, the package is transferred to the He leak detector. The He leak detector will be utilized to extract any He gas that may have been introduced into the package previously. The Reject limit is defined as $5.0*10^{-8}$ atm cc/s He in the relevant standard. VIC MS-40 model is used for He leak detection; the test configuration is given in Figure 3.18. The leak measurement range of this detector is between 10^{-3} and 10^{-11} atm cc/s. After the tests, no instances of leakage were detected in the sealed packages. Subsequently, after a period of six months, the test was repeated, and no additional leakage was observed.

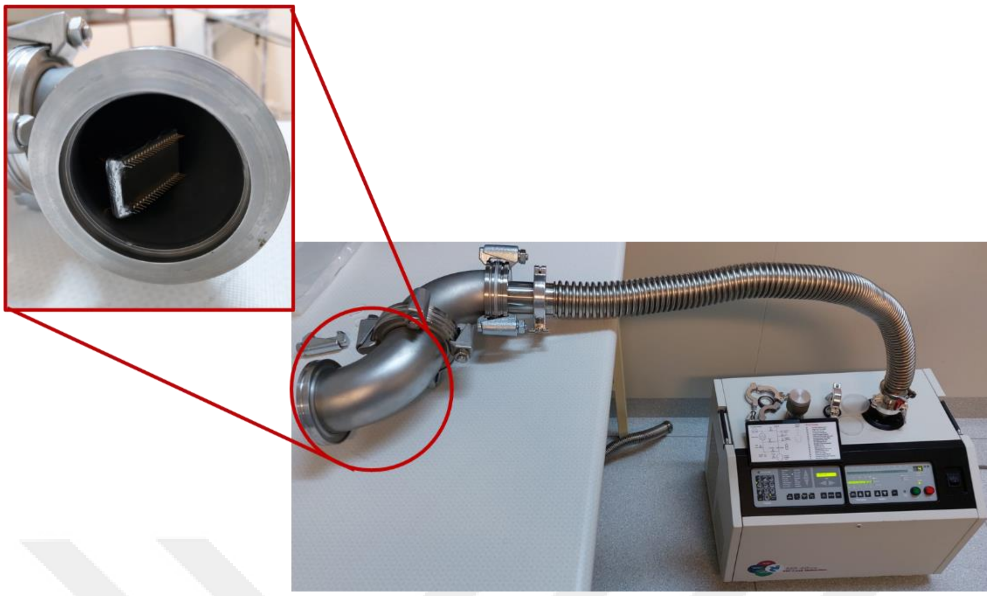

Figure 3.18. Helium leak test setup.

Step 12: Alumina based TIA circuit and PCB board is soldered. Figure 3.19 shows the alumina TIA circuit, PCB, headers, high precision resistors for the thermistor circuit, AD8608 operational amplifier, and resistors for the TIA circuit.

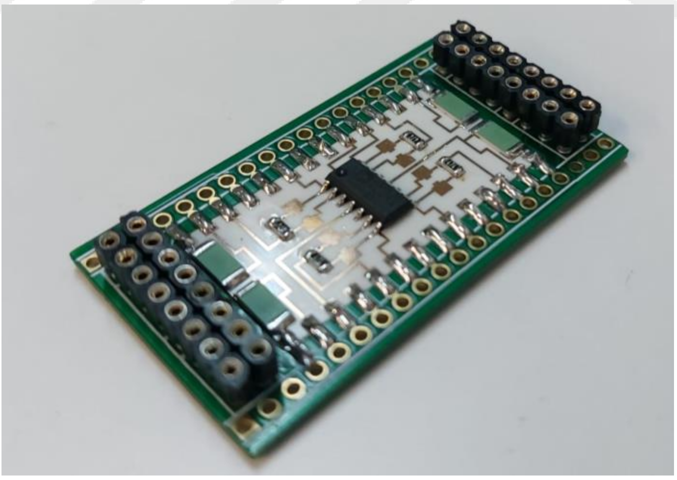

Figure 3.19. Completed soldering process of alumina TIA circuit and PCB with surface mount elements.

Following this soldering operation, a thermal pad was placed on the backside of the alumina circuit to improve heat transfer between the package and the trans-impedance amplifier circuit. Figure 3.20 shows the location of the thermal pad.

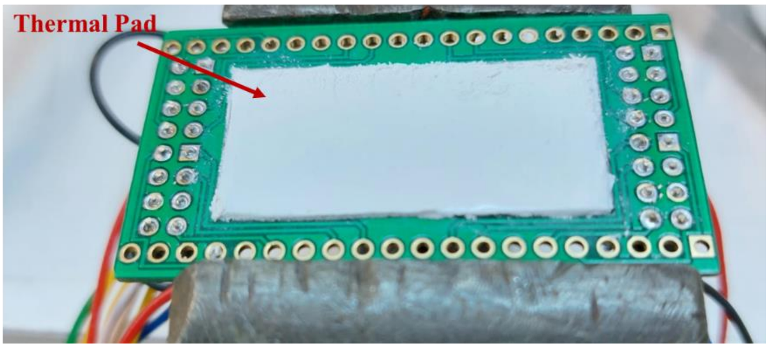

Figure 3.20. Location of the thermal pad on the backside of alumina TIA circuit.

Step 13: The oven controlled package is soldered with a PCB-TIA interface. This is the last step of the procedure. Figure 3.21 represents the completed oven controlled package.

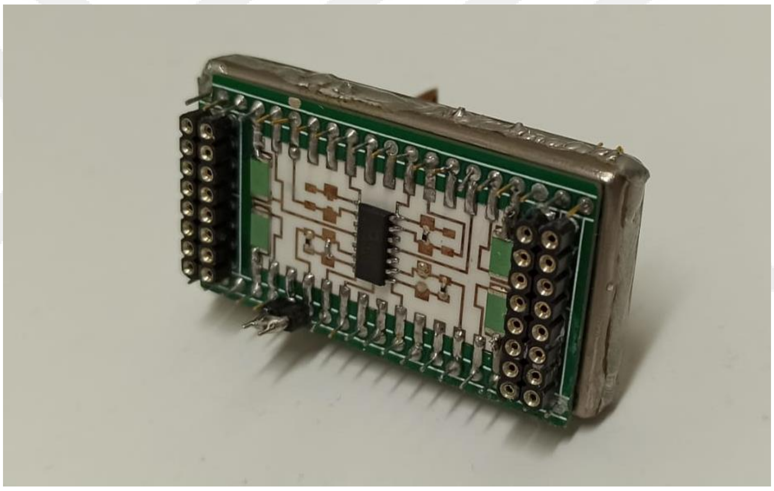

Figure 3.21. Completed assembly of the oven controlled package.

3.3 Summary

In this chapter, the fabrication of the alumina base and alumina TIA circuit is described and supported with microscope views and photographs. The detailed process flow of implementing all the elements and constructing the assembly is presented. Military standard test method of the sealing operation is explained.

CHAPTER 4

CHARACTERIZATION AND CONTROLLER DESIGN

In this chapter, the characterization of the oven controlled package is analyzed with thermal and electrical models of mathematical model and Finite Element Models. A closed-loop controller is implemented in the system. The MEMS sensor is characterized with and without using a closed-loop controller.

4.1 Test Setup

The Oven controlled package's tests are conducted in a climate chamber. As a climate chamber, Espec SH-662 is used. Computer controlled power supplies (Agilent E3631A) are selected for the voltage supply of heaters in the oven controlled package. Between the computer and power supplies, a daisy-chained GPIB connection is built, and voltage commands to the power supplies are sent by the MATLAB environment. NI-6218 Data Acquisition Board is used for temperature measurement from thermistors, and it is processed in the MATLAB interface. Scripts for reading the temperature of the package and sending the voltage input to the heaters are given in Appendix. One power supply is used for the voltage input of thermistors. The read-out circuitry of the MEMS sensor is built on the breadboard. One power supply is also allocated for providing input voltage to the proof mass of the DETF resonator and modulator of the read-out circuit. A waveform generator is used for the modulation signal in the self resonance loop. Finally, an oscilloscope is used for observing the input signal, the output signal of the modulator, and the phase of the resonator. The circuitry is explained in Section 4.6. Table 4.1 presents the list of instruments used in this system-level test setup.

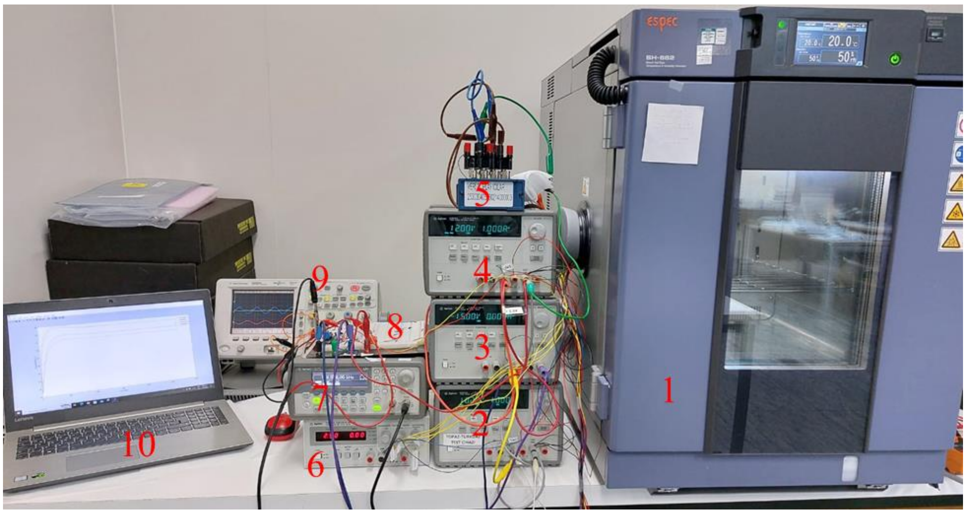

Figure 4.1. Test setup

Table 4.1. Instruments list and their functions in the test setup.

Instrument Number	**Function**
1	Climate chamber
2	Power supply for Heater 1 (H1) control
3	Power supply for AD630 Modulator/Demodulator & Proof mass voltage
4	Power supply for Heater 3 (H3) control
5	Data Acquisition NI6218
6	Power Supply for Thermistors (Vs) & AD8608 Op-Amp
7	Waveform Generator
8	Breadboard, Read-Out Circuitry
9	Oscilloscope
10	PC

4.2 Tests and Measurements of Thermistors and The Oven Controlled Package

Tests and measurements of the oven controlled package were realized in the climate chamber Espec SH-662, which was stabilized under steady-state temperature and humidity parameters. A tool is used to suspend the oven controlled package in the chamber environment. Figure 4.2 shows the location and placement of the package.

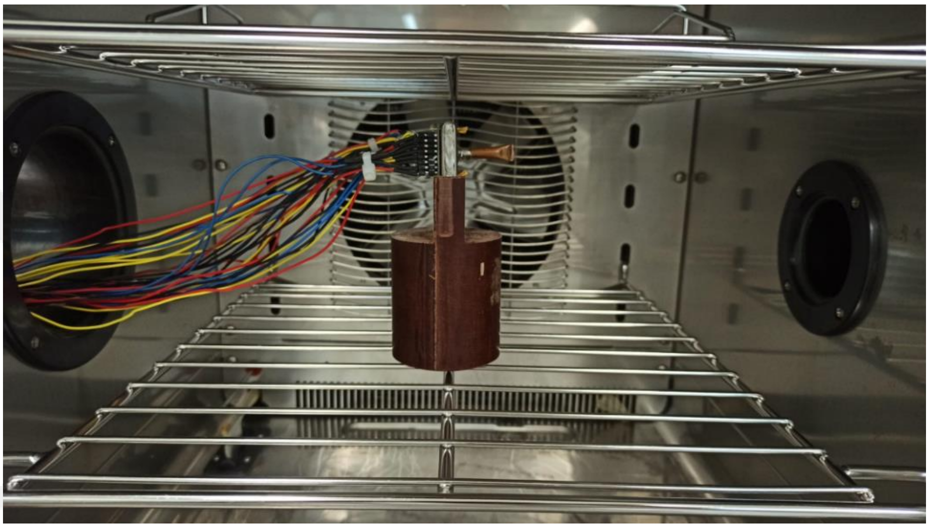

(a)

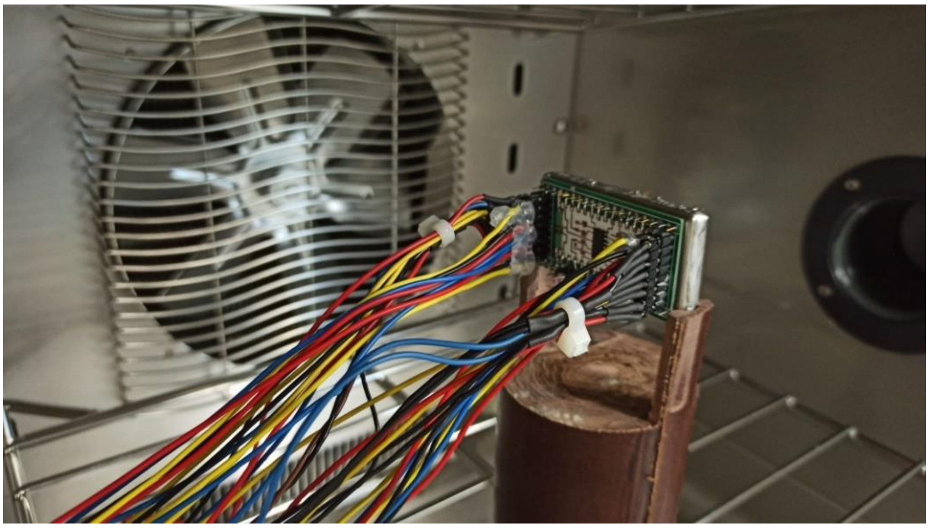

(b)

Figure 4.2. Oven controlled package's placement in the climate chamber. (a) Front view, (b) Side view.

4.2.1 Characterization of Thermistors

To have a consistent methodology in measurements, thermistors were characterized before initiating the tests. The behavior of the four thermistors should be investigated, and their responses should be modeled under steady-state conditions in a climate chamber. It is important for understanding the resolution of the thermistors with the NI-6218 data acquisition board. For that purpose, the climate chamber is stabilized at 25 °C and 10 °C. Figure 4.3 shows the voltage output of the thermistors while the climate chamber was stabilizing to 25 °C. The different voltage levels in Thermistor 1 are most likely the result of soldering and wire bonding operations. The characterization test seen in Figure 4.3 is also repeated at 10 °C, and the outputs are recorded accordingly. Table 4.2 presents the voltage outputs that were collected under different stabilization conditions.

Table 4.2. Steady-state voltage outputs of thermistors.

Temperature	Voltage (V)			
	Thermistor 1	Thermistor 2	Thermistor 3	Thermistor 4
10 °C	1.3714 V	1.3654 V	1.3639 V	1.3646 V
25 °C	1.0175 V	1.0143 V	1.0138 V	1.013 V

The scale factor of these thermistors can be calculated using these measurement values and it is presented in Table 4.3.

Table 4.3. Scale factors of the thermistors.

Thermistor 1	Thermistor 2	Thermistor 3	Thermistor 4
23.59 mV/°C	23.41 mV/°C	23.34 mV/°C	23.44 mV/°C

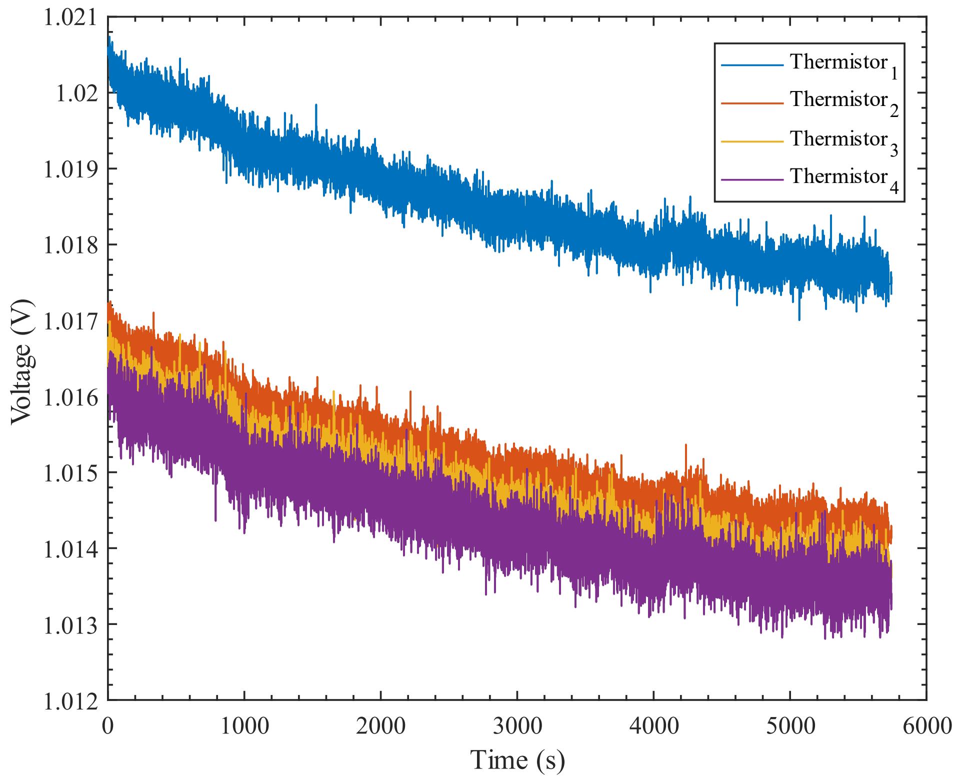

Figure 4.3. The voltage output of four thermistors while the climate chamber is stabilizing under 25°C.

The data acquisition board (NI-6218) used in these readings has 16 bits resolution, which means 65536 steps, and the input voltage of thermistors is 2V. Hence, the smallest change in voltage that we can detect is 0.03 mV, as calculated in Equation 4.1.

$$V = \frac{2V}{65536} = 0.03\ mV \qquad 4.1$$

The minimum detectable temperature change in the system can be calculated with the scale factor of thermistors and the resolution of DAQ. It is 0.013°C for all the thermistors.

4.2.2 Steady-State Test Results of the Oven Controlled Package

In the climate chamber, two different steady-state temperatures were utilized for initial tests. One is 10 °C, and the other is 25 °C. The primary objective of these tests is to obtain the system's thermal properties for analytical and numerical modeling. Obtaining the thermal properties of the system is required to construct a closed loop controller system for the oven controlled package.

In the steady-state tests, a step response experiment was carried out. After the stabilization of the climate chamber was completed, a voltage input of 1 volt was given to one of the heating elements in the oven controlled package. A step response of four thermistors is observed. When all the thermistors reached the steady-state temperature point, the voltage input to the heating element was turned off. The four thermistors were observed to reach their steady-state points again. After reaching the climate chamber's steady-state conditions, the experiment was carried out with 2V and 3V voltage inputs to the same heating element. The experiment was then repeated using the other three heaters with the same voltage inputs, and the step responses of all thermistors were recorded in all those experiments. A total of 24 experiments were carried out at 10 °C and 25°C; four different sets of experimental data are shared in the table below for a voltage input of 1 volt and a temperature of 25 °C.

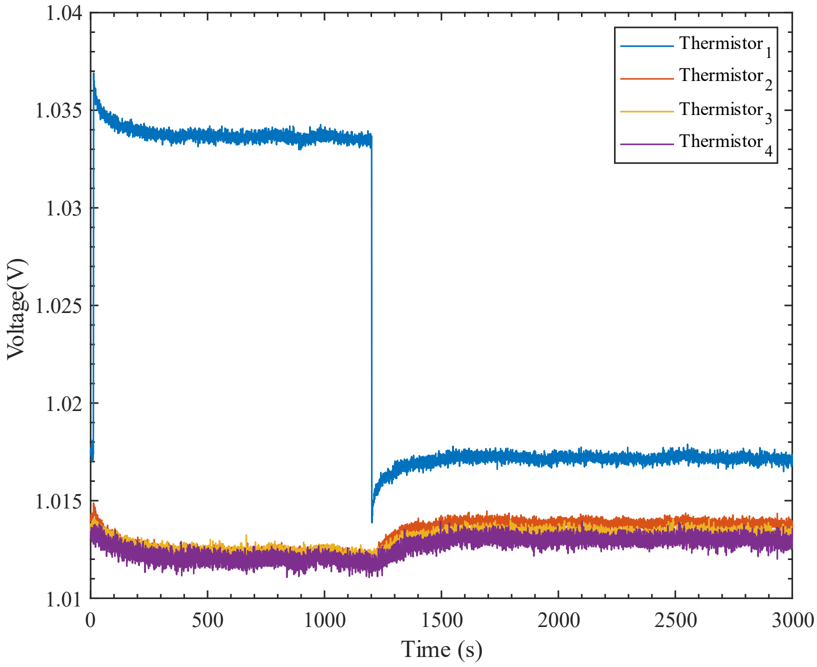
1.04
1.035
1.03
1.025
1.02
1.015
1.01
Voltage(V)
0
500
1000
1500
2000
2500
3000
Time (s)
Thermistor 1
Thermistor 2
Thermistor 3
Thermistor 4

(a)

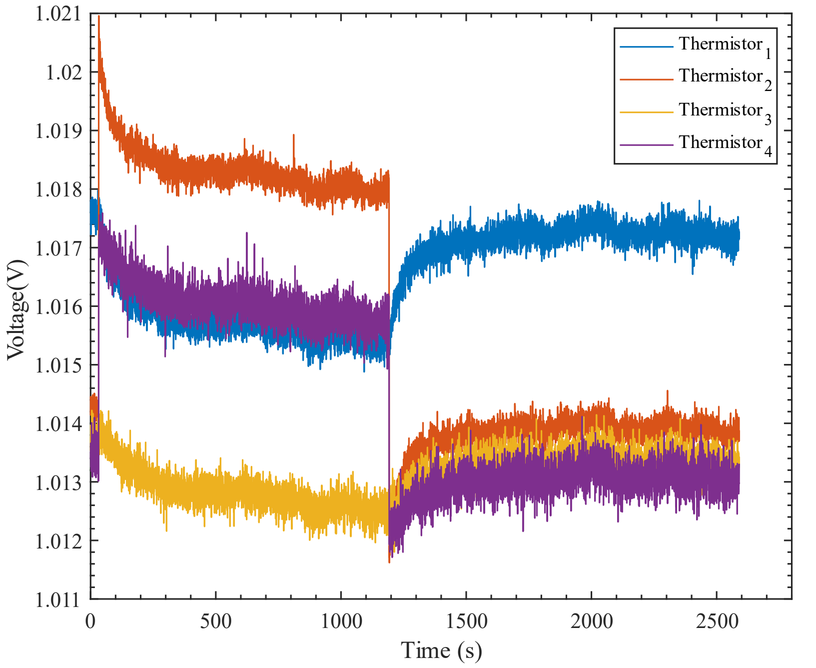
1.021
1.02
1.019
1.018
1.017
1.016
1.015
1.014
1.013
1.012
1.011
Voltage(V)
0
500
1000
1500
2000
2500
Time (s)
Thermistor 1
Thermistor 2
Thermistor 3
Thermistor 4

(b)

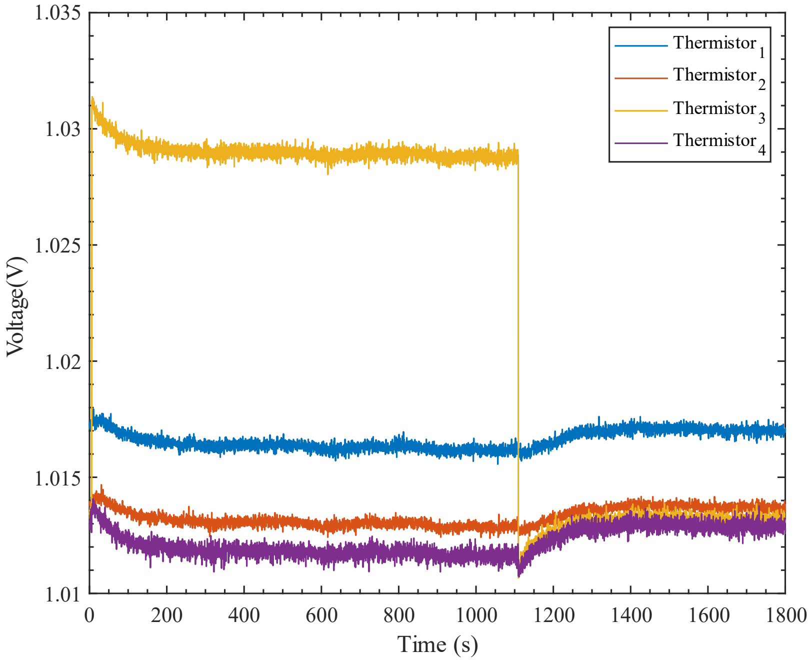

(c)

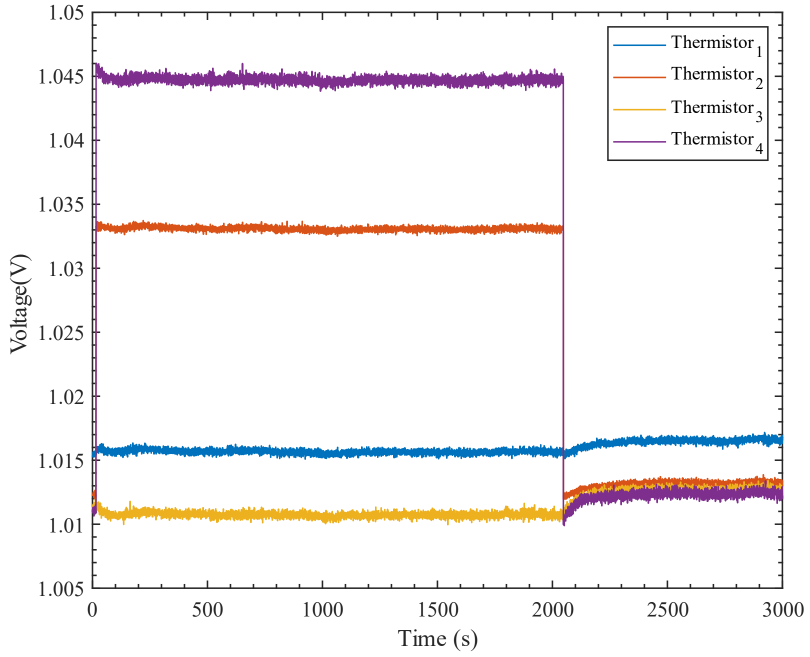

(d)

Figure 4.4. Step responses of thermistors when heaters are triggered by 1V. (a) Heater 1 triggered, (b) Heater 2 triggered, (c) Heater 3 triggered, (d) Heater 4 triggered.

Peaks in these recordings are discernible on graphs. The reason for this is that thermistors and heating elements' ground connections are shared by wire bonding. Hence, the current on the thermistors is significantly affected by the heating elements, which were triggered by step input. An analytical model that was discussed in CHAPTER 2 is implemented for modeling this behavior. In the next section, this model will be presented.

4.3 Plant Identification of The Oven Controlled Package

The thermal model of the package is discussed in two ways: analytical and numerical. Those approaches will be given in detail.

4.3.1 Plant Identification with Analytical Model

The analytical model discussed in Chapter 2 is supplemented with measurements from the test setup and step response experiment. Before starting the experiments, the resistance values of all the heating elements are measured and recorded. In the step response experiment, the current that goes through the heating elements is also collected. Curve fitting is used to find the unknown parameters of thermal resistance ($R_{thermal}$) and thermal capacitance ($C_{thermal}$). Various $R_{thermal}$ and $C_{thermal}$ configurations are placed in the analytical model, and the best fit is obtained. To verify the chosen $R_{thermal}$ and $C_{thermal}$ values, this procedure is executed in various test scenarios. The test scenarios include different environment temperatures and voltage inputs to observe any temperature and voltage dependence of $R_{thermal}$ and $C_{thermal}$. The procurement of these parameters for each heating element first used the recorded data at 25 °C and 1 V step input. After determining the best fit between the analytical model and the step response experiment, $R_{thermal}$ and $C_{thermal}$ values are placed in various test data sets for validation. To validate these selected values, test data that was recorded at 25 °C with 2 V and 3 V step input and at 10 °C with 1 V, 2 V, and 3 V is used. Fitting is obtained for all the test scenarios with the same $R_{thermal}$ and $C_{thermal}$ values, temperature and voltage dependence are not observed. This procedure is carried out for all thermistor-heating element couples.

Figure 4.5 shows the curve-fitting result of the analytical model to the experimental data for Thermistor 1 at 25 °C and 1 V step input of heating element 1.

The parameters that determine the system's main characteristic are $R_{thermal}$, $C_{thermal}$ and electrical resistance of the heating element R_H. When a step input is applied, the thermal capacitance value is indicative of the ramping characteristic as the system approaches steady state. The steady-state point of the system, on the other hand, is determined by the system's thermal resistance value. Furthermore, the magnitude of the voltage jumps caused by the step input is proportional to the electrical resistance of the triggered heating element. After obtaining the best configuration with thermal resistance and thermal capacitance values, this configuration can also be used in different data sets for validation. These values can also be refined with multiple validation data sets, and the final characteristic between a heating element and a relevant thermistor can be determined iteratively. One of the validation results, in which the data was recorded at 10 °C with a 3 V step input, is shared in Figure 4.6.

A plant identification procedure was carried out for each of the thermistor-heating element pairs. In other words, four thermistor-heating element pairs are separate plants and evaluated independently. Even though thermistors are affected by other heating elements outside of their pairs, in this method, the interaction of the plants is neglected. As a result, plant identification was limited to four plants rather than sixteen.

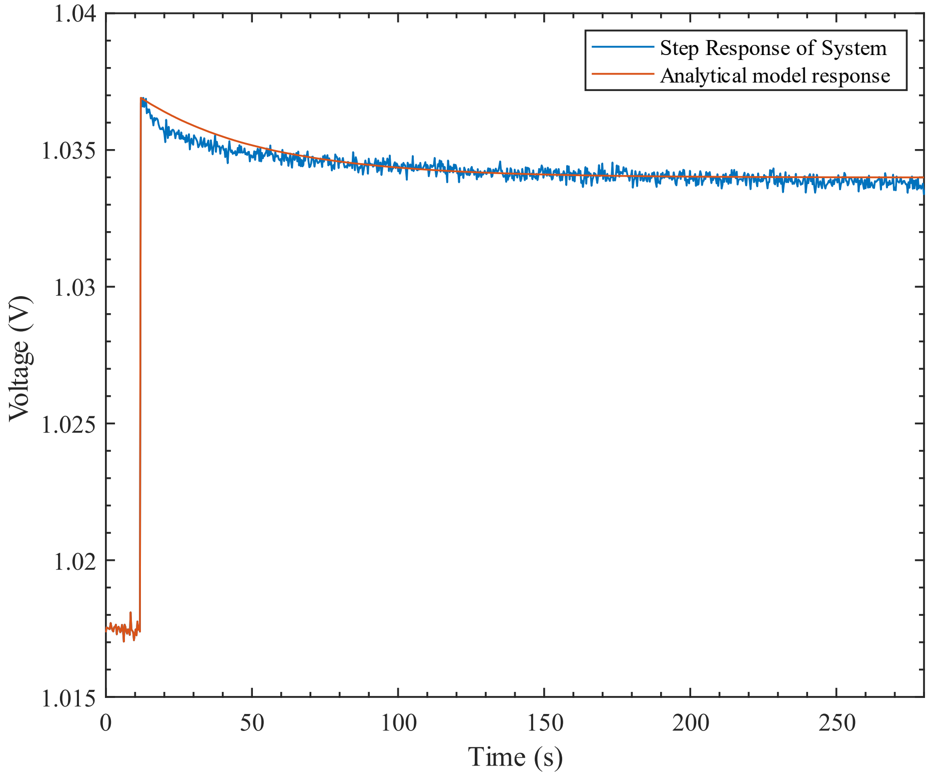

Figure 4.5. Step response of thermistor 1 for 1V at 25 °C.

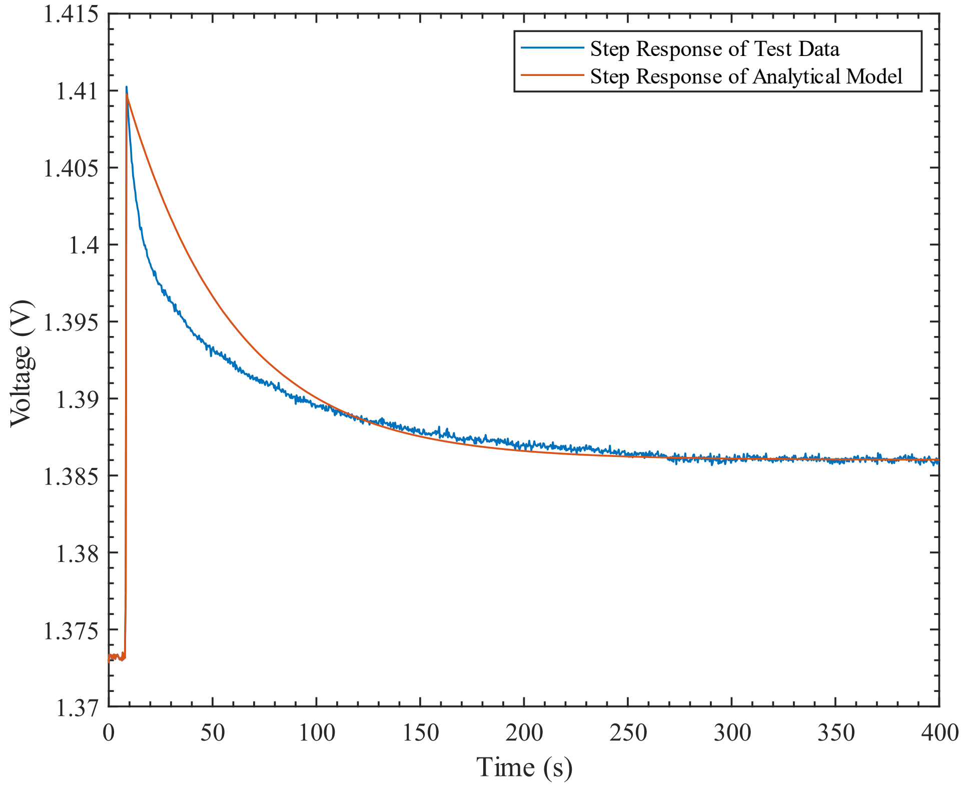

Figure 4.6. Step response of thermistor 1 for 3 V at 10 °C.

Plant identification results are given in Table 4.4.

Table 4.4. Thermal resistance and thermal capacitance values are calculated in the plant identification procedure.

	Plant 1 **H1 on T1**	**Plant 2** **H2 on T2**	**Plant 3** **H3 on T3**	**Plant 4** **H4 on T4**
$R_{thermal}$**(°C/W)**	11.0817	8.04167	8.732	8.492
$C_{thermal}$**(J/°C)**	3.904	5.891	4.648	5.543

4.3.2 Plant Identification with FEM of the Package

4.3.2.1 Steady State Analyses

The goal of steady-state analyses is to identify the system with test results. The first step of the steady-state analysis of the FEM was to evaluate the convective heat transfer coefficient (h). The main difference between the analysis performed in CHAPTER 2 and this subsection is the procedure of iterating the h value until the model is confirmed using test data.

To validate the FEM with test results, boundary conditions should be selected correctly. As mentioned before in CHAPTER 2, heating elements are defined as heat sources. The heat flux boundary condition is convective heat flux, and the outer surface of the oven controlled package and copper tube is selected. The convective heat transfer coefficient, h, was initially estimated to be 10 W/m^2K. Forced convection is selected. Because a fan was installed in the climate chamber to ensure temperature uniformity, an airflow around the package was created. To implement this boundary condition in the FEM, airflow velocity in the climate chamber was measured by an anemometer, this measurement can be seen in Figure 4.6. The measured airflow was 1.54 m/s, and this value was implemented in the steady state analysis of the finite element model with external forced convection and plate transfer coefficient selected in the environment. In this boundary condition, the outer surface of the oven controlled package and the copper tube was selected, and the fluid was defined as air. The absolute pressure of the air was defined as 1 atm. The boundary layer on a flat plate is investigated.

Figure 4.7. Airflow measurement of the climate chamber.

Mesh used in this geometry is the same as in CHAPTER 2, which is extra fine mesh. During the steady-state analysis, constant power was applied to the heating elements, and temperature readings in the thermistor in that pair were obtained by the point evaluation procedure. Figure 4.7 depicts the configuration when only one heat source was turned on, as well as the point probe location where temperature readings were taken. Because the results are compared to test data taken with a 3V step input, the heat source is defined as 0.10 W.

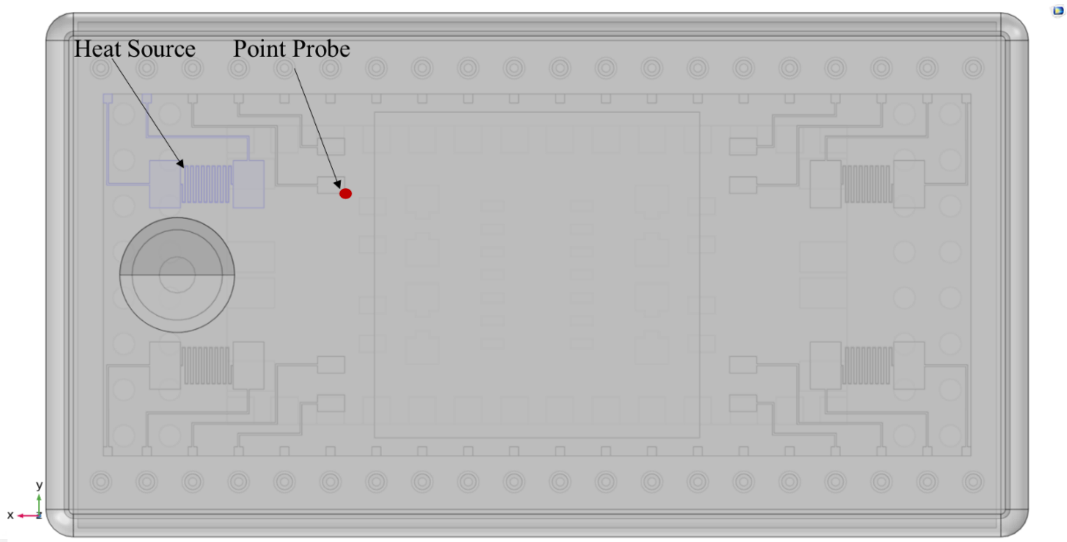

Figure 4.8. A heat source and relevant temperature reading point.

The convective heat transfer coefficient, h, was determined using two different data sets. First, test data from 10 °C ambient temperature was used, and the h value in the FEM was iterated until the probe location read the same temperature value as the test result. After, this procedure was repeated at 25 °C of the environment temperature. In the first case of 10 °C environment temperature, the heat transfer coefficient was calculated as 36 W/m^2K, while in the second case of 25 °C environment temperature, it was obtained as 34 W/m^2K. Temperature plots for 25 °C environment temperature is presented in Figure 4.9.

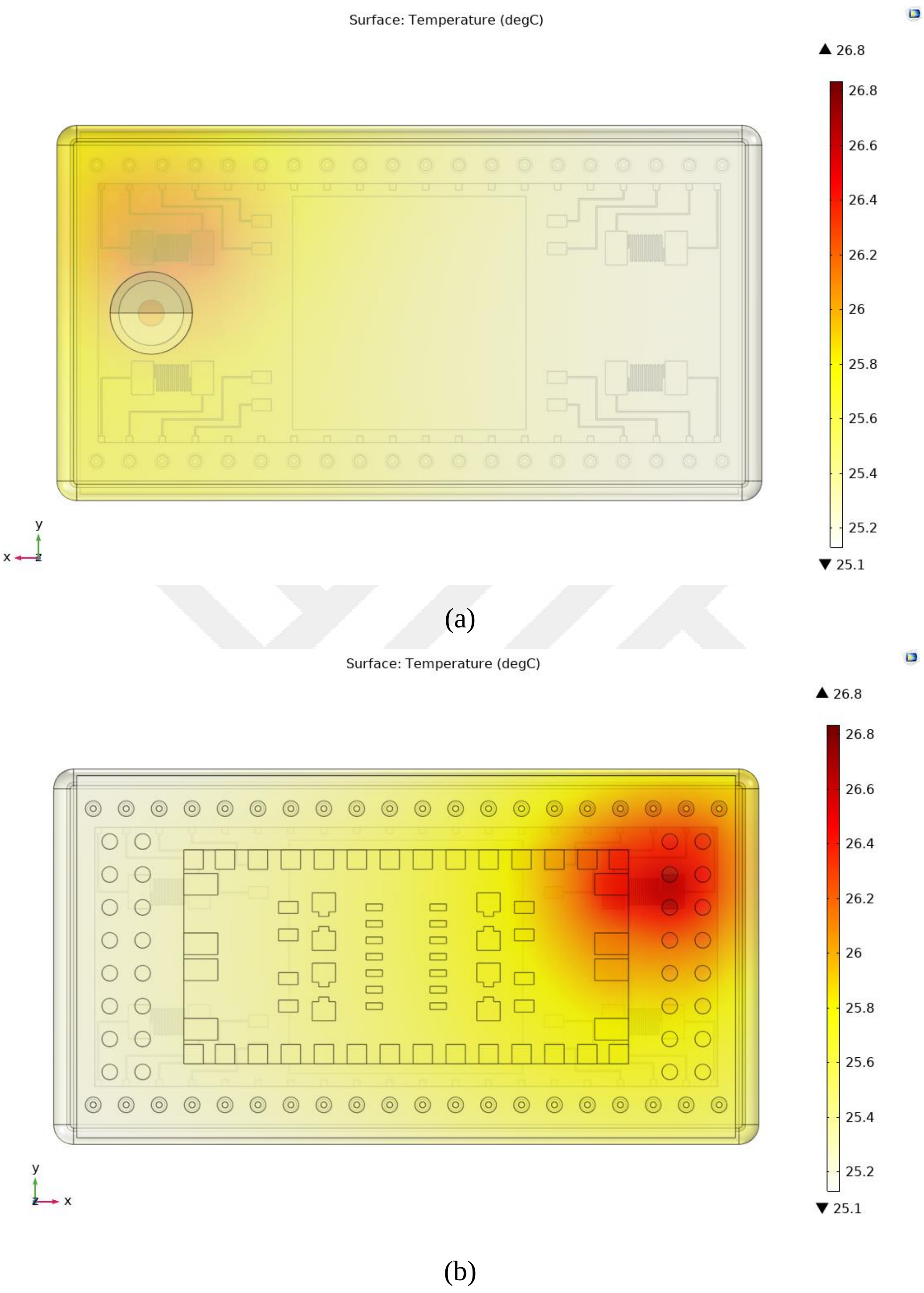

Figure 4.9. Temperature results of steady state FEA at 25 °C. (a) Top view, (b) Bottom view.

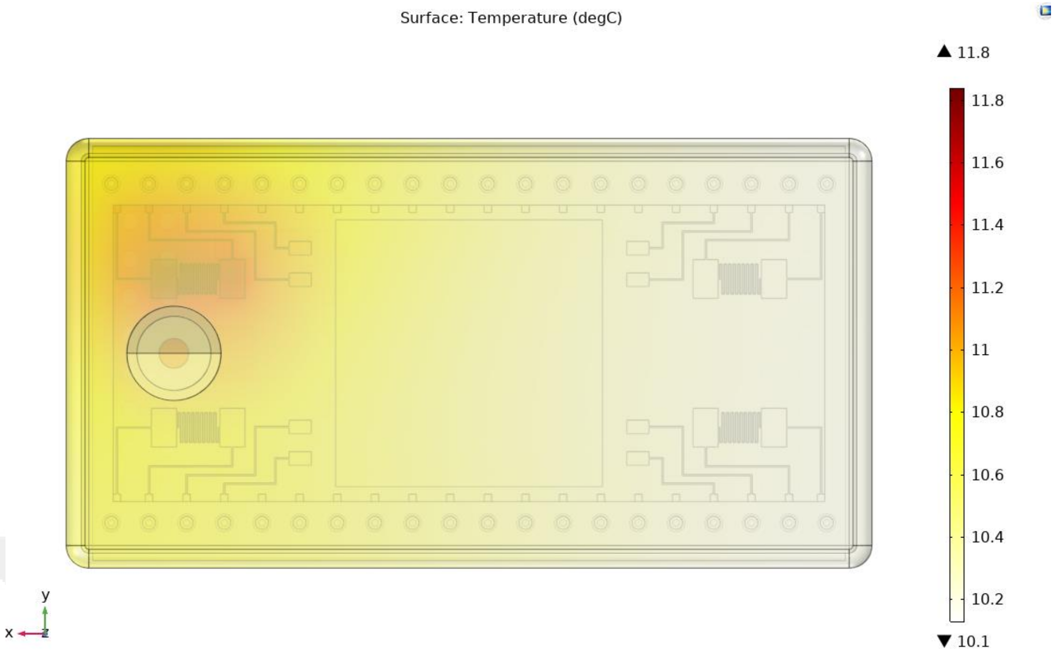

(a)

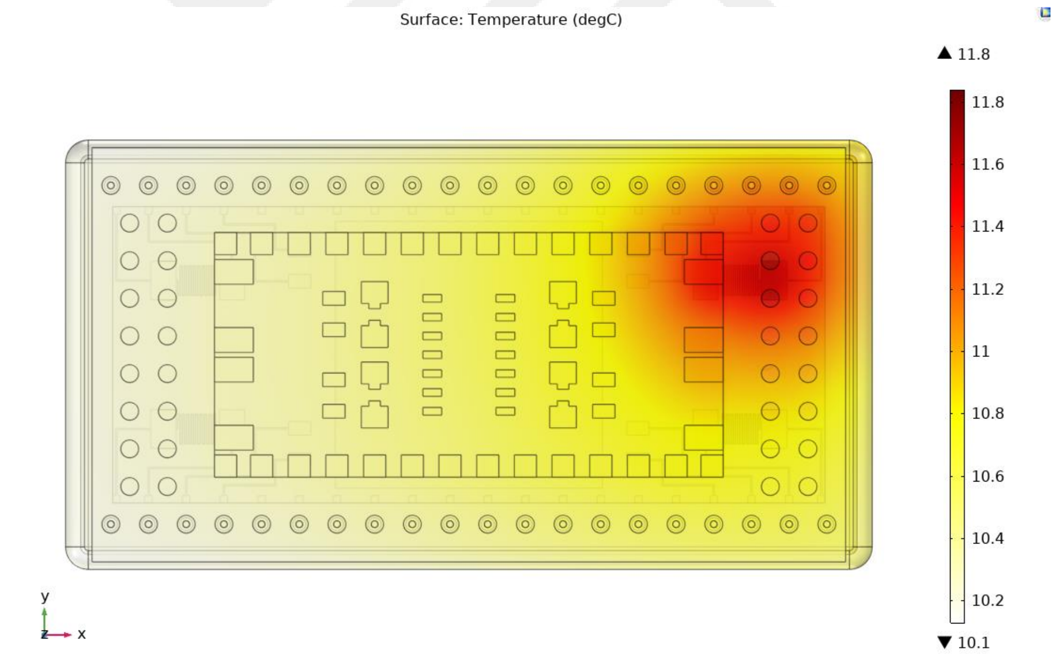

(b)

Figure 4.10. Temperature results of steady state FEA at 10 °C. (a) Top view, (b) Bottom view.

After obtaining h values from steady state analysis, validation is carried out with time dependent analysis.

4.3.2.2 Time Dependent Analyses

A time-dependent analysis was performed to evaluate the COMSOL-generated model and compare the simulated response of the system with test data. The time range in the COMSOL time-dependent study is set to 1000 s, with 20 s steps. The time-dependent analyses employ two distinct environmental conditions. The first one used 10 °C, and the second one used 25 °C. The boundary conditions were chosen in the same way that steady-state analyses were. Heat transfer coefficient h was implemented to the system as calculated in steady state analysis, it was 34 W/m^2K for 25 °C and 36 W/m^2K for 10 °C environment temperature.

To validate the constructed FEM, time dependent analyses were performed for different actuation and detection points. Figure 4.8 shows the location of temperature readings and heat sources. Heat sources are selected as H1 and H3 while thermistor 2 is selected as a temperature detection point. In the climate chamber tests, the heating element 1 (H1) and heating element 3 (H3) were supplied with a constant 8 V. This value equals 0.72 W of power dissipation. Hence, the heat rates of H1 and H3 were defined as 0.72 W in the FEM. Temperature readings from thermistor 2 (T2) were also taken during the tests. The test results and FEM results were compared during the post-processing of the time dependent thermal analyses.

Figure 4.12 shows the test response and FEA response of the system when the environmental temperature is 10 °C. Figure 4.13 shows the test response and FEA response of the system when the environmental temperature is 25 °C. Convective heat transfer coefficient, h has iterated through FEA and curve fitting is obtained for two different environment temperature. Results are presented from h is equal to 10 W/m^2K because steady state analysis was started from that point as explained in the previous subsection.

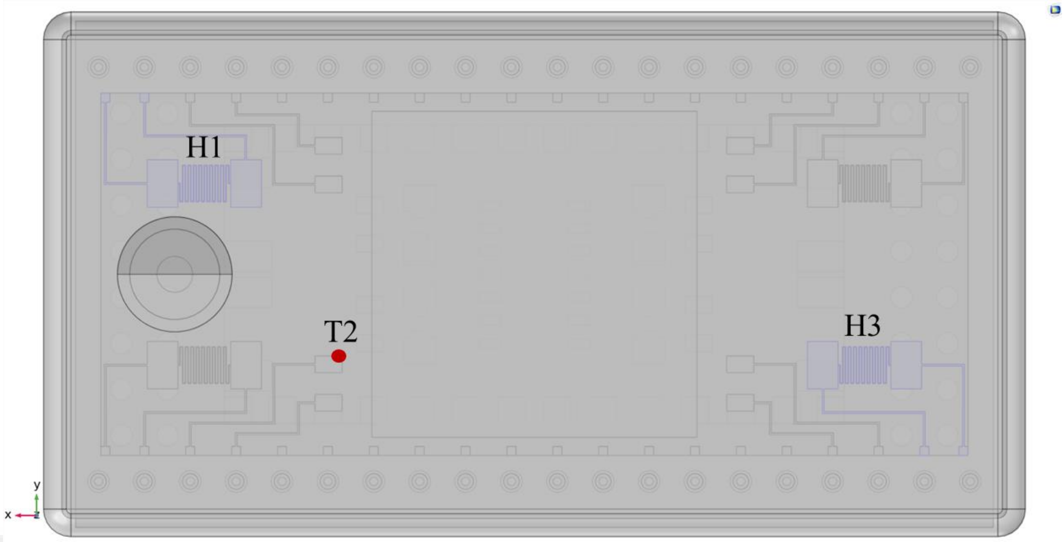

Figure 4.11. Heat sources and temperature reading location in the time dependent analyses.

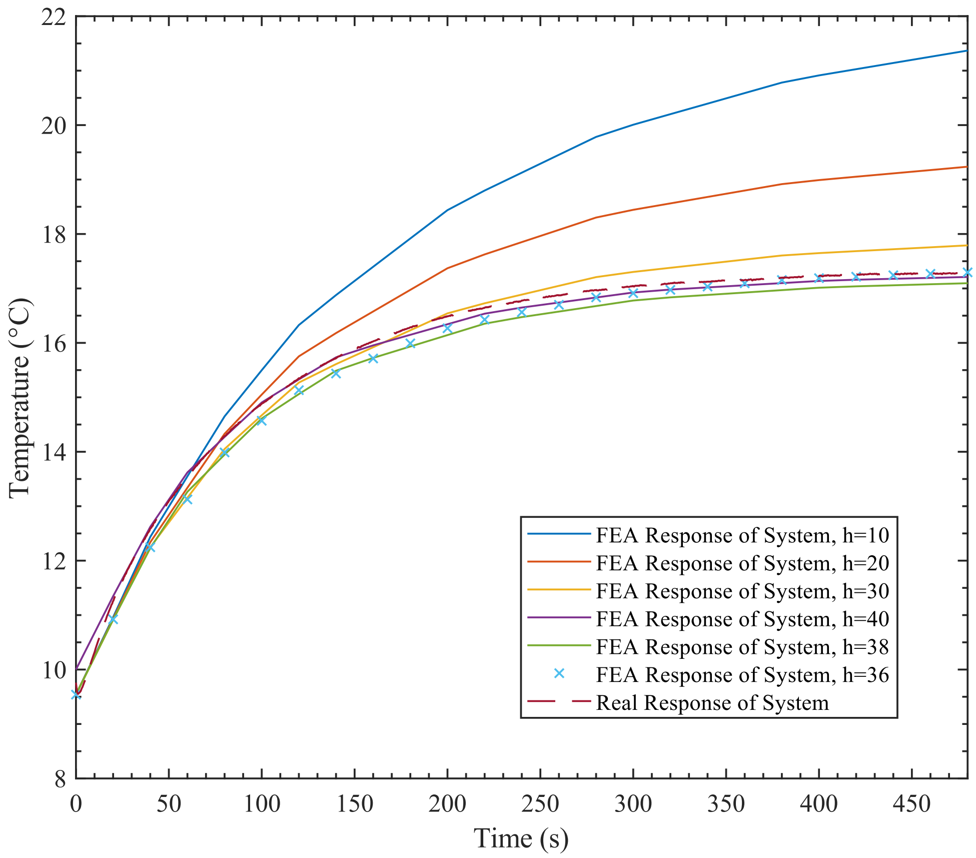

Figure 4.12. Temperature response of T2 at 10 °C environment temperature.

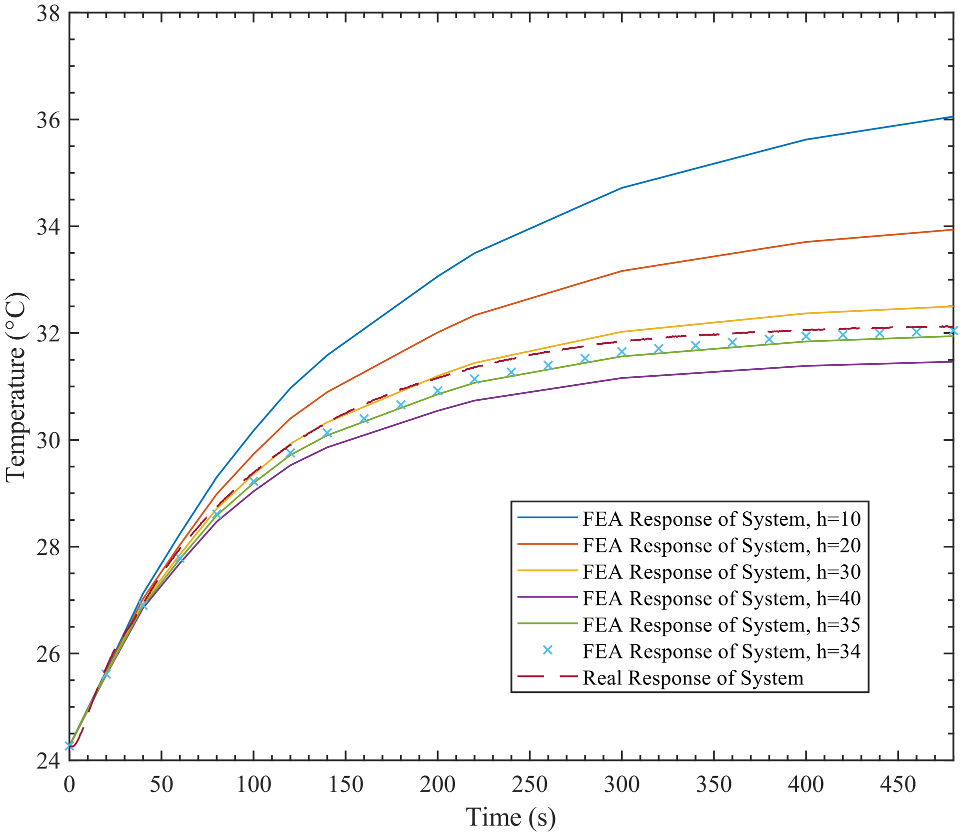

Figure 4.13. Temperature response of 25 °C environment temperature.

As can be seen from Figure 4.12 and Figure 4.13, the temperature response is highly dependent on the h value which is the main parameter when specifying the plant and controller. Hence, in different operating environments, conditions should be completely defined, and the methodology should be repeated.

Figure 4.14 presents the temperature plot for the 400th second of time dependent analysis which the system reach the steady state conditions at 25 °C environment temperature.

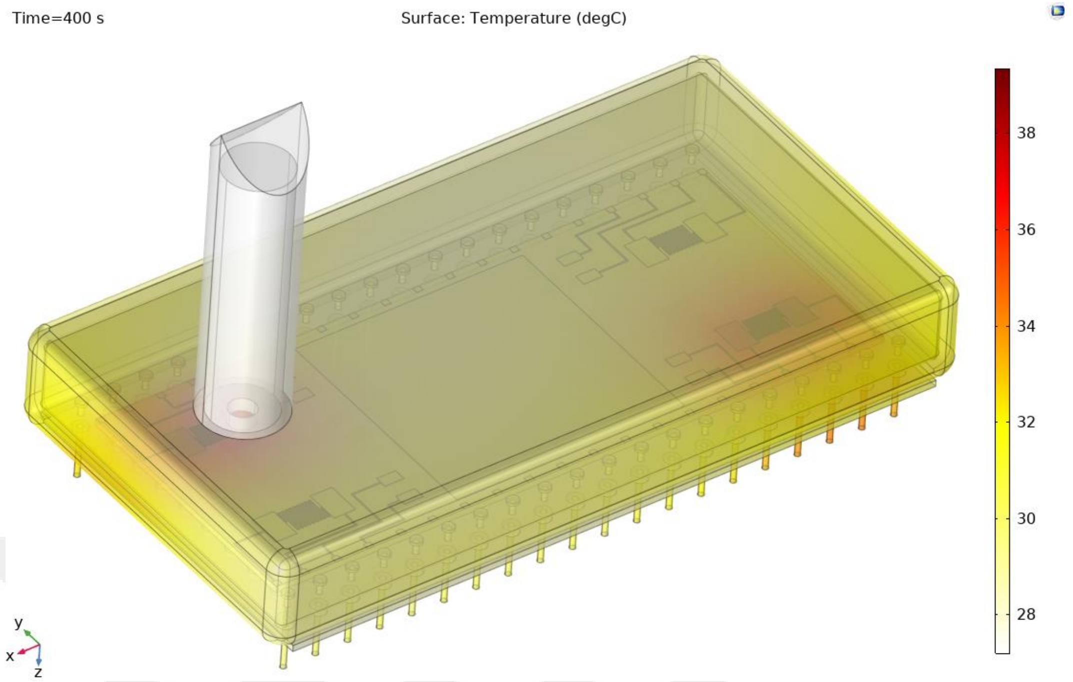

Figure 4.14. Temperature plot for time dependent FEA.

4.4 Closed Loop Controller of The Package

The system characterization of the oven control package enables the design of a closed-loop controller. This closed-loop controller is intended to maintain a constant temperature environment for the MEMS sensor. For this purpose, the temperature is detected at four points, and heating elements are actuated at four points. These four regions are designed to maintain a constant temperature at the same set point. The schematic of the detection and actuation is given in Figure 4.15. Voltage values are read from the thermistors by NI-6218, and this information is transferred to the computer controller. The set temperature and the sensed temperature from the package are compared, and errors are evaluated in the computer. Depending on the controller type and controller parameters, the required power and voltage for each region are calculated, and voltage commands are sent to the power supplies by GPIB protocol.

Two different methods are studied to construct the type of closed-loop controller and its parameters. The first employs an analytical model and its identification, while the second employs the finite element model of the oven-controlled package.

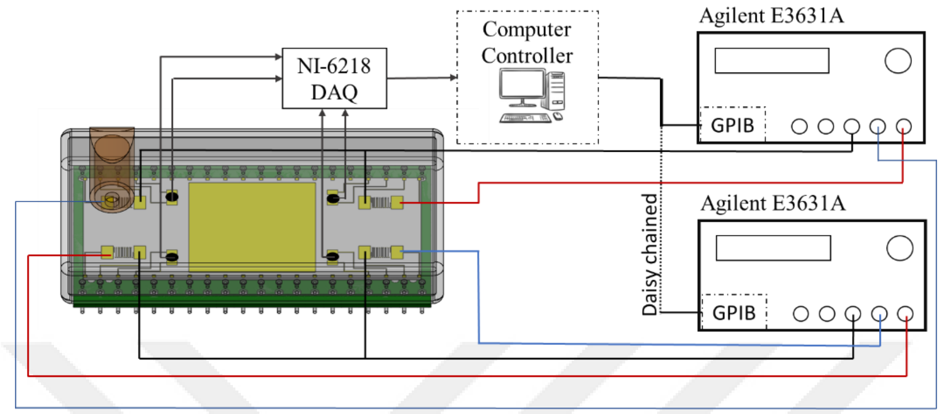

Figure 4.15. Schematic of the temperature detection from thermistors and actuation of the heating elements.

4.4.1 Closed Loop Controller from the Analytical Model

Building an analytical model and identifying the plant is necessary to construct a closed loop controller for the oven control package system. Figure 4.16 presents a block diagram of the closed loop controller for one of the thermistor-heating element pairs.

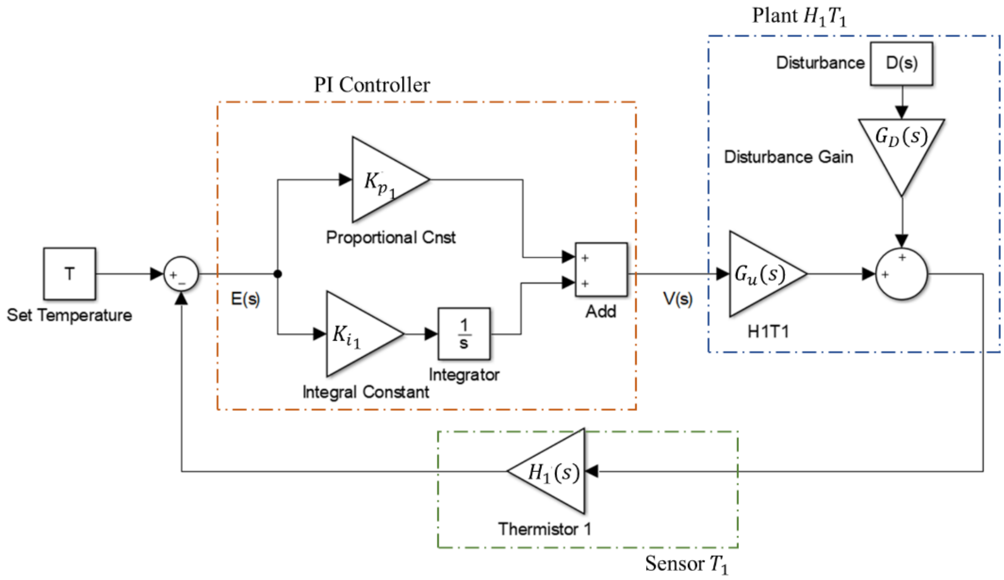

Figure 4.16. Closed loop controller of the heater-thermistor pair.

The main parts of the closed loop controller are the PI controller, the plant, and the feedback element (thermistors). The disturbance can be modeled as other heating elements that can affect the relevant plant. However, they were neglected, as explained in 4.3.1. The transfer function of the plant, on the other hand, is determined by an analytical model and measurements. The analytical model that was developed in CHAPTER 2 was integrated with the measurements from the test setup and the results from the step response tests. An example Simulink model that belongs to Plant 1 is given in Figure 4.16. Simulink models for other plants (Plant 2, Plant 3, and Plant 4) were also built with the same procedure. Parameters of the closed loop controllers for each pair were evaluated separately in the Simulink environment.

Figure 4.17 presents the case when the ambient temperature is 5 °C and the set temperature is 35 °C.

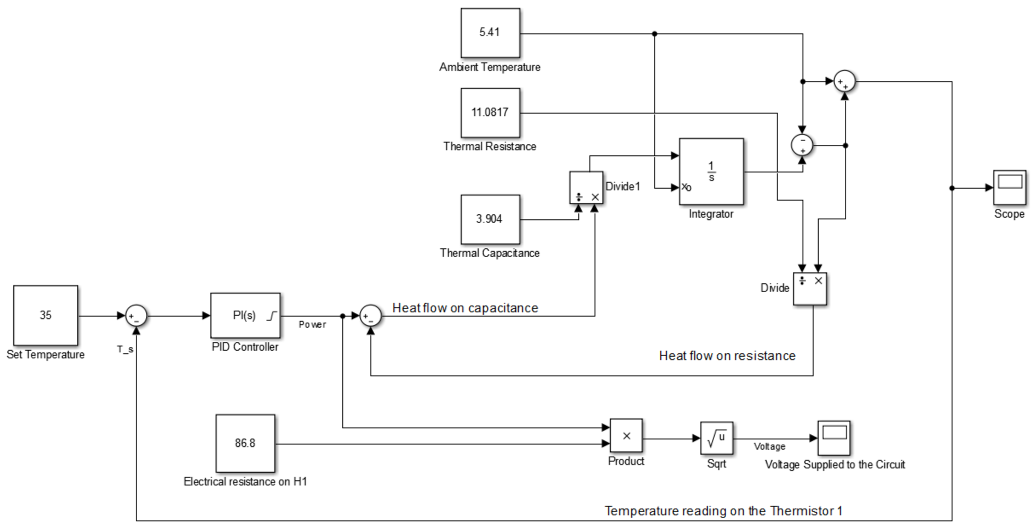

Figure 4.17. The Simulink model for determining the controller parameters.

All controller parameters are tuned in this Simulink environment providing 100 seconds of settling time. Plant characteristics and selected controller parameters are summarized in Table 4.5.

Table 4.5. Plant identification results and controller parameters.

Plants	Actuator	Detector	Plant Identification		PI Controller Parameters	
			Thermal Resistance $R_{thermal}$	Thermal Capacitance $C_{thermal}$	Proportional Constant K_p	Integral Constant K_i
Plant 1	H1	T1	11.0817	3.904	0.3666	0.01981
Plant 2	H2	T2	8.04167	5.891	0.1566	0.0075
Plant 3	H3	T3	8.732	4.648	0.1481	0.0079
Plant 4	H4	T4	8.492	5.543	0.1536	0.007

4.4.1.1 Closed Loop Controller Test Results

A closed-loop controller which is obtained by the analytical model was first used for all the heater-thermistor pairs. Experiments were carried out at 25 °C. Firstly, the set temperature was selected as 40 °C; however, controller parameters were set at 10% of the calculated value to have a safety margin. Setting controller parameters at 10%

of the calculated value brought oscillations to the system, which are presented in Figure 4.18. Another test was conducted with the calculated controller parameters and a set temperature of 30 °C. Figure 4.19 presents the results of this test. It was observed that settling time was sufficient for the application. However, while conducting these tests, the connection in heating element 2 was lost. From then on, heaters 1 and 3 were used to control the temperature. The results of the experiments, which were carried out at 5 °C and 20 °C ambient temperatures, are presented in Figure 4.20. The MATLAB code used for temperature readings and closed loop controller is given in Appendix A. A code from [45] is used for an insight.

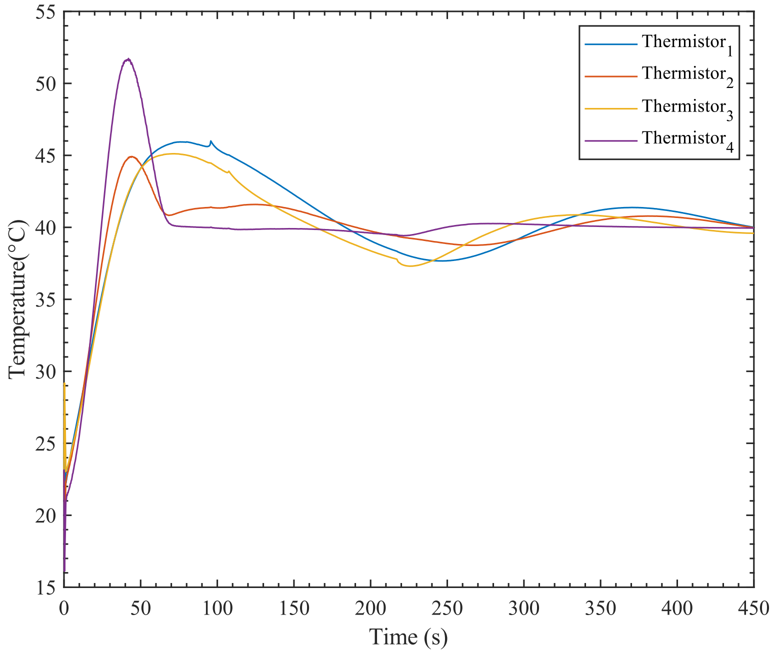

Figure 4.18. Temperature vs time graph when the set temperature was 40 °C and all heaters are running.

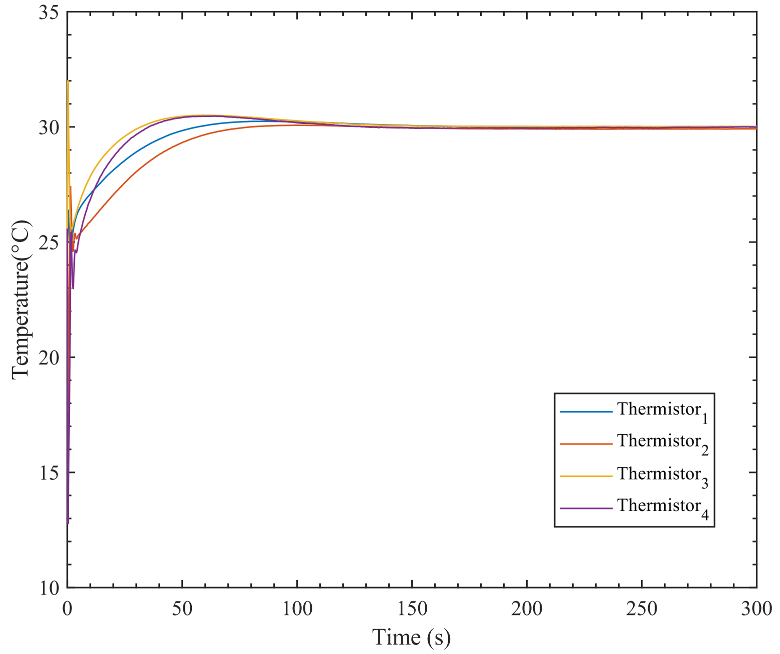

Figure 4.19. Temperature vs time graph when the set temperature was 30 °C and all heaters are running.

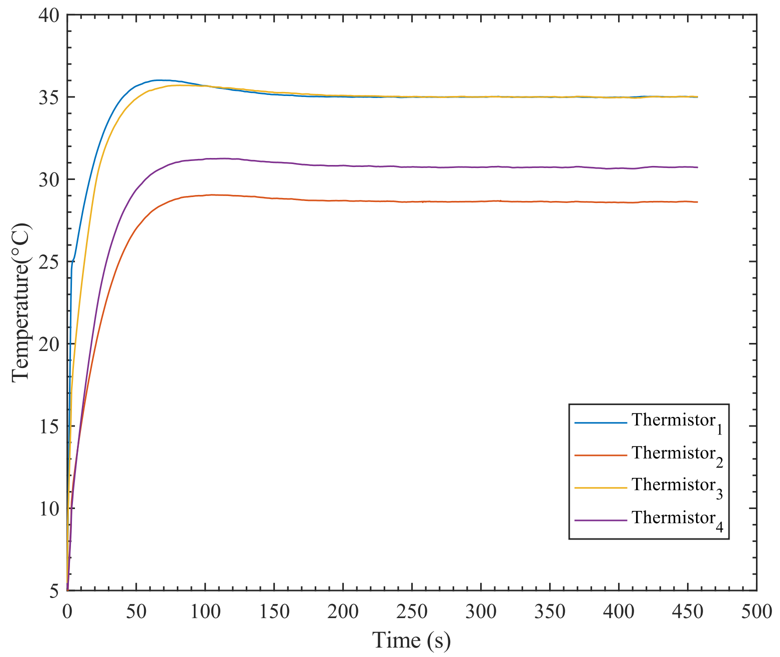

(a)

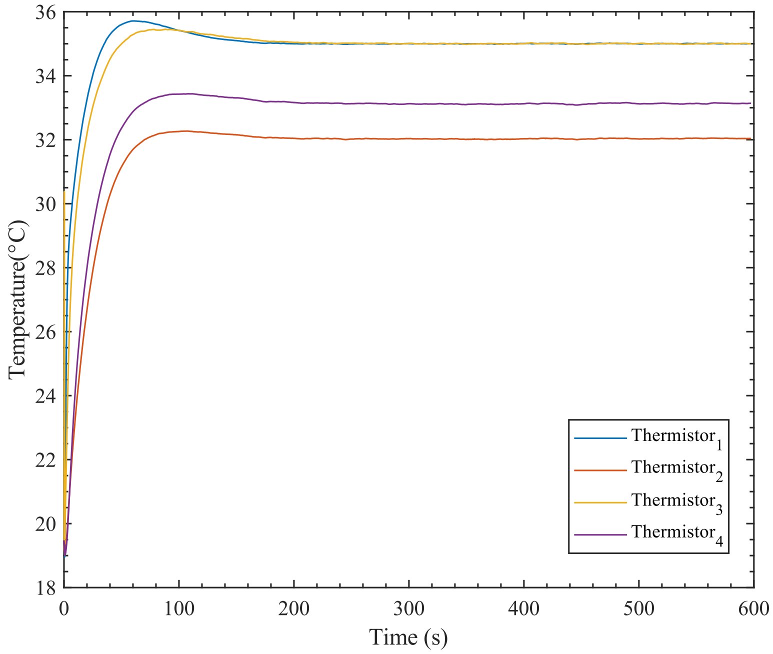

(b)

Figure 4.20. Temperature vs time graph when Heater 1 & Heater 3 are running and the set temperature was 35 °C at (a) 5 °C ambient temperature, (b) 20 °C ambient temperature.

4.4.2 Closed Loop Controller from the FEM

The FEM is used for building the closed loop controller because the analytical model neglects the disturbance effect between the plants, and this can degrade the robustness of the controller. Even though the analytical model is sufficient to build a controller in this thesis, the FEM will be useful for a controller which has a connection to all plants in future work.

As discussed in Section 4.3.2, FEA is used to generate the system's temperature response with respect to time. A plant identification method can also be applied to the system's FEA response. The temperature response of Thermistor 2 when Heater 1 and Heater 3 were powered by a constant of 0.72 W was measured for this purpose. Plant identification was developed in MATLAB with a 96.97% fitting accuracy. As evidenced by the system's first-order temperature response, the transfer function for first-order systems can be expressed as follows:

$$G_u(s) = \frac{K}{Ts + 1} \quad 4.2$$

Gain constant K and time constant T were evaluated with curve fitting from the step response, MATLAB is used for this purpose. After that, PID parameters are tuned manually.

Table 4.6. Plant identification results and controller parameters.

Actuators	Detectors	Plant Identification		PI Controller Parameters	
		Gain Constant K	Time Constant T	Proportional Constant K_p	Integral Constant K_i
H1, H3	T2	9.9853	5.0649	0.14385	0.051139

The parameters of the PI controller from the analytical model and the FEM can be compared. While a similar proportional constant, K_p, is observed in the FEM and analytical model, the FEM has a higher value for the integral constant, K_i. One of the reasons for the similar proportional constant, K_p term is that the parameters are tuned with the same settling time of 100 seconds for each model. For the case of integral constant K_i; while the plant disturbances are neglected in analytical model, they are inseparable from each other in the FEM which directly effects the steady state results. And the steady state error of the response to a step input can be eliminated with the integral constant term K_i [46]. Using the K_i parameter which is obtained from FEM may yield better results for the case when all heaters and thermistors are in operation. Future research efforts will be dedicated to further advancing FEA for this purpose including all plants.

4.5 Characterization of MEMS sensor

The characterization of the MEMS DETF resonator was performed with a frequency response test. The frequency response data were obtained using an Agilent E5061B Network Analyzer, which provides a sine signal to drive electrodes and receives the voltage signal coming from the sense electrodes of the resonator. In the trans-impedance amplifier circuit, AD8608 was used as an op-amp, and 470 kΩ resistance was used.

Frequency response tests were performed for long DETF resonators. The frequency response of the in-phase mode is given in Figure 4.21 and the out-of-phase mode is given in Figure 4.22. Resonance frequency values calculated in the mathematical model, FEM, and test results are summarised in Table 4.7.

Table 4.7. The resonance frequency of the long DETF resonator.

	Long DETF Resonator	
	In-plane Mode	Out-of-plane Mode
Analytical Model	170.75 kHz	
Finite Element Simulation	174.60 kHz	174.74 kHz
Characterization Test Result	166.56 kHz	167.81 kHz

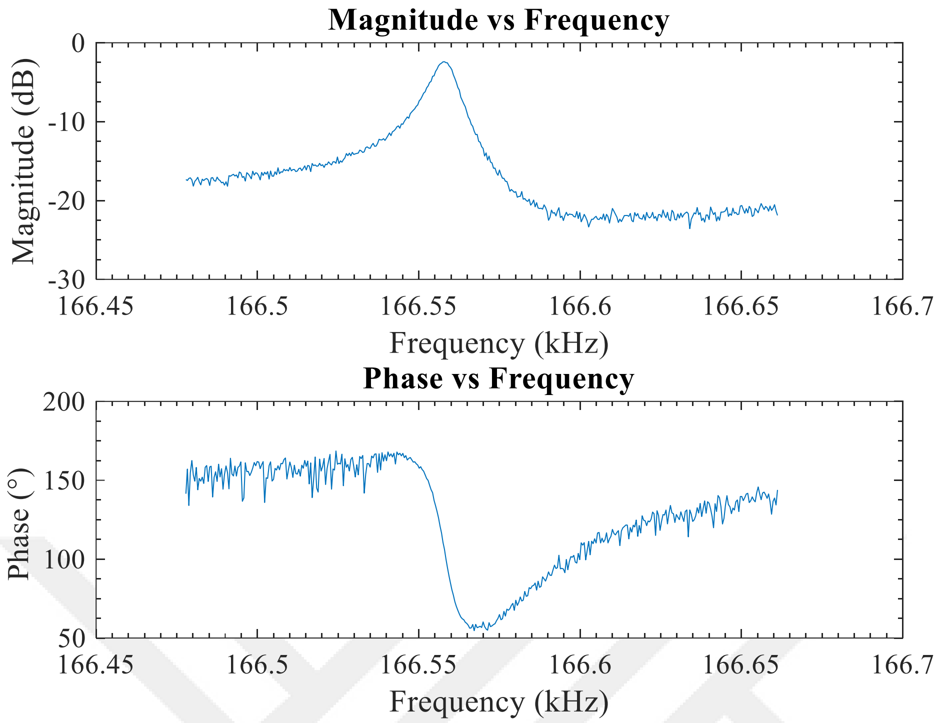

Figure 4.21. Frequency response plot of the in-phase mode.

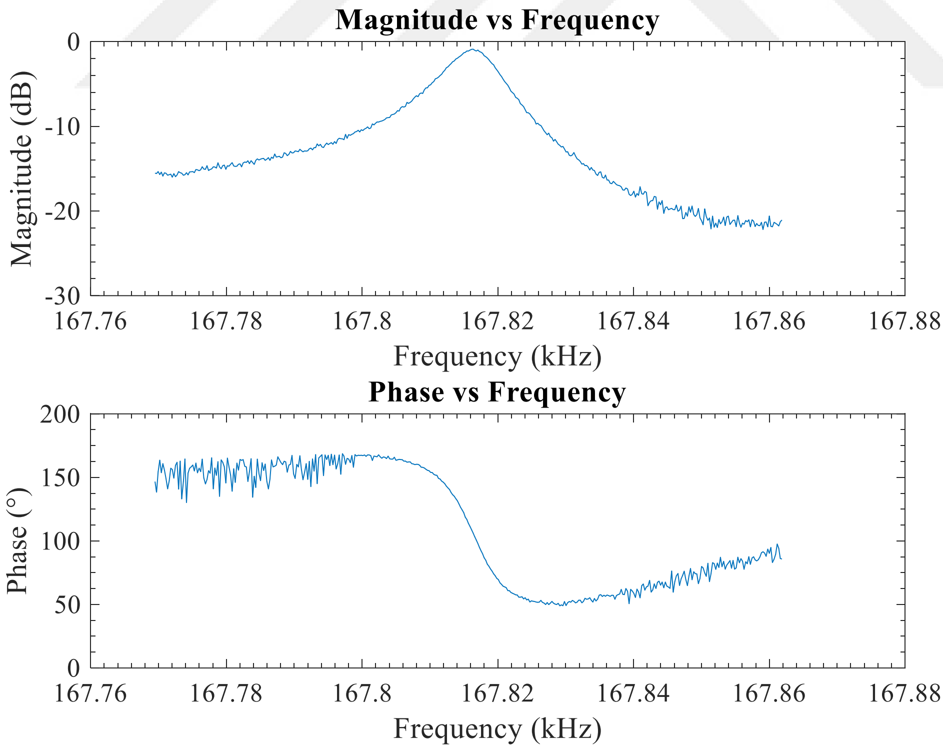

Figure 4.22. Frequency response plot of the out-of-phase mode.

4.6 System-Level Tests

System-level tests are conducted in the climate chamber while a phase of the DETF resonator has been observed in an open-loop configuration. This open loop configuration can be seen in Figure 4.23.

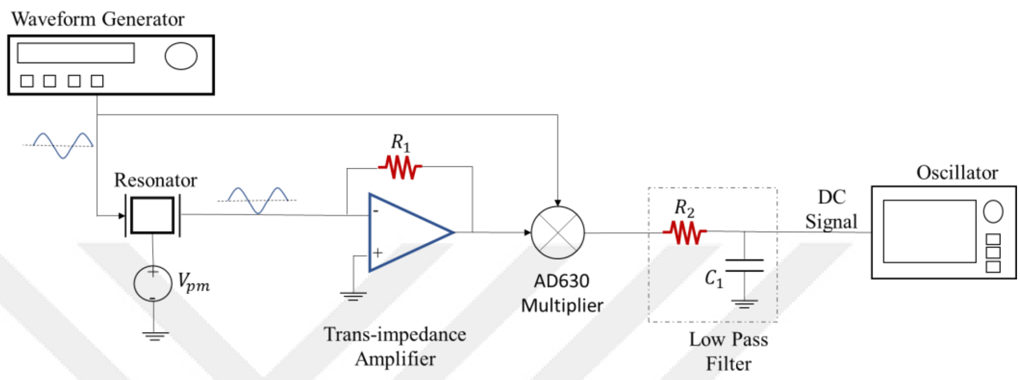

Figure 4.23. Open loop configuration to observe the phase change of the resonator.

The waveform generator used in this circuit generates a sine wave at the resonance frequency of the DETF with an amplitude of 10 mV_{pp}. The signal from the sense electrodes of the resonator is amplified by the operational amplifier AD8608. A modulator AD630 is used for superposing the information signal (the signal from the sense electrodes) onto a carrier signal. In essence, this operation is a mathematical multiplication.

When the sine wave generated by the waveform generator is expressed as:

$$f_1(t) = Asin(wt) \qquad 4.3$$

Moreover, the sine wave from the sense electrodes:

$$f_2(t) = Bsin(wt + \Phi) \qquad 4.4$$

When those signals are multiplied in the AD630:

$$f_1(t)f_2(t) = AB(sin(wt))(sin(wt + \Phi)) \qquad 4.5$$

$$f_1(t)f_2(t) = \frac{AB}{2}(\cos(\Phi) - \cos(2\omega t + \Phi)) \qquad 4.6$$

A low-pass filter should be used to process this signal to remove the time-dependent term and produce only a DC signal. This signal in the output of the Low Pass Filter can be expressed as below:

$$f_{LPF} = \frac{AB}{2}\cos(\Phi) \qquad 4.7$$

The frequency of the waveform generator should be set up so that phase is nearly zero to obtain simply the constant term $\frac{AB}{2}$.

Hence, the resonance frequency measurement of the DETF resonator can be carried out while observing the output of the low-pass filter. These tests were conducted in two different aspects. The first one was performed when the heating elements were not working, and the second one was conducted when the heating elements were set to a constant temperature. Figure 4.24 represents the configuration when a closed-loop temperature controller was operating, and the system was stabilized at a set temperature which is 35 °C. On the computer screen, a stabilized system can be seen. The drive signal from the waveform generator, the output sine signal from the sense electrodes, and the phase signal can be seen on the oscillator's screen.

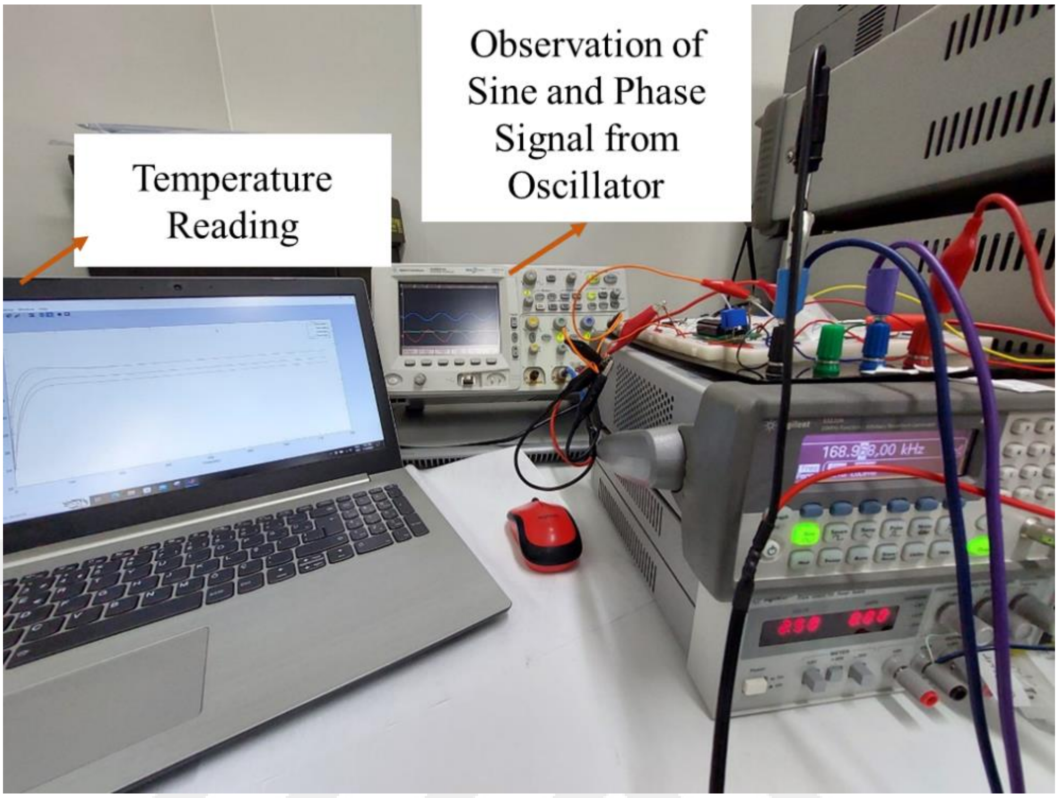

Figure 4.24. Observation of the drive signal from the waveform generator, output signal from the sense electrodes, and phase signal while the system was stabilized under set temperature.

4.6.1 System-Level Test Results

System-level tests were performed between 5 °C and 35 °C. The frequency response of the MEMS resonator was recorded in 5 °C steps. Firstly, data was recorded without oven control. After the oven control strategy was used in the package, the frequency was recorded again. A comparison between the results is given in Figure 4.25, and the improvement of the frequency stability is represented in this graph.

Previously, the resonance frequency of the MEMS sensor deviated by 3120 Hz for in-phase mode and 3140 Hz for out-of-phase mode between 5 °C and 35 °C. The temperature effect on the MEMS sensor was compensated with the oven controlled package design, and the deviation of frequency between this temperature range dropped to 380 Hz for in-phase mode and 154 Hz for out-of-phase mode.

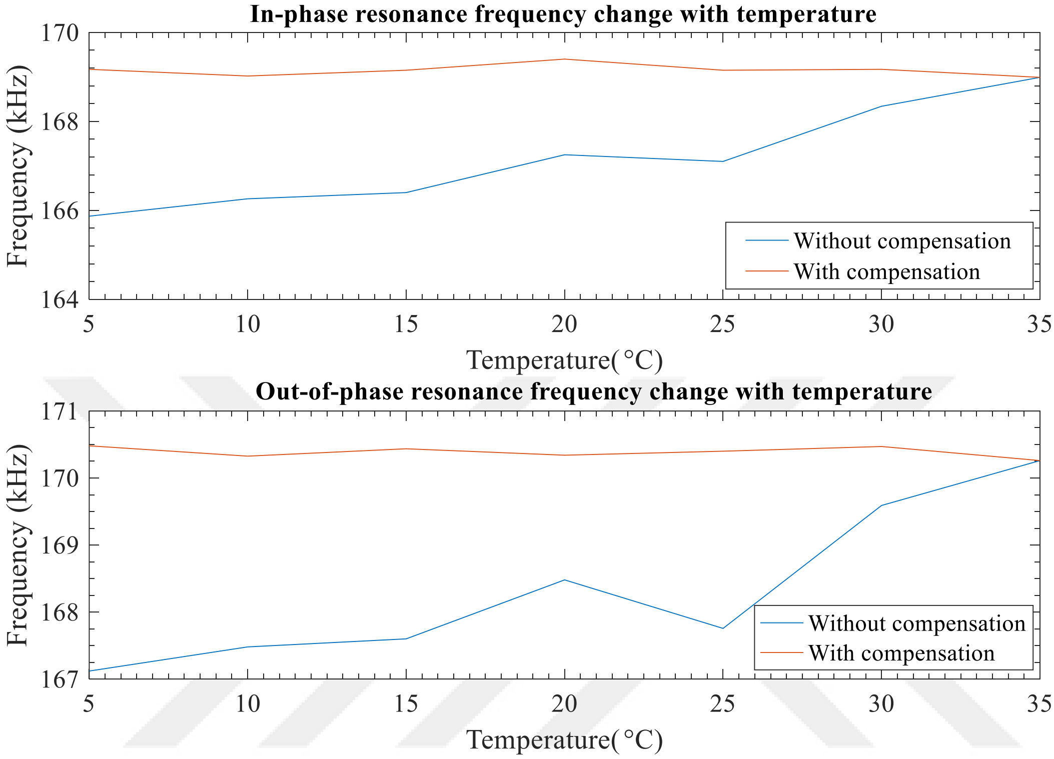

Figure 4.25. Resonance frequency change of the DETF resonator from 5 °C to 35 °C with and without oven control.

CHAPTER 5

CONCLUSION AND FUTURE WORKS

This thesis reported a package-level temperature compensation method for a MEMS sensor. Temperature compensation is achieved by active oven control. Firstly, the material of the substrate is decided for constructing a temperature control surface on where the MEMS sensor should be placed. The heat generation, temperature detection, and die attachment areas are specified. A mathematical model is developed to model the thermal response of the system. Before the production step, the finite element model of the package is constructed for validating the design. The identification and behavior of the system are modeled by the FEM. A closed-loop temperature controller is built from an analytical model and FEM. The MEMS sensor is characterized by an analytical model, FEM, and frequency response tests. System-level tests of the package and sensor are carried out in the climate chamber. Fabrication and tests are carried out in METU MEMS Center. The following is a summary of the conclusions reached as a result of these studies:

1. Oven control methods as active temperature compensation for MEMS sensors are investigated. An alumina material is selected as the substrate material of the temperature control surface because its coefficient of thermal expansion (CTE) value is close to silicon (material of MEMS sensor) and kovar (material of package). The heating elements and temperature detection areas are specified on the substrate. The trans-impedance amplifier of the MEMS sensor is built with the same material, alumina. And it is integrated into the package to enhance temperature stability in the first amplifier circuit.
2. A mathematical model and FEM are constructed for the package's thermal model. Additionally, an electrical model is built and integrated into the thermal model. Characterization of MEMS sensor is presented with FEM, and it is validated by a mathematical model.

3. Fabrication of alumina substrates is explained. The problems and optimization methods for delamination of the metal layer from alumina surface are discussed. The vacuum packaging method and sealing test are presented.
4. System characterization test setup is constructed. The resolution of temperature detection is explained. Plant identification from the analytical model and FEM are finalized and a closed-loop controller is built. A read-out circuit is built for the MEMS sensor and the deviation of the resonance frequency is observed between 5 °C and 35 °C. The deviation for the in-phase mode of the resonator is 3120 Hz while for the out-of-phase mode, it is 3140 Hz. The oven-controlled package reduces this resonance frequency deviation and enhances frequency stability. The deviation for the in-phase mode of the resonator is 380 Hz, while for the out-of-phase mode, it is 154 Hz when the temperature controller is integrated.

Although frequency stability for MEMS sensor is enhanced, the design of the heating elements should be refined and the locations of the heating elements can be optimized. The following studies are planned to improve the oven controlled package:

1. As a result of this study's conclusion that the deposited metal is sufficient to produce heat-generating elements, its design can be altered to reduce temperature gradients in the package. This could assist with controlling the temperature. Moreover, power consumption can be decreased with the optimization of heating elements.
2. Rather than using power supplies as a voltage input to the heating elements, power op-amps can be integrated into the temperature control system.
3. A PLL loop should be constructed for closed-loop frequency recording.
4. The FEM can be used for analyzing extreme conditions.

REFERENCES

[1] G. Wu, J. Xu, E. J. Ng, and W. Chen, “MEMS Resonators for Frequency Reference and Timing Applications,” *Journal of Microelectromechanical Systems*, vol. 29, no. 5, pp. 1137–1166, Oct. 2020, doi: 10.1109/JMEMS.2020.3020787.

[2] M. A. Hopcroft, “Temperature-stabilized silicon resonators for frequency references,” *PhD thesis in Mechanical Engineering for Stanford University*, no. September, 2007.

[3] D. M. Yang, “Oven-Controlled Inertial Sensors,” 2019.

[4] W. Pang, H. Yu, H. Zhang, and E. S. Kim, “Temperature-compensated film bulk acoustic resonator above 2 GHz,” *IEEE Electron Device Letters*, vol. 26, no. 6, pp. 369–371, Jun. 2005, doi: 10.1109/LED.2005.848113.

[5] R. Melamud *et al.*, “Temperature-insensitive composite micromechanical resonators,” *Journal of Microelectromechanical Systems*, vol. 18, no. 6, pp. 1409–1419, Dec. 2009, doi: 10.1109/JMEMS.2009.2030074.

[6] D. R. Myers, “MEMS Resonant Strain Sensor Integration,” 2010.

[7] J. R. Clark, A. R. Brown, G. He, and W. T. Hsu, “Temperature compensated overtone resonators,” in *2013 Transducers and Eurosensors XXVII: The 17th International Conference on Solid-State Sensors, Actuators and Microsystems, TRANSDUCERS and EUROSENSORS 2013*, 2013, pp. 794–797. doi: 10.1109/Transducers.2013.6626886.

[8] V. A. Thakar, Z. Wu, A. Peczalski, and M. Rais-Zadeh, “Piezoelectrically transduced temperature-compensated flexural-mode silicon resonators,” *Journal of Microelectromechanical Systems*, vol. 22, no. 3, pp. 815–823, 2013, doi: 10.1109/JMEMS.2013.2245403.

[9] Institute of Electrical and Electronics Engineers, *MEMS 2019 : the 32nd IEEE International Conference on Micro Electro Mechanical Systems : January 27-31, 2019, Coex, Seoul, Korea.*

[10] A. K. Samarao and F. Ayazi, “Temperature compensation of silicon micromechanical resonators via degenerate doping,” in *Technical Digest - International Electron Devices Meeting, IEDM*, 2009. doi: 10.1109/IEDM.2009.5424221.

[11] Y. Ma *et al.*, “Doped silicon temperature compensation of surface acoustic wave devices,” in *IEEE International Ultrasonics Symposium, IUS*, IEEE Computer Society, Sep. 2020. doi: 10.1109/IUS46767.2020.9251709.

[12] W. Chen, W. Jia, Y. Xiao, Z. Feng, and G. Wu, “A Temperature-Stable and Low Impedance Piezoelectric MEMS Resonator for Drop-in Replacement of Quartz Crystals,” *IEEE Electron Device Letters*, 2021, doi: 10.1109/LED.2021.3094319.

[13] W. T. Hsu and C. T. C. Nguyen, “Geometric stress compensation for enhanced thermal stability in micromechanical resonators,” *Proceedings of the IEEE Ultrasonics Symposium*, vol. 1, pp. 945–948, 1998, doi: 10.1109/ultsym.1998.762298.

[14] W. T. Hsu, J. R. Clark, and C. T. C. Nguyen, “Mechanically temperature-compensated flexural-mode micromechanical resonators,” in *Technical Digest - International Electron Devices Meeting*, 2000, pp. 399–402. doi: 10.1109/iedm.2000.904340.

[15] A. K. Samarao, G. Casinovi, and F. Ayazi, “Passive TCF compensation in high Q silicon micromechanical resonators,” in *Proceedings of the IEEE International Conference on Micro Electro Mechanical Systems (MEMS)*, 2010, pp. 116–119. doi: 10.1109/MEMSYS.2010.5442553.

[16] G. K. Ho, K. Sundaresan, S. Pourkamali, and F. Ayazi, “Low-motional-impedance highly-tunable I2 resonators for temperature-compensated

reference oscillators," in *Proceedings of the IEEE International Conference on Micro Electro Mechanical Systems (MEMS)*, 2005, pp. 116–120. doi: 10.1109/memsys.2005.1453881.

[17] K. Sundaresan, G. K. Ho, S. Pourkamali, and F. Ayazi, "A two-chip, 4-MHz, microelectromechanical reference oscillator," in *Proceedings - IEEE International Symposium on Circuits and Systems*, 2005, pp. 5461–5464. doi: 10.1109/ISCAS.2005.1465872.

[18] G. K. Ho, K. Sundaresan, S. Pourkamali, and F. Ayazi, "Micromechanical IBARs: Tunable high-Q resonators for temperature- compensated reference oscillators," *Journal of Microelectromechanical Systems*, vol. 19, no. 3, pp. 503–515, Jun. 2010, doi: 10.1109/JMEMS.2010.2044866.

[19] H. K. Lee, R. Melamud, B. Kim, M. A. Hopcroft, J. C. Salvia, and T. W. Kenny, "Electrostatic tuning to achieve higher stability microelectromechanical composite resonators," *Journal of Microelectromechanical Systems*, vol. 20, no. 6, pp. 1355–1365, Dec. 2011, doi: 10.1109/JMEMS.2011.2168083.

[20] D. E. Serrano, R. Tabrizian, and F. Ayazi, "Tunable piezoelectric MEMS resonators for real-time clock," in *Proceedings of the IEEE International Frequency Control Symposium and Exposition*, 2011. doi: 10.1109/FCS.2011.5977885.

[21] D. D. Shin *et al.*, "Electrostatic tuning of temperature coefficient of frequency of anisotropic disk-shaped resonators," in *4th IEEE International Symposium on Inertial Sensors and Systems, INERTIAL 2017 - Proceedings*, Institute of Electrical and Electronics Engineers Inc., May 2017, pp. 164–167. doi: 10.1109/ISISS.2017.7935664.

[22] K. Sundaresan, G. K. Ho, S. Pourkamali, and F. Ayaji, "Electronically temperature compensated silicon bulk acoustic resonator reference

oscillators," *IEEE J Solid-State Circuits*, vol. 42, no. 6, pp. 1425–1434, Jun. 2007, doi: 10.1109/JSSC.2007.896521.

[23] M. Perrott *et al.*, "A temperature-to-digital converter for a MEMS-based programmable oscillator with better than ±0.5ppm frequency stability," in *Digest of Technical Papers - IEEE International Solid-State Circuits Conference*, 2012, pp. 206–207. doi: 10.1109/ISSCC.2012.6176977.

[24] G. Wu *et al.*, "Wafer-Level Vacuum-Packaged High-Performance AlN-on-SOI Piezoelectric Resonator for Sub-100-MHz Oscillator Applications," *IEEE Transactions on Industrial Electronics*, vol. 65, no. 4, pp. 3576–3584, Apr. 2018, doi: 10.1109/TIE.2017.2748041.

[25] C. Nguyen and R. T. Howe, "Microresonator Frequency Control ans Stabilization Using an Integrated Micro-Oven," *7th International Conference on Solid-State Sensors and Actuators (Transducers'93))*, 1993.

[26] K. Sundaresan, G. K. Ho, S. Pourkamali, and F. Ayazi, "A low phase noise 100MHz silicon BAW reference oscillator," in *Proceedings of the Custom Integrated Circuits Conference*, 2006, pp. 841–844. doi: 10.1109/CICC.2006.320843.

[27] C. M. Jha *et al.*, "Thermal isolation of encapsulated MEMS resonators," *Journal of Microelectromechanical Systems*, vol. 17, no. 1, pp. 175–184, Feb. 2008, doi: 10.1109/JMEMS.2007.904332.

[28] S. H. Lee, J. Cho, S. W. Lee, M. F. Zaman, F. Ayazi, and K. Najafil, "A low-power oven-controlled vacuum package technology for high-performance MEMS," in *Proceedings of the IEEE International Conference on Micro Electro Mechanical Systems (MEMS)*, 2009, pp. 753–756. doi: 10.1109/MEMSYS.2009.4805492.

[29] J. Lim, H. Kim, T. N. Jackson, K. Choi, and D. Kenny, "An ultra-compact and low-power oven- controlled crystal oscillator design for precision timing

applications," *IEEE Trans Ultrason Ferroelectr Freq Control*, vol. 57, no. 9, pp. 1906–1914, Sep. 2010, doi: 10.1109/TUFFC.2010.1638.

[30] J. C. Salvia, R. Melamud, S. A. Chandorkar, S. F. Lord, and T. W. Kenny, "Real-time temperature compensation of mems oscillators using an integrated micro-oven and a phase-locked loop," *Journal of Microelectromechanical Systems*, vol. 19, no. 1, pp. 192–201, Feb. 2010, doi: 10.1109/JMEMS.2009.2035932.

[31] K. E. Wojciechowski, M. S. Baker, P. J. Clews, and R. H. Olsson, "A Fully Integrated Oven Controlled Microelectromechanical Oscillator - Part I: Design and Fabrication," *Journal of Microelectromechanical Systems*, vol. 24, no. 6, pp. 1782–1794, Dec. 2015, doi: 10.1109/JMEMS.2015.2441037.

[32] K. E. Wojciechowski and R. H. Olsson, "A Fully Integrated Oven Controlled Microelectromechanical Oscillator - Part II: Characterization and Measurement," *Journal of Microelectromechanical Systems*, vol. 24, no. 6, pp. 1795–1802, Dec. 2015, doi: 10.1109/JMEMS.2015.2441045.

[33] C. Xu, J. Segovia-Fernandez, H. J. Kim, and G. Piazza, "Temperature-stable piezoelectric MEMS resonators using integrated ovens and simple resistive feedback circuits," *Journal of Microelectromechanical Systems*, vol. 26, no. 1, pp. 187–195, Feb. 2017, doi: 10.1109/JMEMS.2016.2626920.

[34] C. S. Liu, R. Tabrizian, and F. Ayazi, "A ±0.3 ppm Oven-Controlled MEMS Oscillator Using Structural Resistance-Based Temperature Sensing," *IEEE Trans Ultrason Ferroelectr Freq Control*, vol. 65, no. 8, pp. 1492–1499, Aug. 2018, doi: 10.1109/TUFFC.2018.2843781.

[35] Z. Liu, L. Du, Z. Zhao, J. Liu, P. Wu, and Z. Fang, "A chip-level oven-controlled system used to improve accuracy of silicon piezoresistive pressure sensor," *Measurement (Lond)*, vol. 143, pp. 1–10, Sep. 2019, doi: 10.1016/j.measurement.2019.05.014.

[36] H. K. Kwon, L. C. Ortiz, G. D. Vukasin, Y. Chen, D. D. Shin, and T. W. Kenny, “An Oven-Controlled MEMS Oscillator (OCMO) with Sub 10mw, ± 1.5 PPB Stability over Temperature,” in *2019 20th International Conference on Solid-State Sensors, Actuators and Microsystems and Eurosensors XXXIII, TRANSDUCERS 2019 and EUROSENSORS XXXIII*, Institute of Electrical and Electronics Engineers Inc., Jun. 2019, pp. 2072–2075. doi: 10.1109/TRANSDUCERS.2019.8808255.

[37] L. C. Ortiz *et al.*, “Low-Power Dual Mode MEMS Resonators with PPB Stability over Temperature,” *Journal of Microelectromechanical Systems*, vol. 29, no. 2, pp. 190–201, Apr. 2020, doi: 10.1109/JMEMS.2020.2970609.

[38] W. Zhao, Y. Rong, C. Li, Y. Wang, X. Cai, and X. Yu, “High Precision Hemispherical Resonator Gyroscopes with Oven Control Systems,” *IEEE Sens J*, vol. 21, no. 6, pp. 7388–7401, Mar. 2021, doi: 10.1109/JSEN.2021.3050206.

[39] W. Jia, W. Chen, Y. Xiao, Z. Wu, and G. Wu, “A Micro-Oven-Controlled Dual-Mode Piezoelectric MEMS Resonator with ±400 PPB Stability over -40 to 80 °c Temperature Range,” *IEEE Trans Electron Devices*, vol. 69, no. 5, pp. 2597–2603, May 2022, doi: 10.1109/TED.2022.3159287.

[40] K. Ogata, *System Dynamics*, Fourth Edition. Pearson, 2004.

[41] T. L. Bergman, F. P. Incropera, D. P. Dewitt, and A. S. Lavine, “Fundamentals of heat and mass transfer,” *John Wiley & Sons.*, 2011.

[42] T. Köse, “DEVELOPMENT OF AN INTEGRATED RESONANT MEMS TEMPERATURE SENSOR A THESIS SUBMITTED TO THE GRADUATE SCHOOL OF NATURAL AND APPLIED SCIENCES OF MIDDLE EAST TECHNICAL UNIVERSITY,” 2016.

[43] J. W. Hutchinson, “STRESSES AND FAILURE MODES IN THIN FILMS AND MULTILAYERS,” 1996.

[44] J. D. Lim, "Improving adhesion of copper thin films of alumina substrate through interface engineering," Nanyang Technological University, 2011. doi: 10.32657/10356/65944.

[45] E. Şimşek, "MEMS RESONANT TEMPERATURE SENSING WITH VARIABLE COUPLING STIFFNESS AND IMPROVED SENSITIVITY A THESIS SUBMITTED TO THE GRADUATE SCHOOL OF NATURAL AND APPLIED SCIENCES OF MIDDLE EAST TECHNICAL UNIVERSITY," 2020.

[46] Katsuhiko. Ogata, *Modern control engineering*. Prentice-Hall, 2010.

APPENDICES

A. Temperature Control Code

```
clear
clc
close all;

%% CONNECT POWER SUPPLIES
g = gpib('ni',0,1);
g_2 = gpib('ni',0,5);
fopen(g);
fopen(g_2);

g.EOSMode = 'read&write';
g.EOSCharCode = 'LF';
g_2.EOSMode = 'read&write';
g_2.EOSCharCode = 'LF';
%% PARAMETERS
V_thermistor = 2; %Volts
R = 100000; %resistance
RT = 100000;    %resistance of thermistor at room temp
B = 4250;
T0 = 273.15+25; %initial temp

R_h = 87;     %R_h
R_h_1 = 90.28;
R_h_2 = 87.1;
R_h_3 = 90 + 1;
%% PLANT KP,KI,KD
temp_set1 = 30; % degree C

kp_1 = 0.1177;
ki_1 = 0.0058;

kp_2 = 0.1567;
% kp_2 = 0.005;
ki_2 = 0.0075;

kp_3 = 0.1481;
ki_3 = 0.0079;

kp_4 = 0.1536;
```

```
ki_4 = 0.0070;

%% TEMPERATURE READING

s = daq.createSession('ni');
addAnalogInputChannel(s,'Dev1', 0, 'Voltage');
addAnalogInputChannel(s,'Dev1', 1, 'Voltage');
addAnalogInputChannel(s,'Dev1', 2, 'Voltage');
addAnalogInputChannel(s,'Dev1', 3, 'Voltage');
addAnalogInputChannel(s,'Dev1', 4, 'Voltage');
addAnalogInputChannel(s,'Dev1', 5, 'Voltage');
addAnalogInputChannel(s,'Dev1', 6, 'Voltage');
addAnalogInputChannel(s,'Dev1', 7, 'Voltage');

rate = 1000;
s.Rate = rate;
s.DurationInSeconds = 0.1;
dataIn = s.startForeground;

ai0 = (dataIn(:,1))';
ai1 = (dataIn(:,2))';
ai2 = (dataIn(:,3))';
ai3 = (dataIn(:,4))';
ai4 = (dataIn(:,5))';
ai5 = (dataIn(:,6))';
ai6 = (dataIn(:,7))';
ai7 = (dataIn(:,8))';

volt_ai0 = mean(ai0);   %voltage of t1
volt_ai1 = mean(ai1);   %voltage of t2
volt_ai2 = mean(ai2);   %voltage of t3
volt_ai3 = mean(ai3);   %voltage of t4
volt_ai4 = mean(ai4);   %voltage of  g1
volt_ai5 = mean(ai5);   %voltage of g2
volt_ai6 = mean(ai6);   %voltage of g3
volt_ai7 = mean(ai7);   %voltage of g4

VR_0 = V_thermistor-volt_ai0;
RT0 = ((((V_thermistor*(87/3+1)-0)/((2-volt_ai0)/RT))-87)/(87/3+1))- RT;
ln_0 = log(RT0/RT);
TX_0 = (1/((ln_0/B)+(1/T0)));
TX_0 = TX_0-273.15;
temp_act0 = TX_0;

T_amb = temp_act0;
```

```
VR_1 = V_thermistor-volt_ai1;
% RT1 = volt_ai1/(VR_1/R);
RT1 = ((((V_thermistor*(R_h_1/3+1)-0)/((2-volt_ai1)/RT))-R_h_1)/(R_h_1/3+1))-
RT;
ln_1 = log(RT1/RT);
TX_1 = (1/((ln_1/B)+(1/T0)));
TX_1 = TX_1-273.15;
temp_act1 = TX_1;

VR_2 = V_thermistor-volt_ai2;
% RT2 = volt_ai2/(VR_2/R);
RT2 = ((((V_thermistor*(R_h_2/3+1)-0)/((2-volt_ai2)/RT))-R_h_2)/(R_h_2/3+1))-
RT;
ln_2 = log(RT2/RT);
TX_2 = (1/((ln_2/B)+(1/T0)));
TX_2 = TX_2-273.15;
temp_act2 = TX_2;

VR_3 = V_thermistor-volt_ai3;
% RT3 = volt_ai3/(VR_3/R);
RT3 = ((((V_thermistor*(R_h_3/3+1)-0)/((2-volt_ai3)/RT))-R_h_3)/(R_h_3/3+1))-
RT;
ln_3 = log(RT3/RT);
TX_3 = (1/((ln_3/B)+(1/T0)));
TX_3 = TX_3-273.15;
temp_act3 = TX_3;

T3_ilk = temp_act3;
%%

temp0(1)=temp_act0;
temp1(1)=temp_act1;
temp2(1)=temp_act2;
temp3(1)=temp_act3;


V_ai0(1) = volt_ai0;
V_ai1(1) = volt_ai1;
V_ai2(1) = volt_ai2;
V_ai3(1) = volt_ai3;
V_ai4(1) = volt_ai4;
V_ai5(1) = volt_ai5;
V_ai6(1) = volt_ai6;
V_ai7(1) = volt_ai7;
```

```
time(1) = 0;

pow_0 = zeros();
RT0_d = zeros();

i=1;
DT=0;
DT2=0;

Error_P_1 = temp_set1-temp_act0;
Error_I_1 = temp_set1-temp_act0;

Error_P_2 = temp_set1-temp_act1;
Error_I_2 = temp_set1-temp_act1;

Error_P_3 = temp_set1-temp_act2;
Error_I_3 = temp_set1-temp_act2;

Error_P_4 = temp_set1-temp_act3;
Error_I_4 = temp_set1-temp_act3;

App_volt_0 = zeros();
App_volt_1 = zeros();
App_volt_2 = zeros();
App_volt_3 = zeros();

while i<160000
    i;
    tic

    %% ERROR CALCULATION

    Error_P_1=temp_set1-temp_act0;
    Error_I_1=Error_I_1+(temp_set1-temp_act0)*DT;

    Error_P_2=temp_set1-temp_act1;
    Error_I_2=Error_I_2+(temp_set1-temp_act1)*DT;

    Error_P_3=temp_set1-temp_act2;
    Error_I_3=Error_I_3+(temp_set1-temp_act2)*DT;

    Error_P_4=temp_set1-temp_act3;
    Error_I_4=Error_I_4+(temp_set1-temp_act3)*DT;
```

```
pow_0 = (kp_1*Error_P_1)+(ki_1*Error_I_1);
volt_0 = sqrt(pow_0*86.8);

pow_1 = (kp_2*Error_P_2)+(ki_2*Error_I_2);
volt_1 = sqrt(pow_1*R_h_1);

pow_2 = (kp_3*Error_P_3)+(ki_3*Error_I_3);
volt_2 = sqrt(pow_2*R_h_2);

pow_3 = (kp_4*Error_P_4)+(ki_4*Error_I_4);
volt_3 = sqrt(pow_3*R_h_3);

if volt_0 > 20
   volt_0 = 20;
elseif  volt_0 < 0
   volt_0 = 0.001;
end

if volt_1 > 20
   volt_1 = 20;
elseif  volt_1 < 0
   volt_1 = 0.001;
end

if volt_2 > 20
   volt_2 = 20;
elseif  volt_2 < 0
   volt_2 = 0.001;
end

if volt_3 > 20
   volt_3 = 15;
elseif  volt_3 < 0
   volt_3 = 0.001;
end

volt_1 = -1*volt_1;
volt_3 = -1*volt_3;

App_volt_0(i) = volt_0;
App_volt_1(i) = volt_1;
App_volt_2(i) = volt_2;
App_volt_3(i) = volt_3;

volt_0 = sprintf('%.3f',volt_0);
```

```
volt_1 = sprintf('%.3f',volt_1);
volt_2 = sprintf('%.3f',volt_2);
volt_3 = sprintf('%.3f',volt_3);

to_pow_sup_g_0 = ['APPL P25V,',  volt_0];
to_pow_sup_g_1 = ['APPL N25V,',  volt_1];
to_pow_sup_g_2 = ['APPL P25V,',  volt_2];
to_pow_sup_g_3 = ['APPL N25V,',  volt_3];

fprintf(g,to_pow_sup_g_0);
fprintf(g,to_pow_sup_g_1);
fprintf(g_2,to_pow_sup_g_2);
fprintf(g_2,to_pow_sup_g_3);
fprintf(g,'OUTP ON');
fprintf(g_2,'OUTP ON');

%%  READ

pause(0.05);

dataIn=s.startForeground;
ai0=(dataIn(:,1))';
ai1=(dataIn(:,2))';
ai2=(dataIn(:,3))';
ai3=(dataIn(:,4))';

ai4=(dataIn(:,5))';
ai5=(dataIn(:,6))';
ai6=(dataIn(:,7))';
ai7=(dataIn(:,8))';

volt_ai0 = mean(ai0);
volt_ai1 = mean(ai1);
volt_ai2 = mean(ai2);
volt_ai3 = mean(ai3);

volt_ai4 = mean(ai4);
volt_ai5 = mean(ai5);
volt_ai6 = mean(ai6);
volt_ai7 = mean(ai7);


DT=toc+DT2;
%% CALCULATE NEW RESISTANCES
```

```
    V_ai0(i+1) = volt_ai0;
    V_ai1(i+1) = volt_ai1;
    V_ai2(i+1) = volt_ai2;
    V_ai3(i+1) = volt_ai3;

    V_ai4(i+1) = volt_ai4;
    V_ai5(i+1) = volt_ai5;
    V_ai6(i+1) = volt_ai6;
    V_ai7(i+1) = volt_ai7;

    A = 1/3;    %1/R_cg

    volt_0_app = str2double(volt_0);
    volt_1_app = str2double(volt_1);
    volt_2_app = str2double(volt_2);
    volt_3_app = str2double(volt_3);

    volt_1_app = 0;
    volt_3_app = 0;
%
    RT0_d = ((((V_thermistor*(R_h/3+1)-volt_0_app)/((2-volt_ai0)/RT))-
R_h)/(R_h/3+1))- RT;
    ln_0 = log(RT0_d/RT);
    TX_0 = (1/((ln_0/B)+(1/T0)));
    TX_0 = TX_0-273.15;
    temp_act0 = TX_0;

    RT1_d = ((((V_thermistor*(R_h_1/3+1)-volt_1_app)/((2-volt_ai1)/RT))-
R_h_1)/(R_h_1/3+1))- RT;
    ln_1 = log(RT1_d/RT);
    TX_1 = (1/((ln_1/B)+(1/T0)));
    TX_1 = TX_1-273.15;
    temp_act1 = TX_1;
    temp_act1 = temp_act1 -0.6*volt_1_app + 0.95*volt_3_app;


    RT2_d = ((((V_thermistor*(R_h_2/3+1)-volt_2_app)/((2-volt_ai2)/RT))-
R_h_2)/(R_h_2/3+1))- RT;
    ln_2 = log(RT2_d/RT);
    TX_2 = (1/((ln_2/B)+(1/T0)));
    TX_2 = TX_2-273.15;
    temp_act2 = TX_2;

    RT3_d = ((((V_thermistor*(R_h_3/3+1)-volt_3_app)/((2-volt_ai3)/RT))-
R_h_3)/(R_h_3/3+1))- RT;
```

```
    ln_3 = log(RT3_d/RT);
    TX_3 = (1/((ln_3/B)+(1/T0)));
    TX_3 = TX_3-273.15;
    temp_act3 = TX_3;

    temp_act3 = temp_act3 +  1*volt_3_app;


    temp0(i+1)=temp_act0;
    temp1(i+1)=temp_act1;
    temp2(i+1)=temp_act2;
    temp3(i+1)=temp_act3;


    time(i+1)=DT+time(i);


    %% PLOT DATA

    plot(time,temp0,time,temp1,time,temp2,time,temp3);
    legend('Thermistor_1','Thermistor_2','Thermistor_3','Thermistor_4');
    ylabel('Temperature(\circC)')
    xlabel('Time(sec)')
    tic


    plot(time,V_ai0,time,V_ai1,time,V_ai2,time,V_ai3);
    legend('Thermistor_1','Thermistor_2','Thermistor_3','Thermistor_4');
    ylabel('Voltage(V)')
    xlabel('Time(sec)')

    plot(time,App_volt_0,time,App_volt_1,time,App_volt_2,time,App_volt_3);
    legend('Thermistor_1','Thermistor_2','Thermistor_3','Thermistor_4');
    ylabel('Voltage(V)')
    xlabel('Time(sec)')

    i=i+1;
    DT2=toc;
end

%% RESETTING
fprintf(g,'OUTP OFF');
fclose(g)
delete(g)
clear g
```

```
fprintf(g_2,'OUTP OFF');
fclose(g_2)
delete(g_2)
clear g_2
```